Bending Stresses in Stay-Cables During Large-Amplitude Vibrations - A Fred Hartman Bridge Case Study

by

Aaron James Pebley, B.S.

Thesis

Presented to the Faculty of the Graduate School of

The University of Texas at Austin

in Partial Fulfillment

of the Requirements

for the Degree of

Master of Science in Engineering

The University of Texas at Austin

August 2005

Bending Stresses in Stay-Cables during Large-Amplitude Vibrations - A Fred Hartman Bridge Case Study

APPROVED BY
SUPERVISING COMMITTEE:

Loukas F. Kallivokas

Sharon L. Wood

Dedication

To my family and friends.

Acknowledgements

I would first like to thank the Texas Department of Transportation for funding this worthwhile investigation.

My sincere appreciation goes to the guidance provided by my graduate advisor Dr. Loukas Kallivokas. In addition to his help I would not have been able to complete this endeavor without the assistance of Dr. Sharon Wood and Dr. Karl Frank. To all three of these professors I am greatly indebted for the wisdom and patience you have shown to me.

Personally, without the loving support and endless encouragement of my family I would never have become the man I am today, let alone obtain a master's degree in engineering. I am forever thankful to have been blessed with the great fortune of having such wonderful people as family members.

I would also like to acknowledge the amazing friendships I have made during my two years here at Austin. The memories that I have created with these people of such high character and good humor will always be looked upon as some of the best in my life.

Lastly, I would like to thank God. Thanks for keeping things interesting.

August, 2005

Abstract

Bending Stresses in Stay-Cables During Large-Amplitude Vibrations - A Fred Hartman Bridge Case Study

Aaron James Pebley, M.S.E.

The University of Texas at Austin, 2005

SUPERVISOR: Loukas Kallivokas

After the 1996 completion of the Fred Hartman Bridge in Houston, Texas, there were several occasions when large-amplitude lateral vibrations of its stay-cables were observed. Whereas the exact cause of these vibrations has yet to be determined, the installation of Freyssinet dampers, the stiffening of the anchorage guide pipes, and the reinstallation of cable restrainers have since prevented reoccurrence of the vibrations. Despite the successful mitigation, there still remains a question about the effects these vibrations may have had on the stay-cables and their service/fatigue life. To address it, this work aims primarily at the determination of the bending stresses that arose in the cables during the observed

large-amplitude vibrations, as a precursor to quantifying the cables' fatigue life. In this context, this work draws from the field observations and laboratory experiments conducted under the auspices of a multi-year comprehensive investigative program funded by the Texas Department of Transportation, to arrive at a synthesis of observations, experiments, and computational models that may explain the observed stay-cable behavior. To this end, and with the primary goal of bending stress quantification in mind, a number of necessary secondary issues were also addressed; these include:

a. a plausible scenario for the observed large-amplitude vibrations;
b. computational models consistent with the field observations;
c. computational models for a series of cable fatigue-related experiments conducted at the Ferguson Structural Engineering Laboratory at the University of Texas at Austin over the course of the last two or three years;
d. correlation of the field with the laboratory observations; and
e. development of testing guidelines for a new series of bending fatigue tests based on the findings of this work.

Table of Contents

TABLE OF CONTENTS ..... **VIII**

LIST OF TABLES ..... **XI**

LIST OF FIGURES ..... **XII**

LIST OF FIGURES ..... **XII**

CHAPTER 1 INTRODUCTION **1**

1.1 MOTIVATION 1
1.2 ON CABLE-STAYED BRIDGES 2
1.2.1 Background 2
1.2.2 Contemporary concerns 5
1.3 RESEARCH OBJECTIVES 6
1.4 THESIS OUTLINE 8

CHAPTER 2 STAY-CABLE LARGE-AMPLITUDE VIBRATIONS **9**

2.1 CANDIDATE MECHANISMS 10
2.1.1 Vortex shedding 10
2.1.2 Turbulent buffeting 11
2.1.3 Galloping 11
2.1.4 Flutter 12
2.1.5 Deck or tower vibration (parametric excitation) 12
2.1.6 Wind and rain induced 14
2.2 FATIGUE EFFECTS OF LARGE-AMPLITUDE STAY-CABLE VIBRATIONS 16

CHAPTER 3 THE FRED HARTMAN BRIDGE CASE – COMPUTATIONAL MODELS OF FIELD OBSERVATIONS **17**

3.1 THE FRED HARTMAN BRIDGE - BACKGROUND 17
3.2 FIELD OBSERVATIONS 18

3.2.1 Major vibration incidents at the Fred Hartman Bridge 18
3.2.2 Damage to the stay cables 21
3.3 COMPUTATIONAL MODELING 22
3.3.1 Cable #24 characteristics – dynamic behavior 23
3.3.2 Parametric excitation preliminaries 29
3.3.3 Cable # 24 computational model and bending stress profile 34
3.3.3.1 Qualitative discussion of prior work 34
3.3.3.2 Quantitative analysis of bending stresses in cable #24 36
3.3.3.3 Cable #24 finite element modeling 37
3.3.3.4 Cable #24 static/modal response 40
3.3.3.5 Cable #24 transient analysis 41
3.3.3.6 Cable #24 bending moments and stresses 50

CHAPTER 4 COMPUTATIONAL MODELING OF LABORATORY EXPERIMENTS 54

4.1 LABORATORY EXPERIMENTS 54
4.1.1 Preliminaries 54
4.1.2 Experiment overview 54
4.1.2.1 Material properties - steel strands 56
4.1.2.2 Material properties - cement grout 57
4.1.2.3 Laboratory setup 57
4.1.2.4 Overview of fatigue test results 60
4.2 COMPUTATIONAL MODELING OF LABORATORY EXPERIMENTS 61
4.2.1 Modeling of grouted specimens 62
4.2.2 Discussion of grouted specimens results 64
4.2.2.1 Bending stresses in grouted specimens 73
4.2.2.2 Comparison of field and laboratory bending stresses 77
4.2.3 Modeling of ungrouted specimens 79
4.2.3.1 Finite element analysis of ungrouted specimens 80

CHAPTER 5 NEW TESTING GUIDELINES 88

5.1 OBJECTIVE 88
5.2 BEAM-CABLE: CHARACTERISTIC BEHAVIOR 88
5.2.1 The importance of the γ -parameter 89

5.2.2 Effects of γ on stress distribution 92
5.3 NEW EXPERIMENTAL SETUP 95
5.3.1 Two-strand specimen – physical characteristics 95
5.3.2 Two-strand specimen – computational model 96
5.3.2.1 Model geometry 97
5.3.2.2 Material properties and element types 98
5.3.2.3 Meshing 99
5.3.2.4 Loading and boundary/initial conditions 102
5.3.2.5 Solution approach 106
5.3.2.6 Results and comparison 106
5.3.2.7 Loading clamp expected stresses 111

CHAPTER 6 OBSERVATIONS AND CONCLUSIONS 119

6.1 SUMMARY 119
6.2 OBSERVATIONS 120
6.3 AXIAL FATIGUE LIFE ESTIMATES 123
6.4 CONCLUSIONS 125
6.4.1 On the modeling of stay-cables 125
6.4.2 On fatigue issues of stay-cables 125

APPENDIX A SMEARED PROPERTIES 127

A.1 BEAM MODELING 127
A.1.1 Fred Hartman Bridge Cable #24 127
A.1.2 Tested Laboratory Specimens 131

APPENDIX B CLOSED-FORM SOLUTIONS 141

B.1 STATIC CASE 141
B.1.1 Euler-Bernoulli Beam Equation 141
B.1.2 Cable modeling for un-grouted specimens 145

BIBLIOGRAPHY 149

VITA 154

List of Tables

Table 3.1 Free-length transformed properties of cables #22, 23, 24 23
Table 3.2 First 6 natural frequencies for Cable #24 (assumed flat) 28
Table 3.3 First 6 natural frequencies for Cable #24 29
Table 3.4 First 6 natural frequencies for Cable #24 using design tension 29
Table 3.5 Dynamic properties of cables #22 & #23 42
Table 3.6 Bending moment range for deck and tower anchorages 52
Table 4.1 Material properties of steel strands (units are English unless bracketed) 57
Table 4.2 Load at maximum applied displacement 60
Table 4.3 Wire fracture of fatigue specimens 61
Table 4.4 Specimen γ values 62
Table 4.5 Static test parameters for grouted specimens 63
Table 4.6 Comparison of static midspan deflections for grouted specimens 64
Table 4.7 Closed-form bending stresses at the terminations 76
Table 4.8 Closed-form bending stresses at mid-span 77
Table 4.9 Comparison of bending stress ranges at the terminations 78
Table 4.10 Comparison of static midspan deflections for ungrouted specimens 80
Table 4.11 ANSYS cable-model results 87
Table 5.1 Comparison of bending stress for ANSYS and closed-form models 108
Table 5.2 Results for matched bending stresses 113

List of Figures

Figure 1.1 The Fred Hartman Bridge, Houston, Texas, USA 1
Figure 1.2 Stay ropes on Egyptian sailing vessels circa 2000-1500 BC (reproduced from Ito 1991) 3
Figure 1.3 The Brooklyn Bridge, New York, New York, USA 4
Figure 1.4 The Strömsund Bridge, Sweden 4
Figure 1.5 The Sunshine Skyway Bridge, Tampa, Florida, USA 5
Figure 2.1 Standing wave generation mechanism 13
Figure 2.2 Helical filets on cable duct to prevent wind-rain induced vibrations .. 14
Figure 2.3 Yellow Tedlar tape wrapped around cables 15
Figure 2.4 Possible stress distribution for a grouted cable cross-section 16
Figure 3.1 Fan-shaped arrangement of Fred Hartman cables 17
Figure 3.2 Video of large-amplitude stay-Cable#24 vibrations (upward view) ... 19
Figure 3.3 Still frames of Cable #24 motion; the frames depict cable motion with an almost π phase difference; notice that a node seems to exist near the second restrainer ring (counting rings from the top of the tower) 20
Figure 3.4 Broken guide pipe to anchorage box connections 21
Figure 3.5 Cable oscillations for $\Omega = 1$ rad/sec 31
Figure 3.6 Cable oscillations for $\Omega = 2\pi$ 32
Figure 3.7 Symmetric oscillations assumed to have been induced by wind-rain (per Willox 1998) 35
Figure 3.8 Present working hypothesis – Deck movement 35
Figure 3.9 Relative peak-to-peak displacement 37
Figure 3.10 FEA approximation of moments of inertia in the deck anchorage 39
Figure 3.11 Termination at tower 39
Figure 3.12 Cable boundary conditions 40
Figure 3.13 Function generator input 43

Figure 3.14 Total displacement time-history for “restrainer-clip” node #928 44
Figure 3.15 Steady-state displacement of “restrainer-clip” node928 45
Figure 3.16 Frame-to-frame comparison of video and animation 46
Figure 3.17 Frames of cable #24 response animation 47
Figure 3.18 ANSYS animation looking up from deck towards tower 48
Figure 3.19 Video taken from other side of the deck 49
Figure 3.20 ANSYS animation from camera position across deck 49
Figure 3.21 Bending moment at the deck anchorage vs. time 50
Figure 3.22 Bending moment at the tower face vs. time 51
Figure 3.23 Bending moment at deck anchorage vs time (35-45 sec) 51
Figure 3.24 Bending moment at tower anchorage vs. time (35-45sec) 52
Figure 4.1 Strand arrangement – specimen #1 55
Figure 4.2 Strand arrangement – specimen #2-5, 7-12 55
Figure 4.3 Strand arrangement – specimen #6 56
Figure 4.4 Full-scale bending fatigue test setup (Ridd, 2004) 58
Figure 4.5 Clamp used for loading at mid-span (Ridd, 2004) 58
Figure 4.6 Geometry of grouted specimens (Ridd, 2004) 59
Figure 4.7 Geometry of un-grouted specimens (Ridd, 2004) 59
Figure 4.8 Cross-section at the anchor head 74
Figure 4.9 Cross-section along the free-length 75
Figure 4.10 Transition region of strand arrangement 81
Figure 4.11 Real constants for Link 8 elements 82
Figure 4.12 Boundary conditions at anchor head 82
Figure 4.13 Tension ring constraints 83
Figure 4.14 Mid-span loading and constraints 84
Figure 4.15 Entire specimen with boundary conditions and loads 85
Figure 4.16 Displaced shape of cable: full isometric view 86

Figure 4.17 Displaced shape of cable: oblique anchorage close-up..... 86
Figure 5.1 Mid-span moment versus γ 91
Figure 5.2 Effects of γ on moment distribution 93
Figure 5.3 Effect of γ on moment gradient for members with equivalent peak bending moments 94
Figure 5.4 Cross-section of ANSYS model 97
Figure 5.5 2-D mesh of cross-section..... 100
Figure 5.6 3-D extruded mesh..... 101
Figure 5.7 Fixed-end boundary conditions 103
Figure 5.8 Mid-span symmetric boundary conditions..... 104
Figure 5.9 Point-load application in ANSYS verification model 105
Figure 5.10 Scaled displaced shape under a point load..... 107
Figure 5.11 Oblique view of bending stresses at the anchorage (units in lbs/in^2) 109
Figure 5.12 Isometric view of bending stresses at mid-span (units in lbs/in^2).... 109
Figure 5.13 Longitudinal grout stresses at the anchorage face (units in lbs/in^2) 110
Figure 5.14 Loading clamp application..... 112
Figure 5.15 Longitudinal steel stress at anchorage (units in lbs/in^2)..... 113
Figure 5.16 Longitudinal steel stress at mid-span (units in lbs/in^2) 114
Figure 5.17 Longitudinal stress in the grout at the fixed-end (units in lbs/in^2)... 115
Figure 5.18 Longitudinal stress in the grout at the mid-span (units in lbs/in^2) ... 115
Figure 5.19 Overall rate of change of extreme fiber tension stress..... 116
Figure 5.20 Close-up of stress gradient for peak tensile steel strand 117
Figure 6.6.1 Effect of γ on moment gradient for members with equivalent peak bending moments (Fig. 5-3 repeated) 122
Figure 6.6.2 Close-up of stress gradient for peak tensile steel strand 124
Figure A.1 Cross-Section of Cable #24 128

Figure B.1 Schematic of un-grouted test specimens 145

CHAPTER 1
Introduction

1.1 MOTIVATION

Between 1996 and 1997, several of the longer cables of the Fred Hartman Bridge (Figure 1.1), a cable-stayed bridge spanning the Houston shipping channel, experienced large-amplitude vibrations. Though the exact cause and generative mechanisms of the observed vibrations continue to be the subject of technical investigations, it seems that invariably the large-amplitude vibrations appeared during favorable wind and/or wind and rain conditions. Since the time of the observed incidents, the redesign of the broken anchorage guide pipes, the strengthening and reinstallation of previously broken cable restrainers, and the installation of two types of visco-elastic dampers, have successfully prevented the reoccurrence of the undesirable cable vibrations.

Figure 1.1 The Fred Hartman Bridge, Houston, Texas, USA

However, beyond what could have been assessed by visually inspecting the cables and their anchorage points, it remains unclear whether the cables' steel strands were damaged during the cyclic loading induced by the dynamic large-amplitude cable motion. The work presented in this thesis is motivated by the need to understand what may have caused the large-amplitude motion, to postulate the source mechanism, to estimate the impact the motion may have had on the stresses in the cables, and, as a consequence, to provide a rational basis for assessing the impact the motion may have on the fatigue life of the stay-cables.

1.2 ON CABLE-STAYED BRIDGES

1.2.1 Background

Though, the underlying principles of cable-stayed bridge design have been in use for thousands of years, it is only in the last fifty years that cost and constructability issues have been overcome sufficiently to allow for the construction of, by now, more than three hundred cable-stayed bridges worldwide. Their history is instructively rich: ancient Egyptians used rope-stayed principles in their sailing ships (Figure 1.2), with a main mast supporting the weight of beams through a system of inclined ropes connected directly to the mast (Ito 1991). However, since the essential elements needed for cable-stayed bridges (the cables) are absent through much of the recorded history, it is only in the 1600s that a Venetian carpenter, Verantius, builds, for the first time, a timber bridge using chain stays (in place of the (ancient) ropes or the (modern) cables). Later, in 1784, Löscher, a Swiss carpenter also constructed a short-span (32m) timber bridge made entirely of wood (including the stays).

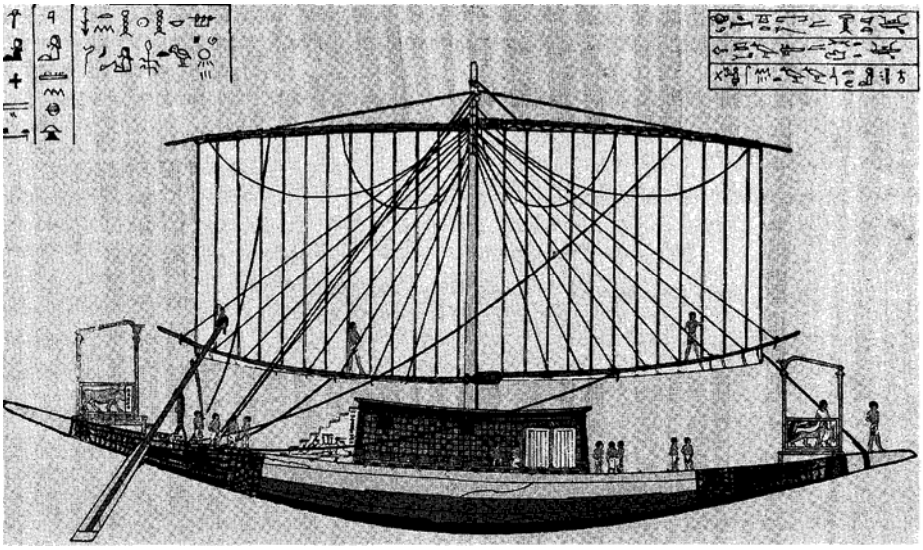

Figure 1.2 Stay ropes on Egyptian sailing vessels circa 2000-1500 BC (reproduced from Ito 1991)

The incorporation of cables in bridge design has allowed for significant increases in span length and total load capacity. In the early stages of large-scale bridge construction, beginning in the early-to-mid 19th century, a lack of advanced structural analysis methods and of sufficiently stiff steel-wires prevented any bridge from being designed solely with stay-cables; instead, the suspension bridge was gaining popularity among the premier bridge designers of the time. Perhaps the most famous of this group, John A. Roebling, designed, what proved to be, the archetypical suspension bridge, Brooklyn Bridge (Figure 1.3) (opened in 1883). Following the improved strength and constructability of steel cables proven in the design and construction of suspension bridges, time came for cable-stayed bridge designs to materialize. In 1955 German engineer Dischinger designed and built the first modern cable-stayed bridge, the Strömsund Bridge in Sweden (Figure 1.4), which opened to traffic in 1956. The Strömsund Bridge proved to be the first

of a growing number of cable-stayed bridges built throughout Scandinavia and Europe between the mid-to-late 20th century.

Figure 1.3 The Brooklyn Bridge, New York, New York, USA

Figure 1.4 The Strömsund Bridge, Sweden

By contrast, the development of cable-stayed bridges in the United States took somewhat longer. The Sunshine Skyway Bridge (Figure 1.5), constructed in Tampa, Florida in 1988 is regarded today as an important cable-stayed bridge in the US for having brought national attention to the efficient constructability and aesthetic appeal of cable-stayed bridges. To date there are over 25 cable-stayed bridges in the United States; the list includes the Fred Hartman Bridge (Fig. 1.1), whose dynamic behavior prompted this investigation.

Figure 1.5 The Sunshine Skyway Bridge, Tampa, Florida, USA

1.2.2 Contemporary concerns

Once, during modern times, the constructability difficulties were overcome, attention and emphasis shifted to cost considerations. Since in cable-supported bridges (whether of the cable-stayed or the suspension type) the steel cables are the main load-transferring elements (to the towers), the overall weight of the bridge can be significantly lowered. However, whereas the lighter structure may be economically and aesthetically more appealing than competitive designs, the bridge's slender profile and increased flexibility allow a cable-stayed bridge to be more susceptible to cyclic loads of various origins. Indeed, wind-or combined wind-and rain-induced vibrations seem to be plaguing a significant number of cable-stayed bridges worldwide. In fact, design

specifications for cable-stayed bridges in the United States are required to incorporate these issues in the overall design process (PTI 2000).

Without remedial intervention, the cyclic loading imparted on the cables (and the rest of the bridge's structural elements), will ultimately lead to a substantial decrease of the bridge's intended lifespan or premature failure (Leonhardt 1991). In particular, cable-steel-strand fatigue emerges as a key concern among those bridges that are susceptible to large-amplitude vibrations of their stay cables. Whereas considerable research has been devoted to the study of fatigue behavior/failure for steel strands under cyclic axial loading (Hobbs and Ghavami 1982; Papanikolas 1995), the study of fatigue failures due to bending stresses on steel strands has received less attention; the issue of fretting fatigue failures of grouted steel strands has received even less attention (but see Raoof, 1993). Given that the observed large-amplitude vibrations were typically accompanied by abrupt changes in local curvatures, the latter issue of fretting fatigue arises as a primary (candidate) failure modality.

1.3 RESEARCH OBJECTIVES

To be able to quantify potential fatigue failure, it is necessary to arrive at an estimate of the stresses developed during the dynamic response of the cables. In turn, this requires the ability to reproduce, either experimentally or computationally, the observed field behavior. The latter has, thus far, proved to be elusive, for the source of the vibrations is difficult to identify and quantify due to the lack of recorded data and the complexity of the observed phenomena. Potential sources include wind (and rain) loads on the deck, the towers, and the cables, as well as traffic loads which may or may not exacerbate the dynamic response of any or all of the above structural elements. Thus, in its truest form,

whether computationally or experimentally, the modeling ought to provide for the coupling of all of the above structural elements (in all of their respective complexity), while taking into account the fluid-structure interaction aspects (with the need to include turbulence effects as well), together with realistic loads ideally correlated with field measurements. Whereas such modeling is within present technological means, it is considerably complex, and thus escapes the scope of this work. Instead, attention here has been given to charting a reasonable investigative path, given the minimal field data that were available for the Fred Hartman Bridge under consideration. Thus, in summary, the research objectives are:

- **A plausible scenario for the observed large-amplitude vibrations**

  A first goal is to characterize the mechanism that caused the large-amplitude vibrations observed in the Fred Hartman Bridge and to quantify the source loads. It is important to note that the discussion and approaches followed in this work rely heavily on a single video showing large-amplitude vibrations of the stay cables in the Fred Hartman Bridge (recorded in April 1997). This essentially represents the only field-related data made available to this work. It should be noted that the mechanism causing the vibrations on the specific date of the recording need not be the same for any other day where similar or different cable motion was observed. Thus, it is possible that the conclusions may lack generality, but, nevertheless, given the uniqueness of the data, the presented analysis is based exclusively on this information.

- **Computational models consistent with the field observations**

  A subsequent goal consists of creating the computational models that would be able to reproduce the observed field behavior, and will thus allow for computational determination of the induced stresses.

- **Computational models consistent with laboratory experiments**

There have been twelve bending fatigue experiments conducted at the Ferguson Structural Engineering Laboratory at the University of Texas at Austin to investigate the impact the large-amplitude dynamic behavior may have had on the stay-cables in question. A goal of this work is to reproduce computationally the observed behavior of the laboratory specimens, again in an effort to characterize/predict the stress distribution in the cables.

- **Discussion and correlation of field and laboratory observations**

Since the possibility exists for a mismatch between the field and laboratory observations, the objective here is to correlate the computational and experimental outcomes between the two environments. Discrepancies have been identified and are noted here.

- **New testing guidelines**

Finally, based on the prior findings, recommendations are made for a future experimental setup that may allow for a tighter correlation of field and laboratory observations.

1.4 THESIS OUTLINE

This thesis is structured as follows: Chapter 2 reviews candidate mechanisms for large-amplitude cable vibrations. Chapter 3 focuses on the Fred Hartman Bridge case, discusses the field data, and associated computational models, in an effort to reproduce the field observations. Chapter 4 presents the computational models and associated discussion that reproduce the laboratory experiments. Chapter 5 provides new testing guidelines consistent with the findings of this work, and Chapter 6 presents a summary of the conclusions.

CHAPTER 2
Stay-Cable Large-Amplitude Vibrations

Large-amplitude vibrations of stay cables have been steadily reported since, at least, 1984 (Hikami 1986). The slender cylindrical geometry of the cables, the drive for ever longer spans[1] that, in turn, is responsible for longer cables, coupled with slender bridge deck designs, and the unavoidable exposure to the elements, make the cable the bridge's structural element best positioned for experiencing undesirable vibrations during a bridge's lifetime. Large-amplitude vibrations of stay-cables have been reported worldwide, including bridges in France (e.g. the Normandie and the Brotonne Bridges), in Belgium (e.g. the Ben-Ahin and Wandre Bridges), in Japan (e.g. the Meiko-Nishi Bridge), in Portugal (the Tagus River Bridge), in Thailand (the Rama IX Bridge), in the UK (the Dee River Crossing Bridge), in the USA (the Fred Hartman and Veterans Memorial Bridges), and elsewhere. Whereas the precise reasons for these worldwide reported incidents vary widely, it is generally accepted that wind or wind-rain conditions must be present for inducing large-amplitude cable motion. That this is indeed the case has been repeatedly demonstrated worldwide by both field, experimental, and analytical investigations (Ghaffer and Khalifa 1991; Lilien and Pinto Da Costa 1994).

It is noteworthy that, despite the common origin of the problem (e.g. wind), the root causes are often classified based on the manner by which a

[1] The current record holders are the Tatara Bridge in Japan (890m), and the Normandie Bridge in France (856m), but plans are underway for the Stonecutter Bridge in Hong Kong with a tower-to-tower span exceeding 1000m.

particular bridge element is excited, and/or the type of structural element first excited. For example, vortex induced vibrations (VIV) at certain wind speeds may produce deck oscillations and not cable oscillations (Verwiebe 1998), if the two systems were not connected. In such a case, the VIV of the deck is considered the root mechanism and any cable vibrations are secondary effects. Thus, given the complexity of interactions (cable-to-tower, tower-to-deck, cable-to-deck, wind-to-cable, wind-to-deck, etc), a more detailed classification of the root mechanisms is needed. These are reviewed below.

2.1 CANDIDATE MECHANISMS

All of the mechanisms reviewed below refer to aerodynamic instabilities that arise, under certain conditions, whenever a solid interrupts the flow of moving air (wind). Some are due to separated flow phenomena (e.g. vortex shedding, galloping), i.e. to phenomena that arise when the flow does not tightly follow the contour of the obstacle it meets in its path, whereas others do not necessarily involve flow separation (e.g. flutter). Specifically:

2.1.1 Vortex shedding

When wind blows around an object, at very low or low Reynolds numbers the flow essentially circumscribes the object. However, as the speed of the wind increases, or at higher Reynolds numbers, there is flow separation accompanied by the formation of vortices. To maintain the balance of the fluid momentum around the object, the vortices are shed. The shedding alternates between the upper and lower sides of the object's profile perpendicular to the wind direction, thereby creating alternating forces on the object. These alternating forces cause the object to vibrate. Vortex shedding in a cable-stayed bridge may affect both the deck and the cables, but the cables are more susceptible (Chang et al. 1997).

In fact, vortex shedding may affect either one or a group of cables depending on the cable arrangement (fan, radiating, etc), and local flow conditions. Typically, the frequency, N, of the alternating forces induced by vortex shedding is given by

$$N = \frac{U \cdot S}{H} \qquad 2.1$$

where U is the wind velocity, H is the depth of the cable's profile, and S is the Strouhal number for the particular profile (for a circular cylindrical body, such as a cable, and for a wide range of Reynolds numbers, the Strouhal number S value is close to 0.18). Though vortex shedding may induce cable vibrations, the motion amplitude is typically constrained (Simiu and Scanlan, 1986), thereby not causing overall large-amplitude vibrations.

2.1.2 Turbulent buffeting

Buffeting vibrations are due to turbulent flow conditions. Such conditions can occur both at the inflow (the wind blowing towards the structure) level, or at the wake of a neighboring object. For example, the vortex shedding described above may lead to turbulent conditions at the wake of an upstream body, which, in turn, affects the inflow conditions (turbulent) of a downstream object. This type of wake buffeting is uncommon in bridges, but the turbulent inflow buffeting may significantly affect bridges, especially the movement of the deck.

2.1.3 Galloping

Galloping is most commonly encountered in transmission lines. It is an aerodynamic instability associated with the presence of an object whose profile conforms to one of the geometric shapes that are unstable in an air-stream. The classical case arises in transmission lines when ice deposits render the otherwise circular cable cross-section into an elliptical one, with the major ellipse axis

perpendicular to the wind direction. But, in general, even in the presence of an, otherwise, stable cross-section, the forces exerted by a steady wind on the object are a function of the angle of attack (for oblique incidence). Thus, even a cable with a circular cross-section may experience the same kind of destabilizing force (the force is typically proportional to the velocity and has a "negative" damping effect, i.e., it adds energy to an already vibrating system), as the unstable cross-section at vertical angle of incidence case. In these cases, the amplitudes grow uncontrollably and galloping may lead to catastrophic failure. It should be noted that, even though galloping of stay-cables is theoretically possible, there has been no field evidence of galloping stay-cables (Jones, 2003).

2.1.4 Flutter

There are many types of aero-elastic vibrations that are often called flutter. Typically, flutter occurs when an object's deflections under wind load cause the load itself to get reduced (due to the changed shape), which, in turn, allows the object to return to its original shape, which, in turn, restores the original load, which, in turn causes the object to deflect, thereby changing its shape, and causing this oscillatory cycle to repeat itself. The failure of the Tacoma Narrows Bridge in 1940 has been attributed to flutter inducing second-mode torsional failure. A prerequisite for flutter is adequate structural flexibility (slenderness helps).

2.1.5 Deck or tower vibration (parametric excitation)

Another possible means for significant cable vibrations to occur is through standing waves caused by vibrations of the deck due to the bridge deck's own aerodynamic instability (similarly for the tower, albeit due to the typical pylon mass and stiffness, tower instabilities/vibrations are less likely). The conditions

under which a bridge's deck may be excited are the same as those described in the preceding paragraphs.

When the deck moves a wave is sent up to the tower through every cable anchored in the deck (whipping motion). Due to the fixity condition at the tower end, the wave reflects in the pattern depicted in Figure 2.1.

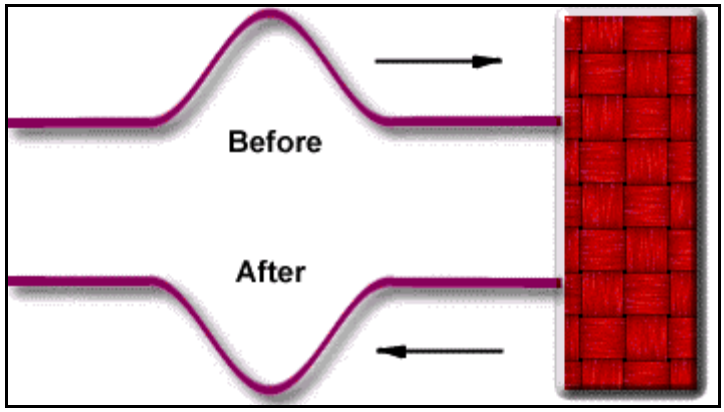

Figure 2.1 Standing wave generation mechanism

However, due to the continuing motion of the deck, a train of similar pulses has already left the deck traveling to the tower and interfering with the reflected waves from the tower's anchorage. The interference is both constructive and destructive causing the formation of, so-called, standing waves. When the motion of the deck is at a frequency that coincides (or is close) to a cable's natural frequency, then there results large-amplitude cable motion. It should be noted that the pattern of cable response may be quite complex as, axial (or, so-called, elastic), transverse, and out-of-plane modes may result from the parametric deck or tower excitation. Typically, due to the sagging cable's geometric nonlinearities, the amplitudes do not increase uncontrollably, as would have been the case for a taut flat cable. The presence of damping may also

alleviate the instability (however, the large-amplitude motion will be maintained), but its role is less important than the geometric nonlinearities.

2.1.6 Wind and rain induced

Another possible cause of vibrations in cables, similar to galloping, in that it depends on the profile of the cables in a steady wind flow, is the phenomenon of wind-and rain-induced vibrations. Accordingly (Matsumoto et al. 2003), under favorable conditions (e.g. wind at moderate speeds, wind direction at an angle with respect to the cable, the cable declined in the wind direction) water rivulets form in the upper and lower surfaces of the cable. The rivulets change the aerodynamic shape of an otherwise circular cable cross-section, thereby causing aerodynamic instability similar to the one caused in galloping. As the cable oscillates the rivulets change location, creating oscillatory aerodynamic forces acting on the cable that keep feeding energy to the oscillations ("negative" damping effect). Wind-tunnel testing has confirmed the presence of rivulets and the associated instability (Gu and Du 2005).

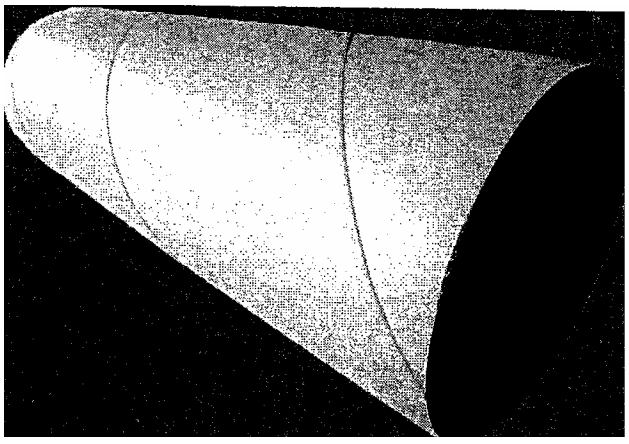

Figure 2.2 Helical filets on cable duct to prevent wind-rain induced vibrations

It has been argued (Hikami and Shiraishi 1988) that for the rivulets to form there is need for a smooth cable surface. One current remediation technique, used in Japan and France, is the installation of cable ducts that utilize helical filets in order to provide a groove to channel water down the length of the cable while minimizing the obstruction of airflow over the cable. Such a helical duct is shown in Figure 2.2 (Virlogeux 1998).

It is noteworthy that a similar helical pattern can be seen in the Fred Hartman Bridge cables due to the use of Tedlar tape (for purposes of ultraviolet protection) that is wrapped around the cables. This yellow tape can be seen on the cables in Figure 2.3.

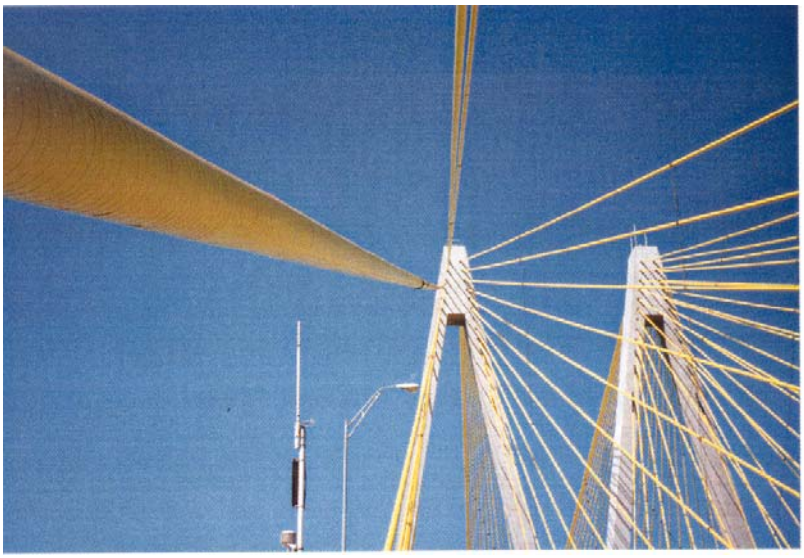

Figure 2.3 Yellow Tedlar tape wrapped around cables

Based on the available field data and among all described mechanisms the one that appears, as will be illustrated in the next chapter, as the likely candidate for having caused the Fred Hartman bridge large-amplitude cable vibrations is the deck parametric excitation.

2.2 FATIGUE EFFECTS OF LARGE-AMPLITUDE STAY-CABLE VIBRATIONS

Having described the various possible causes of dynamic excitation in stay-cables it is important to get a qualitative understanding of what effect these dynamic actions have on the internal forces in the cables (Wyatt 1960). Under large-amplitude vibrations it is readily apparent that significant bending moments may develop due to high local curvatures.

Similarly to the distribution of bending stresses in any reinforced concrete cross-section, the following figure provides a schematic of how stresses may be distributed across a typical cable cross-section assuming that the cement grout has cracked in tension and the "Whitney stress block" approximates the cement-grout's non-linear compressive behavior.

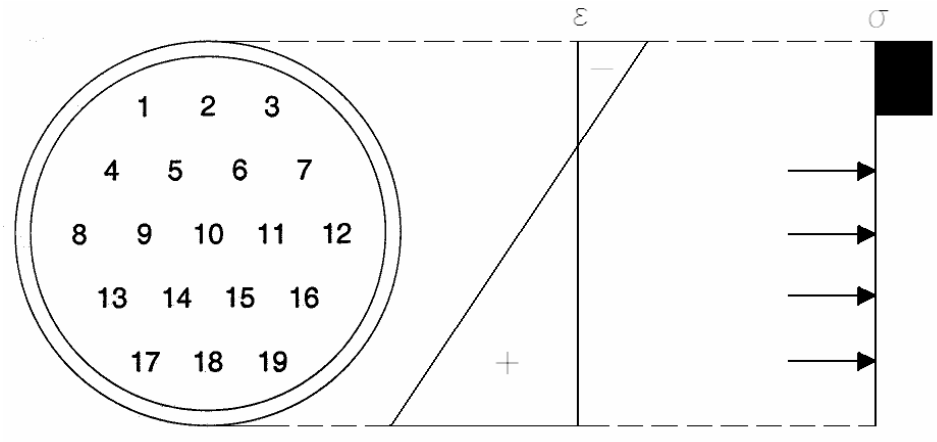

Figure 2.4 Possible stress distribution for a grouted cable cross-section

CHAPTER 3

The Fred Hartman Bridge Case – Computational Models of Field Observations

3.1 THE FRED HARTMAN BRIDGE - BACKGROUND

Completed in 1995 after nearly 10 years of construction, the Fred Hartman Bridge, like so many other cable-stayed bridges, has become a significant architectural landmark. The bridge has two independent steel-girder decks supported by four 436 ft A-shaped towers and 192 steel-stranded stay-cables. Some of the widest decks on any cable-stayed bridge in the world at 78 ft in width are supported by the bridge and see almost 200,000 vehicles cross them per day.

The cables, in a fan-type of arrangement (Figure 3.1), support a main-span bridge length of 1250 ft and a total span length of 2475 ft.

Figure 3.1 Fan-shaped arrangement of Fred Hartman cables

The cables themselves are composed of a varying number of 270K steel strands with the largest cable containing 61 strands. Cement grout surrounds the 7-wire strands used in each cable, which are in turn contained in a high-density polyethylene (PE) pipe. The grout and PE pipe protect the steel strands from potential corrosion due to the cable's exposure to the elements.

At 650 ft, Cable #24 is one of a group of eight cables that are the longest on the bridge. The cable is connected to the south west tower and runs east-west from its deck anchorage to its tower connection.

3.2 FIELD OBSERVATIONS

3.2.1 Major vibration incidents at the Fred Hartman Bridge

Between 1995 and 1997 the stay cables of the Fred Hartman Bridge experienced large-amplitude vibrations. The best available source (and sole source in this work) of information regarding the dynamic behavior of the cables in the field originates from two video recordings taken on April 4, 1997 at 6:41am and 6:55 am (see Figure 3.2 for an excerpt from the 6:55 am video). Standing near mid-span of the southern bridge deck, the cameraman shot this segment of the video facing the southwestern tower, looking, for the most part, up the length of Cable #24. The vibrations took place during a storm of moderate wind and rain; reportedly (Poston 1998), the maximum displacements observed on Cable #24 were ± 21 in above and below the center line of the cable. The frequency of vibration near the anchorage points has been previously estimated to be around 1.8 Hz (Poser 2001). These estimates are somewhat revised in this thesis (see section 3.3.3).

Figure 3.2 Video of large-amplitude stay-Cable#24 vibrations (upward view)

Figure 3.3 depicts two frames isolated from this video. Despite the perspective and the oblique angle of viewing, Figure 3.3 clearly shows cable motion of significant amplitude. In addition, the frames are chosen as to best demonstrate the maximum and minimum displaced positions of the upper-most restrainer clip.

Figure 3.3 Still frames of Cable #24 motion; the frames depict cable motion with an almost π phase difference; notice that a node seems to exist near the second restrainer ring (counting rings from the top of the tower)

3.2.2 Damage to the stay cables

The most apparent damage done by these large-amplitude vibrations was the breaking of nearly all of the bridge's 192 guide pipes, which are located at the cables' deck anchorage points (See Figure 3.4). The guide pipes were all subsequently repaired.

Figure 3.4 Broken guide pipe to anchorage box connections

In addition, the motion of the cables led to the fatigue failure of restrainer-links connecting individual cables to each other. Placed originally to help prevent large-amplitude vibrations from occurring, the restrainers are a series of steel wires connecting the cables together to increase overall stiffness (Figure 3.4).

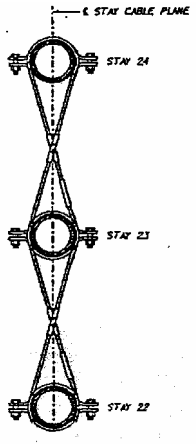

Figure 3.4 Schematic of original cable restrainer-links

As it can be easily seen in the 1997 video of the cable vibrations (Figure 3.2), the cable restrainers connecting the uppermost cable (Cable #24) to the surrounding cables were broken. The cable is clearly vibrating independently of the other cables. In fact, it may also be argued, based on the recording, that even the two cables below Cable #24, Cables #23 and #22, respectively, had all restrainers connected to them broken as well.

3.3 COMPUTATIONAL MODELING

In order to be able to quantify the stress distribution during the observed large-amplitude vibration, it is necessary to be able to computationally reproduce the observed motion. This requires reverse-engineering the source excitation that caused the cable's response: it is an exacting task, but not an impossible one. The steps that need to be taken include image analysis to digitize the observed motion by first filtering out the camera jitter, establishing the camera location and viewpoint vector through affine transformations and comparisons with known stationary points, identifying the skeleton of the object to be followed from frame-to-frame, and finally extracting the motion in a time history format (assuming that time estimates are possible). Once the time history is obtained, it is theoretically feasible to seek to establish the time-dependent excitation that has caused the extracted motion. The latter alludes to a time-dependent inverse problem where an appropriately chosen misfit functional between the measured motion and a computed one based on an estimate of the source excitation is minimized, subject to the governing partial-differential-equations of the cable's dynamics. The complexity and the nonlinearities of the (so-called) forward problem exacerbate the difficulties of this approach. Nevertheless, the primary difficulties in

following this approach emanate from the poor video source and the lack of appropriate resources for the image analysis task.

Thus, an alternate path to the motion reconstruction was followed: accordingly, the various mechanisms described in the previous chapter were reviewed together with the recorded motion, and preliminary calculations assisted in establishing a plausible scenario. Of all the possible mechanisms, it appears that the deck parametric excitation is the most likely cause. The discussion that follows is based on the above hypothesis and, as it will be shown, the computed motion that resulted from it closely matches the observed field behavior. We review next the details of the computational setup, starting with a discussion on the dynamic behavior of cables.

3.3.1 Cable #24 characteristics – dynamic behavior

Since Cable #24 is clearly disconnected from all other surrounding cables in the 6:41 am and 6:55 am videos (i.e. the interactions are simpler), and since it exhibits by far the most dramatic dynamic response, it is the primary focus of analysis in this thesis. Its properties are summarized in Table 3.1 below: amongst them are modulus and moment of inertia values whose calculation was based on smeared cross-sectional properties based, in turn, on the cable's free-length properties as those were obtained from the original bridge drawings. The calculation details can be found in Appendix A. It should be noted here that the tension force shown in the table is based on pluck tests performed (Poston, 1998) on Cable #24, and does not represent the design value (the tension force was found to be 9% lower than the design value).

Table 3.1 Free-length transformed properties of cables #22, 23, 24

Transformed Properties						
Cable #	Length (in)	Weight (kips)	Moment of Inertia (in^4)	Young's Modulus (ksi)	Area (in^2)	Tension (kips)
22	6630	27.2	18.72	27500	10.72	885
23	7207	32.4	23.93	27500	17.34	1000
24	7789	34.9	23.93	27500	17.34	925

In the analysis of both the static and dynamic behavior of stay-cables there are two critically important dimensionless parameters that encapsulate a cable's physical behavior (Irvine, 1981). These parameters are subsequently denoted by γ and λ^2. Specifically,

$$\gamma = \sqrt{\frac{T \cdot L^2}{E \cdot I}}, \tag{3.1}$$

and

$$\lambda^2 = \left(\frac{mgL}{T}\right)^2 \cdot \frac{E \cdot A \cdot L}{T \cdot L_e} \tag{3.2}$$

where T denotes tension force, L denotes the cable's overall length, E is Young's modulus, I is the second moment of inertia, A is the cross-sectional area, m is the mass per unit length, g is the gravity acceleration, and L_e is the cable's effective length that takes into account the sagging due to self-weight. L_e is typically slightly larger than the cable span L, and is defined as:

$$L_e = L\left(1 + 8 \cdot \left(\frac{d}{L}\right)^2\right), \tag{3.3}$$

where d is the midspan sag given by:

$$d = \frac{mgL^2}{8T}\left[1 - \frac{8}{\gamma^2}\left(1 - \operatorname{sech}\frac{\gamma}{2}\right)\right] \tag{3.4}$$

The parameter γ indicates the relative importance of cable and beam actions (Irvine, 1981): for large γ values (of the order of hundred or hundreds or larger) cable action dominates (in our calculations it appears that the cutoff value between beam and cable action is approximately at $\gamma = 48.99$ as shown in Chapter 5), otherwise the flexural rigidity cannot be ignored. Parameter λ^2 accounts for the relative importance between elastic and geometric effects (Irvine, 1981). Elastic effects typically imply axial deformations, whereas geometric effects typically allude to cable sagging. In other words, λ^2 is a measure of how taut (or how much extensible/inextensible) the cable is; as it can be seen from equation 3.2, its value largely depends on the ratio of the cable's weight to the tension force.

Based on the Cable #24 properties listed in Table 3.1 these two important parameters can be shown to be:

$$\gamma_{24} = 292$$

$$\lambda_{24}^2 = 0.72$$

The above value of γ_{24} clearly indicates dominant cable action, as one would expect from a stay-cable. The above value of λ_{24}^2 is clearly indicative of a relatively taut cable (notice also the weight to tension ratio $\frac{mgL}{T} = 0.038$, another characteristic of taut cable behavior). In the literature (e.g. Irvine, 1981), a measure of acceptance of taut-string theories for cables is based on whether the inequality $\frac{12}{\lambda^2} >> 0.5$ is satisfied. For Cable #24 the inequality reads:

$$\frac{12}{\lambda_{24}^2} = \frac{12}{0.72} = 16.67 >> 0.5$$

A more restrictive measure is to require that $\lambda^2 < 0.1$ (see, for example, Lilien and Pinto da Costa, 1994), which is clearly violated by Cable #24. Nevertheless, it is safe to use the dynamic theory applicable to taut inclined strings, by neglecting second- and higher-order terms (and associated nonlinearities), for deducing the dynamic characteristics and behavior of Cable #24. Accordingly, the fundamental behavior is briefly discussed below; details can be found in classic texts (e.g., Irvine 1981). The focus is first on flat cables; the effects of inclination will be discussed later in this section. We remark that the simplifications are made here for purposes of presentation; for the computational modeling the true nonlinear coupled behavior has been taken into account.

For a flat taut cable there arise three equations of motion, corresponding to two in-plane components and one out-of-plane component (uncoupled). The out-of-plane displacement describes swinging motion. The two in-plane components describe axial (or longitudinal) and vertical (or transverse) displacements. Of interest here is the transverse in-plane motion, for there is no evidence of out-of-plane motion in the observed field vibrations. Moreover, the axial displacement is generally small.

Let $w(x,t)$ denote the transverse in-plane displacement of the cable. Then, there are, in general, two forms of in-plane transverse modes that arise in cables: symmetric and anti-symmetric. As the cable vibrates the changes in shape may induce additional tension; let the additional tension be denoted with $h(t)$. Then, it can be shown (Irvine 1981) that:

$$h(t) = \frac{mg}{T}\frac{EA}{L_e}\int_0^L w(x,t)dx \tag{3.5}$$

If the modes are such that $\int_0^L w(x,t)dx = 0$ for all times t, then the additional dynamic tension $h(t)$ vanishes. The requirement however that $\int_0^L w(x,t)dx = 0$, clearly implies anti-symmetric modes (e.g. a full sine shape accommodated within the length of the cable). By contrast, symmetric modes (reflective symmetry about the perpendicular bisector of the cable) induce additional tension. It can then be easily shown that there are different natural frequencies associated with the two modalities of in-plane transverse motion. Specifically, for the anti-symmetric modes, the natural frequencies are:

$$\omega_{\text{anti-sym},n} = \frac{2n\pi}{L}\cdot\left(\frac{T}{m}\right)^{\frac{1}{2}} \qquad n = 1,2,3,... \tag{3.6}$$

Similarly, the natural frequencies corresponding to the symmetric mode shapes can be obtained using the following transcendental equation:

$$\tan\left(\frac{\hat{\omega}}{2}\right) = \frac{\hat{\omega}}{2} - \frac{4}{\lambda^2}\cdot\left(\frac{\hat{\omega}}{2}\right)^3 \tag{3.7}$$

where,

$$\omega_{\text{sym},n} = \frac{\hat{\omega}}{L}\sqrt{\frac{T}{m}} \tag{3.8}$$

and n here denotes order in the ordered root set of 3-7. Using the above equations the first three anti-symmetric and symmetric natural frequencies are calculated for Cable #24 are shown in Table 3.2.

Table 3.2 First 6 natural frequencies for Cable #24 (assumed flat)

Natural Frequencies (rad/sec)		
n	ω (sym)	ω(anti-sym)
1	3.62	7.23
2	10.85	14.45
3	18.08	21.69

It is noteworthy that the frequencies of the anti-symmetric transverse modes coincide with the frequencies of the symmetric axial modes, and conversely, the frequencies of the symmetric transverse modes coincide with the frequencies of the anti-symmetric axial modes (Burgess 1998).

There remains to discuss any deviations to the above values to account for a cable's inclination: let θ denote the inclination angle with respect to the horizontal; then the frequencies of the anti-symmetric modes can be shown to be (Irvine 1981, and Triantafyllou 1986):

$$\omega^*_{\text{anti-sym},n} = \frac{2n\pi}{L_*}\left(\frac{T_*}{m}\right)^{\frac{1}{2}} \tag{3.9}$$

Similarly, the frequencies of the symmetric modes can be obtained as the solutions to the modified transcendental equation:

$$\tan\left(\frac{\hat{\omega}^*}{2}\right) = \frac{\hat{\omega}^*}{2} - \frac{4}{\lambda^2}\cdot\left(\frac{\hat{\omega}^*}{2}\right)^3 \tag{3.10}$$

where:

$$L_* = L\cdot\sec\theta \tag{3.11}$$

$$T_* = T\cdot\sec\theta \tag{3.12}$$

$$\omega^*_{\text{sym},n} = \frac{\hat{\omega}^*}{L}\sqrt{\frac{T_*}{m}} \tag{3.13}$$

$$\lambda^2_* = \left(\frac{mgL_* \cos\theta}{T_*}\right)^2 \cdot \frac{E \cdot A \cdot L_*}{T \cdot L_{e^*}} \tag{3.14}$$

$$L_{e^*} = L_*\left(1 + \frac{1}{8}\left(\frac{mgL_* \cos\theta}{T_*}\right)^2\right) \tag{3.15}$$

The angle of inclination of Cable#24, taken from the original bridge drawings, is 21.98 degrees. Based on the above modified equations, the following frequencies are calculated for the inclined Cable #24:

Table 3.3 First 6 natural frequencies for Cable #24 (inclination taken into account)

Inclined Natural Frequencies (rad/sec)		
n	**ω (sym)**	**ω(anti-sym)**
1	3.47	6.93
2	10.40	13.87
3	17.33	20.80

It might also be worthwhile to calculate what the expected inclined frequencies would have been using the designed tension force of $T = 1018 kips$.

Table 3.4 First 6 natural frequencies for Cable #24 using design tension

Inclined Natural Frequencies (rad/sec)		
n	**ω (sym)**	**ω(anti-sym)**
1	3.64	7.27
2	10.91	14.55
3	18.18	21.82

3.3.2 Parametric excitation preliminaries

Our working hypothesis is that the aerodynamic instability (or even any wind-induced vibration) of the deck produced the observed large-amplitude

cable motion. Thus, we provide next an insight into the dynamic behavior of a taut flat string under periodic excitation of one of its supports, as a prelude to establishing the actual Cable #24 motion under deck parametric excitation. We assume vertical sinusoidal movement of the support with an Ω driving frequency. The initial-and-boundary-value problem can be stated as: find $w(x,t)$ such that:

$$\frac{\partial^2 w(x,t)}{\partial x^2} = \frac{1}{c^2} \cdot \frac{\partial w(x,t)}{\partial t^2} \tag{3.16}$$

with boundary/initial conditions:

$$w(x,0) = w'(x,0) = w(l,t) = 0 \quad w(0,t) = W_0 \sin(\Omega t) \tag{3.17}$$

where c denotes the speed of wave propagation along the cable,

$$c = \sqrt{\frac{T}{m}} \tag{3.18}$$

and W_0 denotes the excitation amplitude. Using Laplace transforms of both the governing wave equation and of the boundary conditions, separation of variables for the resulting boundary value problem, and, subsequently, inverse Laplace transforms on the Laplace-domain solution, the following time-dependent expression is obtained for the transverse displacements:

$$w(x,t) = W_0 \left[\sum_{k=0}^{\infty} H(t-\alpha_k) \sin \Omega(t-\alpha_k) - \sum_{k=0}^{\infty} H(t-\beta_k) \sin \Omega(t-\beta_k) \right] \tag{3.19}$$

In the above, H denotes the Heaviside function, and the terms α_k, β_k are given as:

$$\alpha_k = \frac{2Lk + x}{c} \tag{3.20}$$

$$\beta_k = \frac{2L(k+1) - x}{c} \tag{3.21}$$

Equation 3.19 represents trains of waves propagating from the moving support to the fixed end of the string, being reflected at the fixed end, and constructively and destructively interfering with each other to form standing waves (Hartono 2004). For example, Figure 3.5 shows the animated string/cable response for a unit amplitude base motion (and unit values for the velocity c, the length L, and the driving frequency $\Omega = 1$ rad/sec).

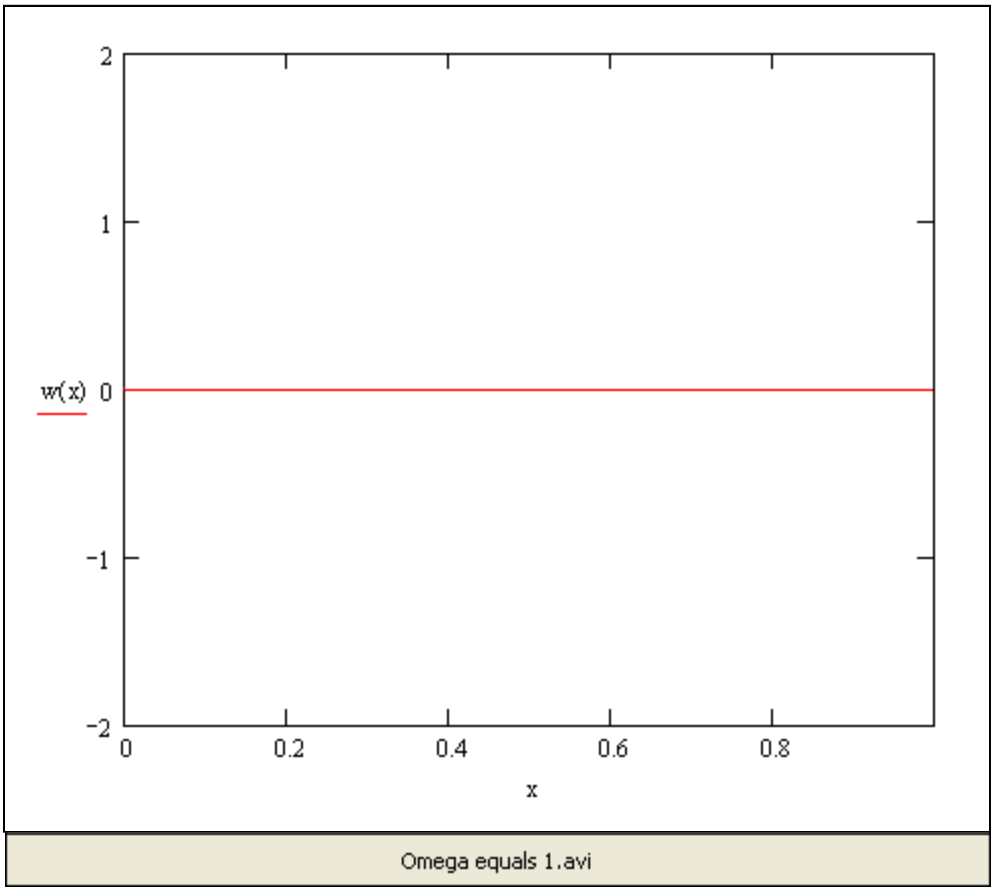

Figure 3.5 Cable oscillations for $\Omega = 1$ rad/sec

Clearly, the motion amplitude remains bounded, while the incident and reflected wave are discernible. Notice, by contrast, the animated cable response shown in, Figure 3.6 which corresponds to a driving frequency Ω that coincides with the first (anti-symmetric) natural frequency ($\Omega = 2\pi$): a standing wave is produced with increasing amplitude.

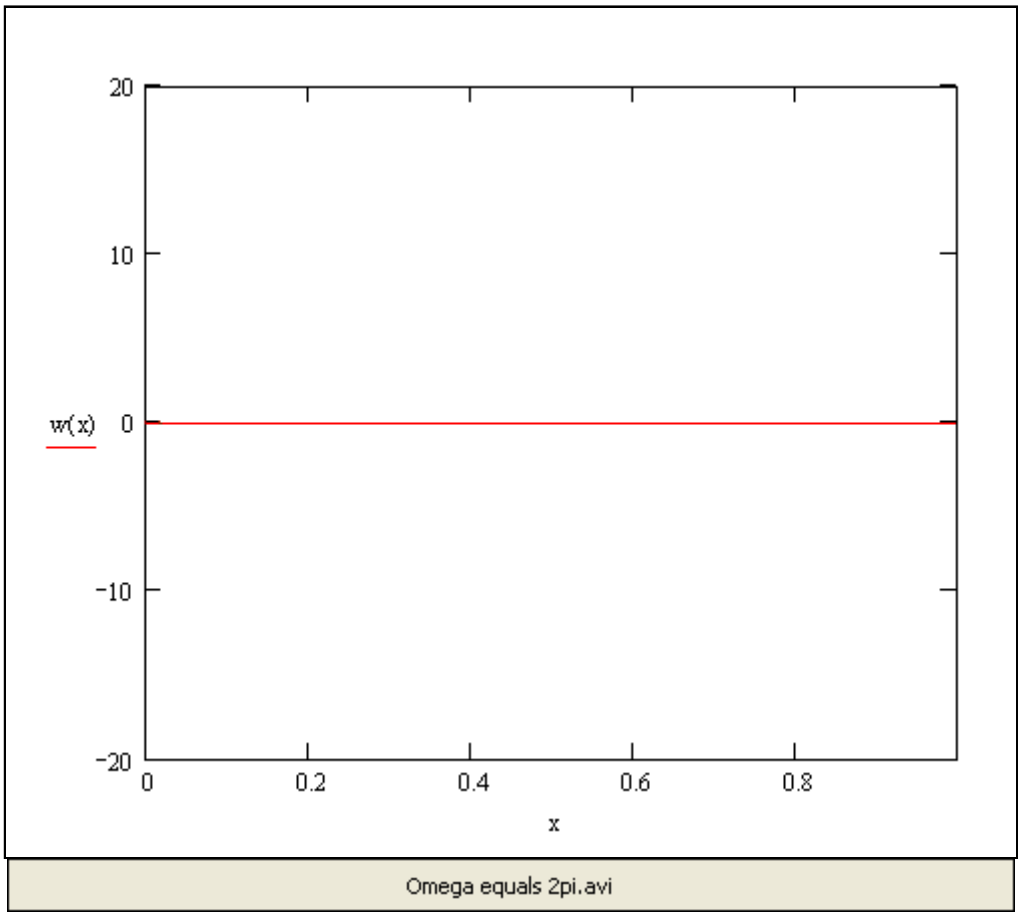

Figure 3.6 Cable oscillations for $\Omega = 2\pi$

The exhibited motion closely resembles the motion of Cable #24 observed in the field (Figure 3.19). Armed with this insight, we will attempt next to reproduce computationally the field behavior of Cable #24.

We remark that for an inclined cable and under a vertical deck motion, both axial and transverse modes will be excited, since there are motion components along both the axial and the perpendicular to the cable directions. Even if the axial inertia effects were to be neglected (they are usually small), the resulting governing partial differential equations are nonlinear, since the elastic effects can not always be uncoupled from the geometric effects. For a taut cable (small λ^2) the decoupling is valid, in which case the preceding analysis is sufficient (usually the case with stay-cables; not true for suspended bridge cables). If, however, the effects cannot be uncoupled, there result Mathieu- (or Hill-) type equations (second-order with quadratic and/or cubic nonlinearities), which can only admit approximate solutions (see, for example, Lilien and Pinto da Costa, 1994, and Pinto da Costa et al, 1996, for the specific case of parametric excitations). In these cases, prior research (e.g. Lilien and Pinto da Costa, 1994) suggests that resonance can occur at driving frequencies that follow:

$$\Omega = \frac{2}{k}\omega_n, \qquad 3.22$$

where k is an integer and ω_n is a natural frequency of the cable (whether of the symmetric or anti-symmetric type). Thus, the instability/resonance region starts, for a given natural frequency, at twice the frequency, and becomes clustered as k increases: instability/resonance can occur even at very low deck excitation frequencies and still excite a cable's fundamental mode. We also remark that, by contrast to the simple case of a flat taut string parametrically excited that we discussed above, the nonlinearities and the damping present in an actual cable help alleviate the instability, without however preventing large-amplitude motion.

3.3.3 Cable # 24 computational model and bending stress profile

3.3.3.1 Qualitative discussion of prior work

In prior work (Willox, 2000), the cable motion was approximated by the 3rd symmetric mode shape assumed to have been induced by wind-rain effects on the cables themselves, absent of any deck/tower movement. This approach was based on the reports described earlier (Poston, 1998) for the video in question, which suggests, as already described, the presence of a standing wave (possibly first anti-symmetric mode).

Moreover, the assumption that there was no vertical displacement of the bridge deck at the location of the cable anchorage was previously used as a simplified assumption. Having stood on the bridge deck during good weather conditions and seen clear visual indications of vertical differential displacement between the two independent decks would seem to indicate that during light wind and rain conditions, and prior to any vibration mitigation, it is reasonable that in fact there were displacements occurring at the deck. In addition to these general observations, measurements taken on the bridge support the concept of deck movement and subsequent cable excitation (Jones, 2003). Figure 3.7 illustrates an instance of symmetric wave excitation which was the foundation for the approach used by Willox.

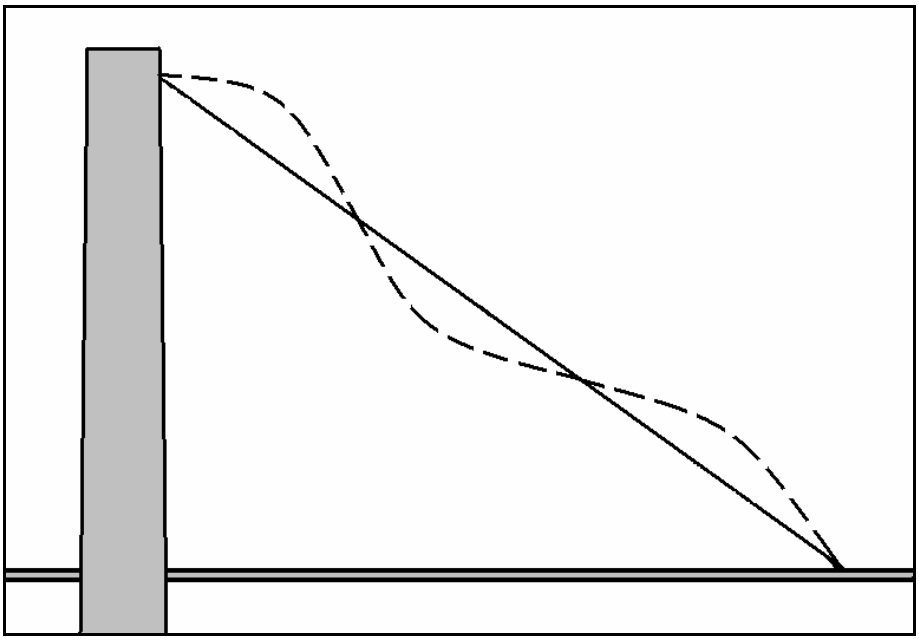

Figure 3.7 Symmetric oscillations assumed to have been induced by wind-rain (per Willox 1998)

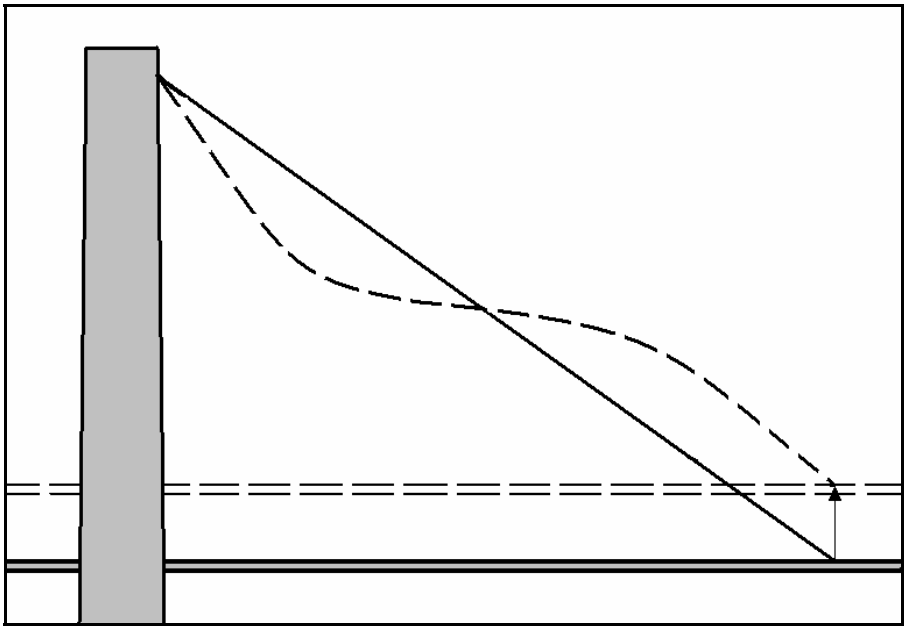

Figure 3.8 Present working hypothesis – Deck movement

The fatigue stress range due to bending stresses calculated under the 3rd symmetric mode shape assumption was 183.6 ksi, implying a cyclic fatigue life of about 45 minutes for the strands (Willox, 1998).

The following analysis departs from prior assumptions, and based on the hypothesis of deck movement, attempts to provide new estimates for the range of bending stresses that correspond to the observed motion of the 6:41 am and 6:55 am videos.

3.3.3.2 Quantitative analysis of bending stresses in cable #24

In an attempt to reproduce the observed dynamic behavior of Cable #24, a finite element model was developed using the general-purpose commercial software package ANSYS. Prior to presenting the model details, we discuss (imperfect) means for evaluating the computational solution based again on the video recording.

Upon inspection of the anti-symmetric excitation in the video it appears that there is a point close to the uppermost restrainer clip, 210 ft from the tower face (per the original bridge drawings), that exhibits the largest observable peak-to-peak displacement. In order to determine the value of this displacement, a closer look was taken at individual frames of the video exhibiting the maximum and minimum displacements. Using the pixels of the video as a unit of measurement, relative distances were measured from the restrainer clip to the top corner of the tower. The top corner of the tower was used because it serves as a stationary point of reference. The change in distance from the restrainer clip to the corner of the tower between the maximum and minimum displacements roughly represents the peak-to-peak amplitude of motion for this point along the length (see Figure 3.9).

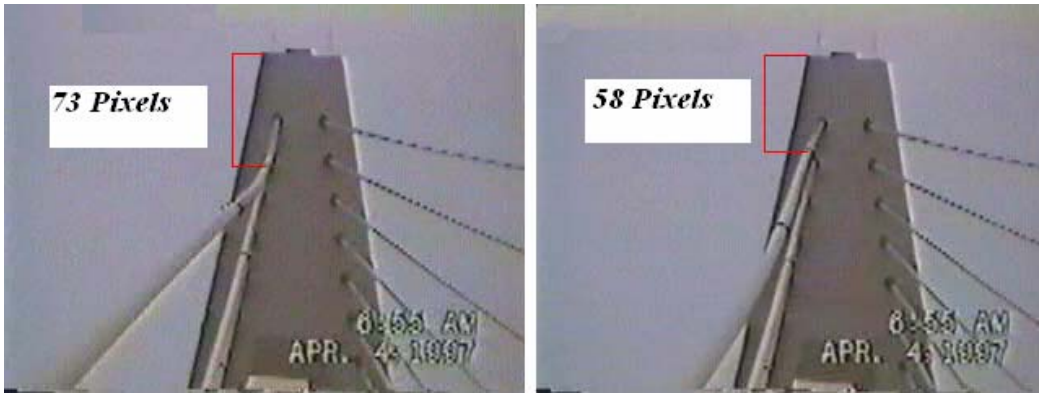

Figure 3.9 Relative peak-to-peak displacement

In order to translate the number of pixels into physical lengths, a known dimension in the video was measured in pixels. The width of the top restrainer clip, which is equal to the outer diameter of the PE pipe was used. This distance was measured as 4.00 pixels in the video frames. With the actual outer diameter of the PE pipe at that location equal to 6.30 in, this implies that each screen pixel at that point in the perspective shot was approximately equal to 1.58 in. Then, it can be shown that the peak-to-peak displacement at the restrainer clip was 23.6 in, or essentially ±11.8 in. This estimated value of peak-to-peak displacement in the video will be compared with the value for peak-to-peak displacement at the corresponding nodal point obtained using the ANSYS steady-state solution. While this is an approximate method, and a more in-depth digital analysis would provide a more accurate estimate, this approximate value obtained leads to a good correlation of the FEA response and that seen in the video, as will be described subsequently.

3.3.3.3 Cable #24 finite element modeling

A finite element ANSYS model was developed based on the actual size and geometry of Cable #24 in order to model its dynamic response as the cable

was displaced cyclically (sinusoidal excitation) at its deck anchorage termination. The goal of this analysis was to match the dynamic behavior observed on the cables as best as possible. Once a good match was made then bending stress range could be derived from the dynamic response.

BEAM3 elements were used and their geometries and sectional properties were based on the transformed properties of Young's modulus and moment of inertia calculated in Appendix A for both the free length and the anchor head of the cables. BEAM3 elements allow for the calculation of flexural forces at the nodes as well as initial strain and material self-weight density inputs. The smeared properties used were based on the dimensions of the cables taken from the original bridge drawings.

A total of 1319 BEAM3 elements were used along the discretized length of the cable. The length of the cable is divided into 2 distinct sets of different element sizes. In the majority of the free-length the elements are 6 in long and have the smeared section properties of the free-length section. Within a foot of the anchor head the elements are 1 in long and have the smeared section properties associated with the anchor heads as calculated in the Appendix A for the deck anchorage as seen below. While this is an approximation of the anchorage sectional properties, the anchorage region has little effect on the overall dynamic behavior of the cable. The increase in moment of inertia within a foot from the termination is done to merely to ensure the bending moment is accurate at this region in order to later calculate bending stresses.

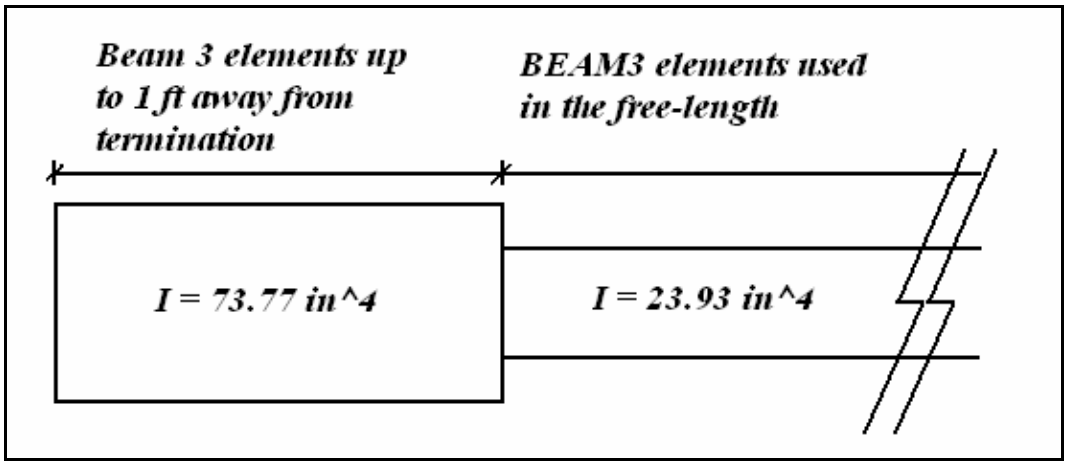

Figure 3.10 FEA approximation of moments of inertia in the deck anchorage

The plan drawings would seem to indicate that the tower termination is fixed out into the free-length cross-section and as such the free-length transformed properties are used at that location in the model as seen in the image taken from the structural drawings below.

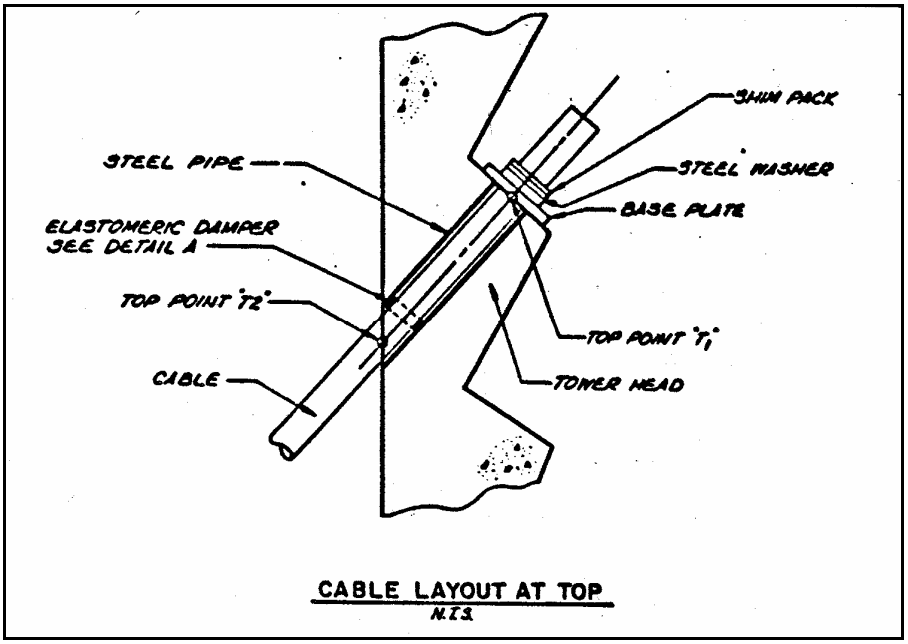

Figure 3.11 Termination at tower

The BEAM3 elements have an initial strain of 0.00194 to account for the tension force of 925 kips which was determined via pluck tests done previously (Poston, 1998).

The boundary conditions of the model were such that there was perfect fixity at the tower end, whereas at the deck anchorage there was no rotation and no translation in the horizontal direction; a sinusoidal excitation along the vertical direction was applied at the deck anchorage to account for the deck's movement (Figure 3.12).

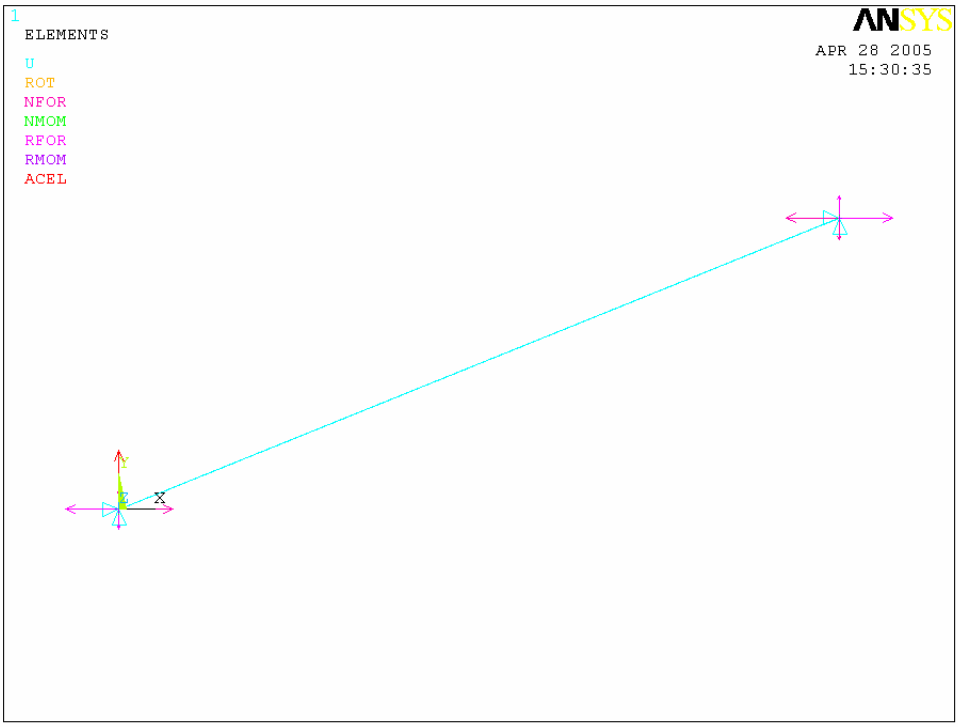

Figure 3.12 Cable boundary conditions

3.3.3.4 Cable #24 static/modal response

Before running the dynamic analysis in ANSYS, static and modal analyses were performed. In order to perform a modal analysis in ANSYS using elements

that have an initial strain, a static test must be run prior to the actual modal analysis with "stress-stiffening" turned on. Based on this analysis it was found that the 1st anti-symmetric natural frequency for the inclined cable was 7.28 rad/sec which was in good accord with the closed form solution obtained earlier (Table 3.2 and Table 3.3). In the dynamic analysis that follows, this frequency will be used as the operating frequency at the deck anchorage to simulate resonance conditions (can also be seen as a revamped estimate of the deck's movement).

3.3.3.5 Cable #24 transient analysis

The objective in this analysis was to match the maximum estimated peak-to-peak displacement (see section 3.3.3.2) observed in the videos along with the 1st anti-symmetric mode shape behavior. Using the frequency obtained in the modal analysis a sinusoidal displacement was applied at the deck anchorage to re-create the desired dynamic behavior seen in the video. The only factor that needed to be calibrated was the amplitude of the displacement at the anchorage. This value was adjusted until the peak-to-peak displacement at the node in the model corresponding to the position of the uppermost restrainer clip matched the estimated displacement.

In order to most realistically recreate the videos the two cables next to Cable #24, Cables #23 and #22, were also included in the analysis. From the recording it appears the motion of Cables #23 and #22 is not as dramatic as that of Cable #24, implying that resonance conditions may not have been met for these cables or that the restrainers have limited their response (if they were not broken; though hard to decipher from the video, it appears that these restrainers were broken too). The dynamic properties were calculated for these cables through the

same means used for Cable #24. These properties are listed in the following tables.

Table 3.5 Dynamic properties of cables #22 & #23

Dynamic Properties					
Cable	**n**	**γ**	**λ^2**	**ω-sym (rad/sec)**	**ω-anti sym (rad/sec)**
#22	1	274.894	0.31462	4.32	8.65
	2	-	-	12.97	17.30
	3	-	-	21.62	25.94
#23	1	280.942	0.50051	4.04	8.08
	2	-	-	12.12	16.16
	3	-	-	20.20	24.24

The application of a cyclic displacement at the bottom node was done in ANSYS through the use of its built-in function generator. It was determined that the displacement necessary to achieve results closest to what was described was 7.4 in. Figure 3.13 shows how this equation was entered into the function generator. After the equation is entered into the function generator ANSYS applies the cyclic displacement based on that function of time. The same excitation was also applied to cables #23 and #22.

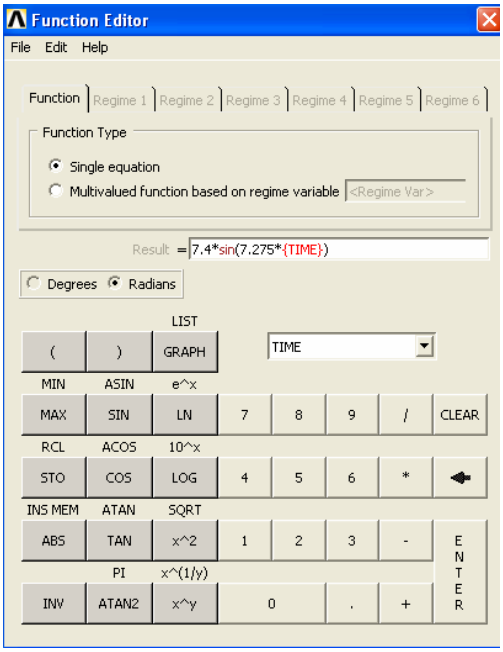

Figure 3.13 Function generator input

A "Large-Displacement Transient Analysis" was run in ANSYS with stress-stiffening turned on to account for the initial tension force in the cable and nonlinear effects including sagging, and dynamically modified cable tension. The analysis was run for 45 seconds in order to allow for the standing wave to form and to allow sufficient time for instabilities, if any, to develop (the total time corresponds to the initial disturbance having traveled 78 times up and down the cable's length). The solution controls were adjusted such that the data from every one of the 750 substeps was saved. This was done so that an accurate time-history of the analysis would be available to create animations for comparison to the video and so that it would also be possible to determine the exact times of peak bending moments in the terminations.

The primary goal of the ANSYS dynamic analysis is to correlate the computational model with the observed dynamic behavior in the video. In order to assess the accuracy of the ANSYS model we must examine the peak-to-peak

displacement at the node corresponding to the restrainer ring position. Figure 3.14 is a complete time history of the displacement at this node (node #928).

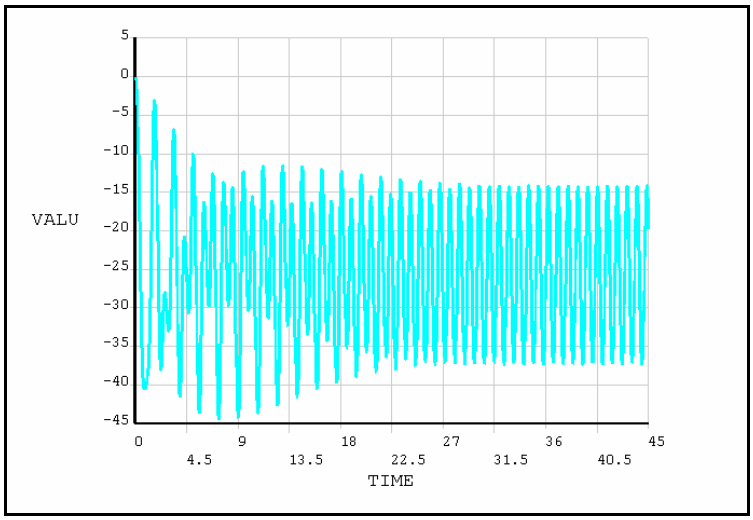

Figure 3.14 Total displacement time-history for "restrainer-clip" node #928

Figure 3.14 shows that the steady-state response begins to dominate after around 30 seconds of activity. As such in order to calculate the peak-to-peak displacement at this node during steady-state we can take a closer look at, for example, the last 5 seconds of the analysis. Figure 3.15 illustrates this point.

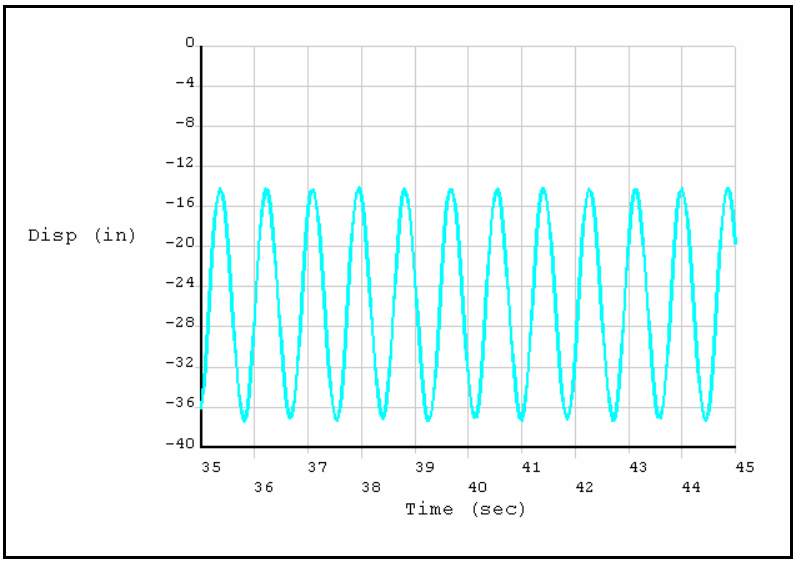

Figure 3.15 Steady-state displacement of "restrainer-clip" node928

The exact peak values of displacement at node #928 were calculated in the ANSYS general post-processor as 37.61 and 14.05 inches, which would give us a peak-to-peak displacement of ±11.79, which is approximately equal to the measured peak-to-peak displacement of ±11.81 inches calculated in section 3.3.3.2.

Having matched the estimated amplitude of displacements at the position of the restrainer clip seen in the video, it was also important to check the qualitative behavior of the ANSYS analysis. In order to best do this a 3D animation was developed in ANSYS based on the solution data obtained and compared to the actual video. Frames of the animation are compared to the actual video frames in Figure 3.16.

Figure 3.16 Frame-to-frame comparison of video and animation

It is possible in ANSYS to move the location of the animation perspective as well as the focal point of the images. The ANSYS animation was created with the position of the "camera" in ANSYS located at the most likely position of the actual cameraman who shot the original video. Figure 3.17 shows a series of sequential frames of the ANSYS animation in question.

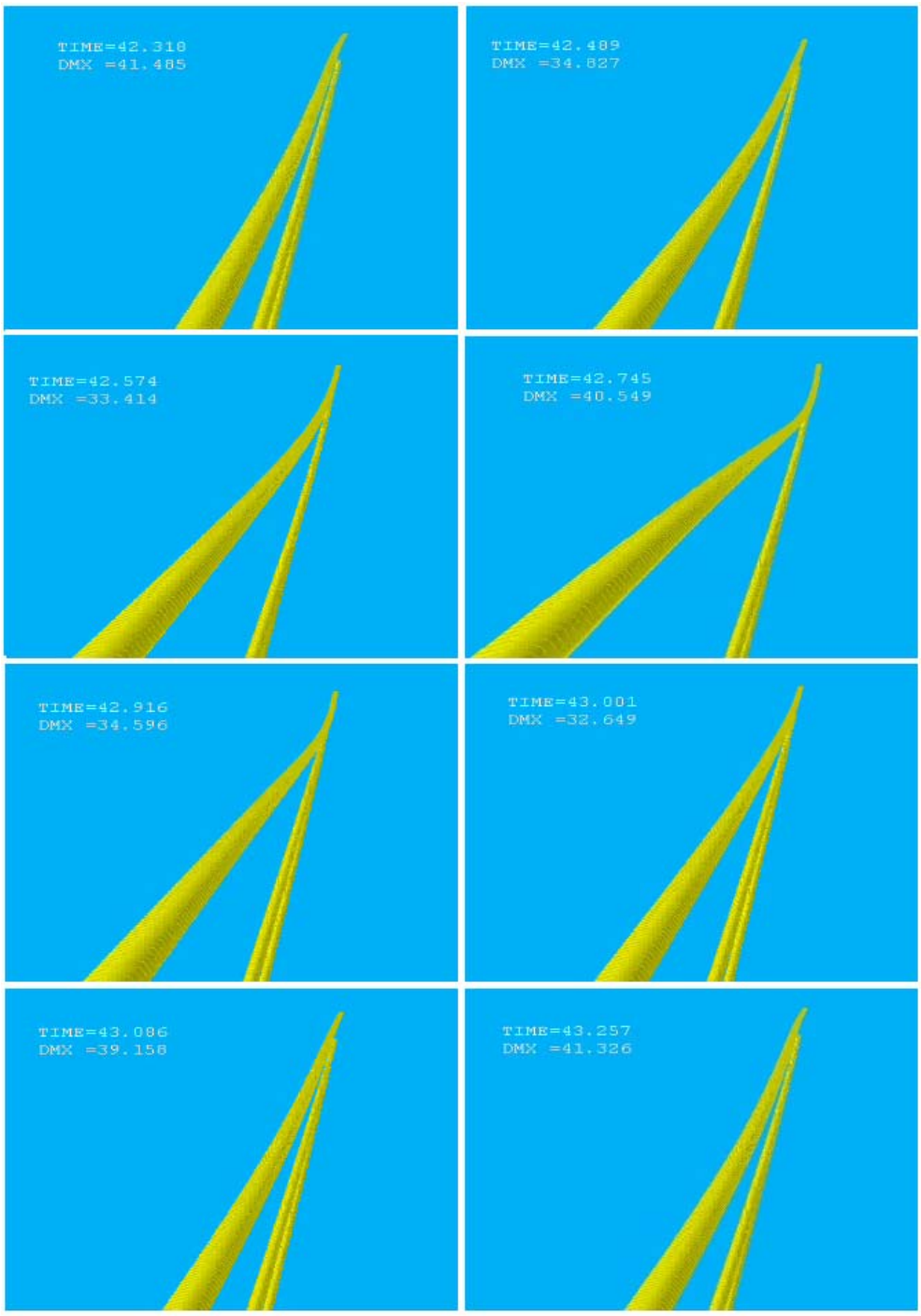

Figure 3.17 Frames of cable #24 response animation

The complete animation can be seen in Figure 3.18 below.

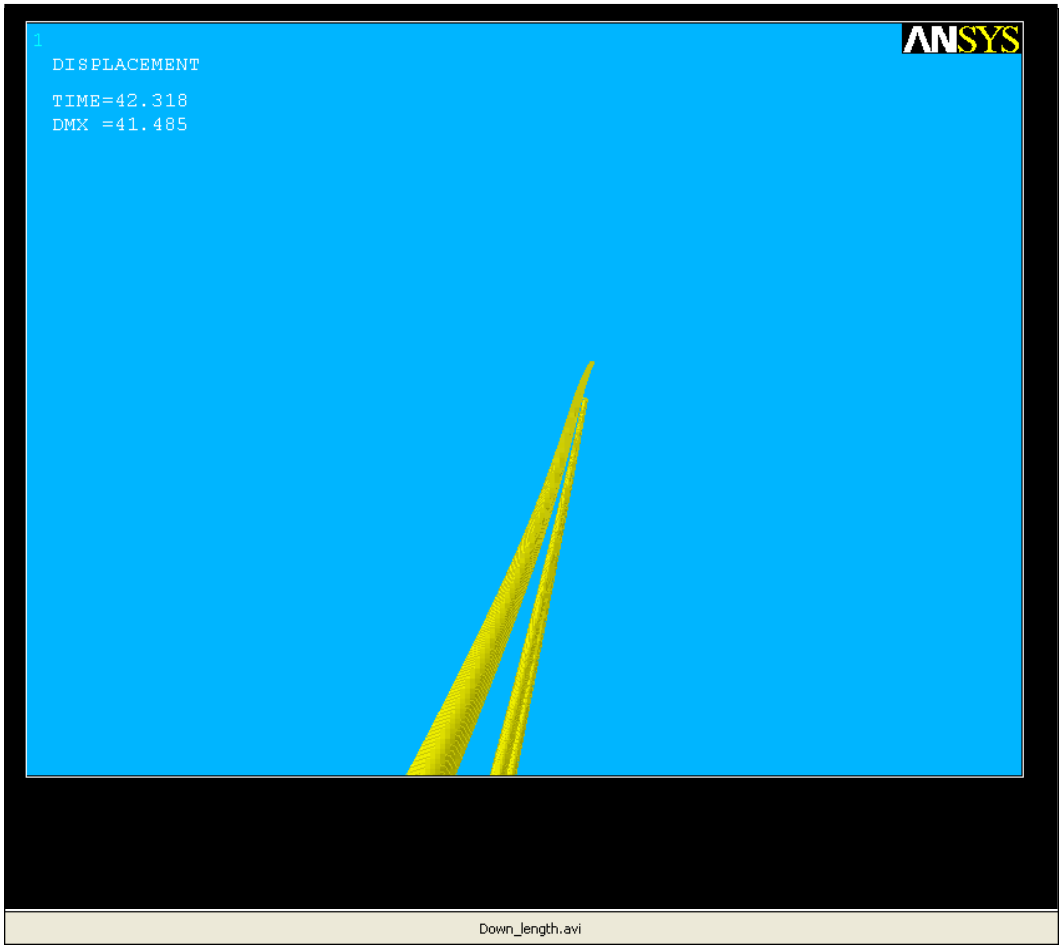

Figure 3.18 ANSYS animation looking up from deck towards tower

Another animation was made to further correlate the solution based on video taken from the side of the deck. This video is of the same cables as seen in the previous video but viewed approximately 78 ft (other side of the deck) which provides a more orthogonal view of the cable vibrations and demonstrates more clearly the dominance of the 1st anti-symmetric mode shape. The actual video recording can be seen in the figure below (Figure 3.19), whereas the ANSYS complete animation can be seen, for comparison, in Figure 3.20**.**

Figure 3.19 Video taken from other side of the deck

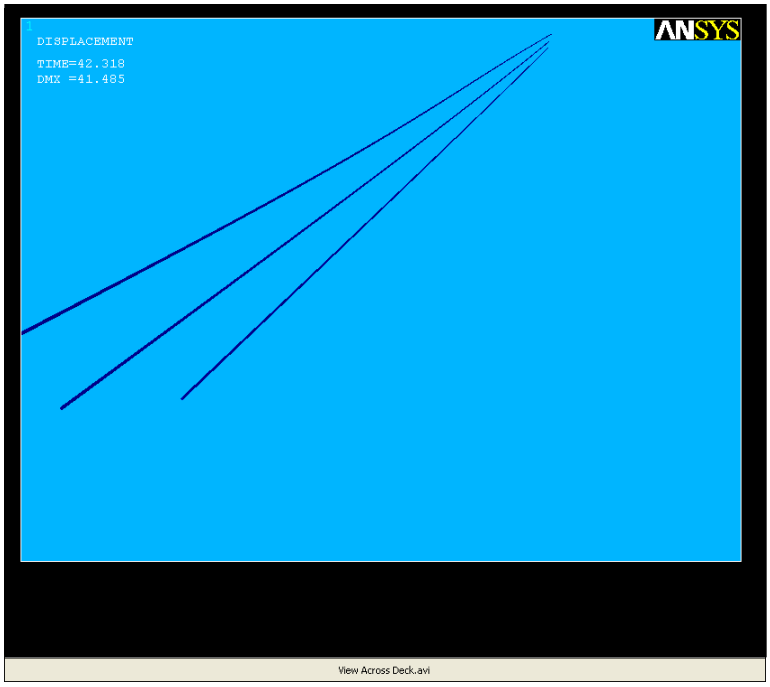

Figure 3.20 ANSYS animation from camera position across deck

3.3.3.6 Cable #24 bending moments and stresses

Now that we have matched the ANSYS response to the video field observations we can examine the ANSYS solutions for cyclic bending moments at the terminations.

The following images are the 45 second time-histories for the bending moments at the deck and tower anchorages, respectively. One can observe the effects of the transient response fading out and the steady-state response dominating.

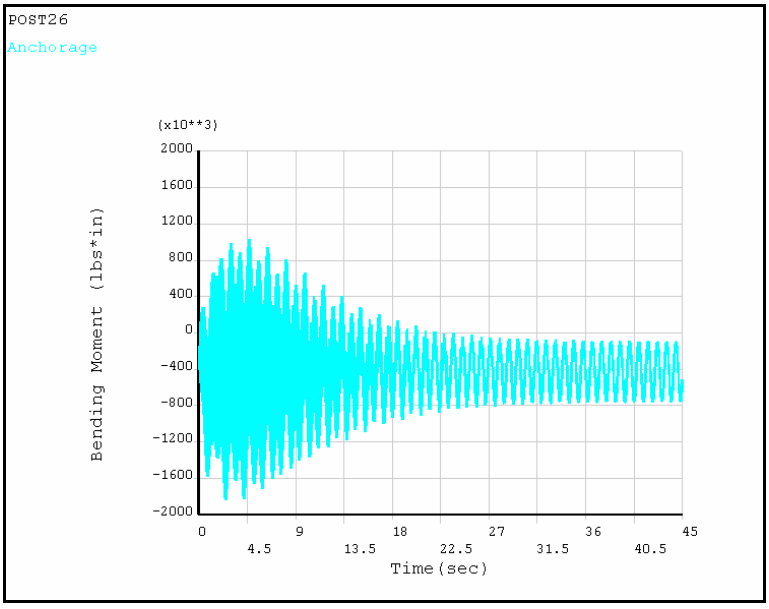

Figure 3.21 Bending moment at the deck anchorage vs. time

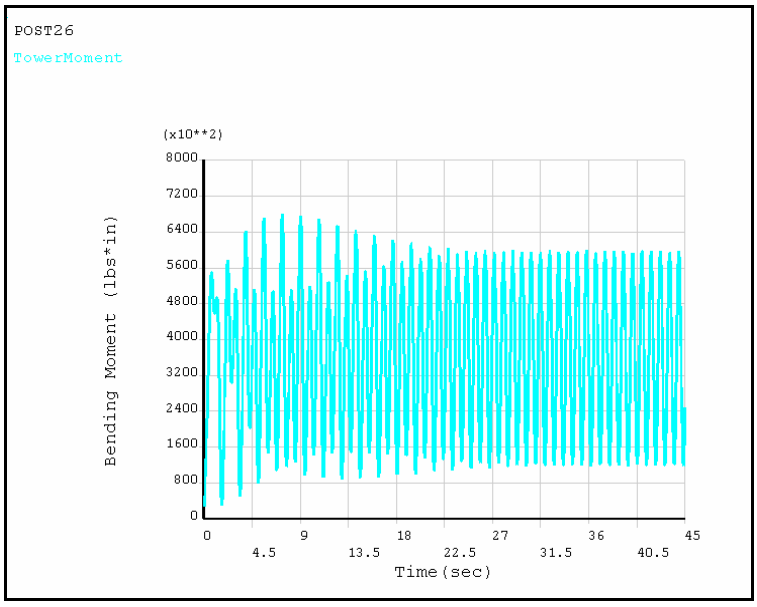

Figure 3.22 Bending moment at the tower face vs. time

In order to evaluate the steady-state range of bending moments in the cables a closer look was taken at the last 10 seconds of the response for each case.

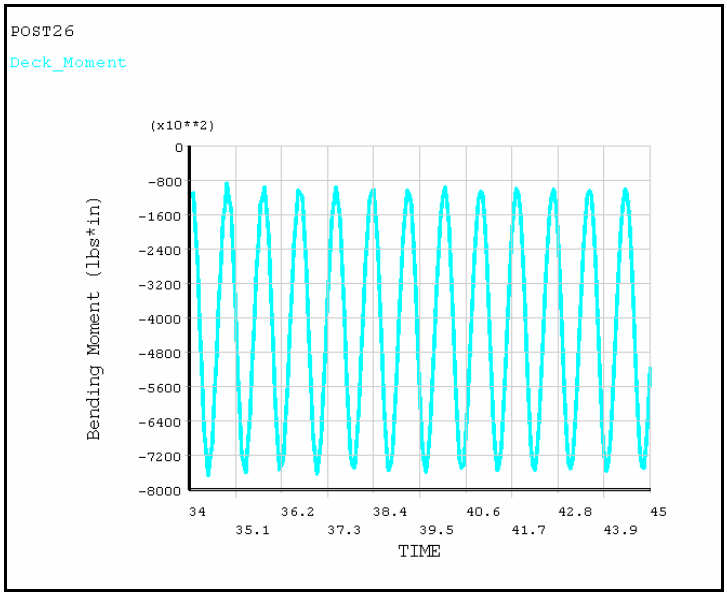

Figure 3.23 Bending moment at deck anchorage vs time (35-45 sec)

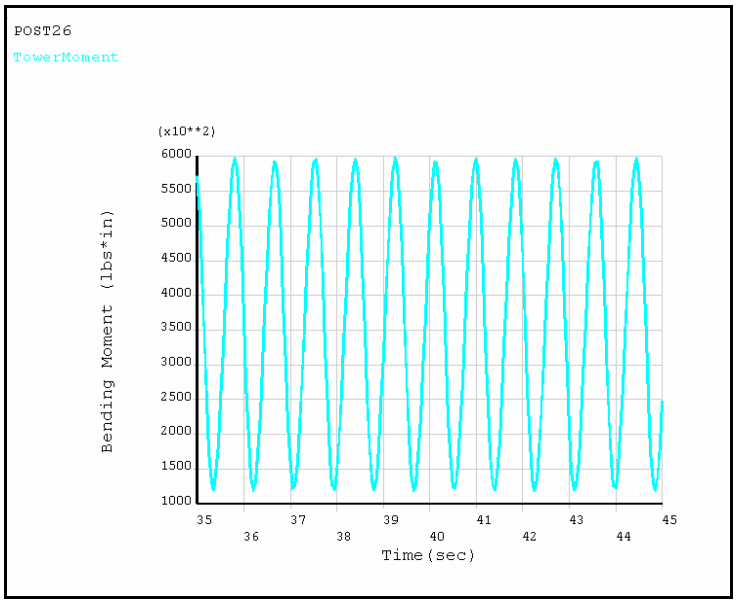

Figure 3.24 Bending moment at tower anchorage vs. time (35-45sec)

As seen in the previous figures there is a clearly defined range of bending moments at the deck and tower terminations defined by the maximum and minimum bending moments there. Using the general post-processor in ANSYS the maximum and minimum values of bending moment were obtained and used to determine the subsequent range of bending moments as seen in Table 3.6.

Table 3.6 Bending moment range for deck and tower anchorages

Bending Moments (kip*in)				
Location	**Max.**	**Min.**	**Total Difference**	**Range**
Deck	94.10 (-)	765.6 (-)	671.5	± 335.8
Tower	657.3 (+)	133.6 (+)	523.9	± 262.0

With ranges for bending moments obtained from the dynamic model the level of stress in the steel strands of the cable's cross-section can now be ascertained. These values are obtained using the full, un-cracked smeared properties (Appendix A), which is a reasonable assumption based on field observations of the condition of the grout (Willox, 1998 and Dowd, 2001).

$$\sigma_{Deck} = \frac{\pm(335.8kip \cdot in) \cdot (3.88in)}{(73.77in^4)} = \pm 17.66ksi \qquad 3.23$$

$$\sigma_{Tower} = \frac{\pm(262.0kip \cdot in) \cdot (2.5in)}{(23.93in^4)} = \pm 27.37ksi \qquad 3.24$$

We now have obtained a bending stress range that can be used as a model for the experimental test setup to be described in further detail in Chapter 5.

CHAPTER 4
Computational Modeling of Laboratory Experiments

A series of twelve laboratory fatigue tests have been performed at the Ferguson Structural Engineering Laboratory at the University of Texas at Austin over the course of the last few years aimed at studying the effect the large-amplitude vibrations may have had on the stay-cables of the Fred Hartman Bridge. In this chapter we review this prior experimental work and discuss appropriate computational models that describe satisfactorily the experimental results.

4.1 LABORATORY EXPERIMENTS

4.1.1 Preliminaries

The actual specimens tested were similar to the bridge's smallest cables (so-called Group-5). The loading and displacement parameters used for the testing procedure were developed in preliminary finite element analysis (Dowd 2001) that was, in turn, based on the previously estimated field motion (±21 in peak-to-peak displacement and 3rd symmetric mode) as the latter was estimated from the video recording. We remark that the estimates obtained from the videos taken at 6:41 am and 6:55 am have been revised in this work.

4.1.2 Experiment overview

Poser (2001) designed a test setup for the full-scale bending fatigue tests that began in 2000 and were later continued by Ridd (2004**)**. Specimens #1

through #4 were tested by Poser; however information about testing results from the first two specimens are included in the thesis (Poser, 2001). Specimens #5 through #10 were all tested by Ridd and the results for all of those tests are discussed in her thesis (Ridd 2004). The final two tests were conducted in the summer of 2004.

In general, there were two types of 19-strand arrangements, and one type of 13-strand arrangement used for the steel strands throughout the testing sequences; those are shown in Figure 4.1, Figure 4.2, and Figure 4.3.

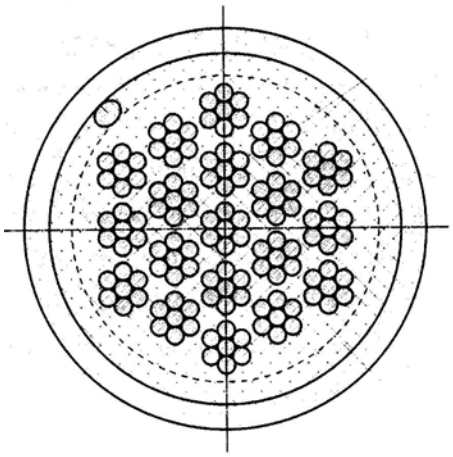

Figure 4.1 Strand arrangement – specimen #1

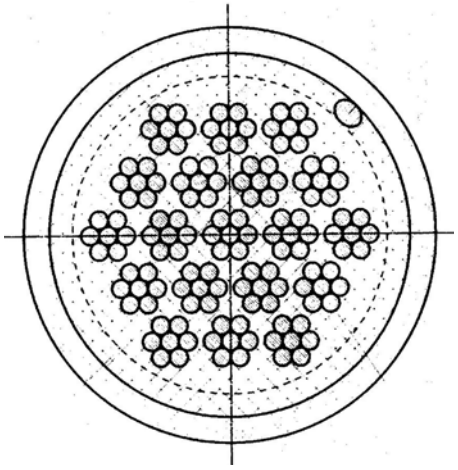

Figure 4.2 Strand arrangement – specimen #2-5, 7-12

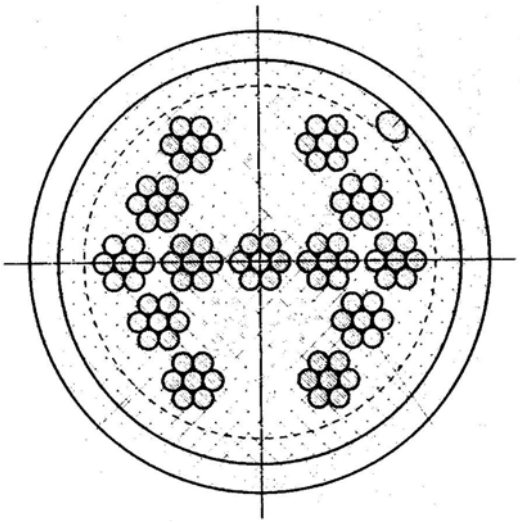

Figure 4.3 Strand arrangement – specimen #6

All of the specimens were wrapped with a helical wire and placed into a polyethylene (PE) pipe with transition regions near their ends consistent with the design of the actual cables (Poser 2001). At these terminations or, anchor heads, the cross-sectional area of the cable is much wider, with the strands splayed out into the seating wedges, typical for any pre-stressed tendons.

4.1.2.1 Material properties - steel strands

The steel strands were 0.6 in nominal diameter 7-wire strands composed of 270 ksi high-strength steel, the same type used in typical prestressing applications. There were two types of strands used in the tests, denoted as Type A and Type B (Ridd, 2004). The basic material properties for the Type A strands were used throughout this thesis and can be seen in Table 4.1. The nominal area of an individual steel strand as given in the strands mill certificate is $0.217 in^2$, which is the value used in all subsequent calculations. Furthermore, the 6 outer wires of the strand are wrapped around the length of the center wire.

Table 4.1 Material properties of steel strands (units are English unless bracketed)

ASTM A416 - Seven-Wire Uncoated Strand - MINILAX [low relaxation]							
Grade	Nominal Strand Diameter	Strand Tolerance	Minimum Breaking Strength Lbs (kgs)	Min Yield Strength at 1% extension	Minimum elongation @24" gauge	Nominal area In^2 [mm^2]	Nominal weight Lbs/1000ft kg/1000m
270K	0.6"	0.6102/0.5941 [15.50/15.09]	58,600 [26,580]	52,740 [23,922]	3.5%	0.2170 [140.00]	740 [1,102]

4.1.2.2 Material properties - cement grout

For the grouted specimens, the steel strands are placed inside a grout matrix to better protect the strands from potential corrosion. The addition of the grout also plays an important role in increasing the cables' flexural rigidity. The cement grout is composed of Type I Portland cement and tap water at a ratio of water-to-cement equal to 0.42. An admixture was also used. The Young's modulus was computed to be 3500 ksi (Poser 2001) with a tensile capacity of 474 psi.

4.1.2.3 Laboratory setup

The design for the experimental setup is described in detail in (Poser 2001) and (Ridd 2004). Herein, for reference purposes we reproduce only the basics of that setup: the following figures, Figure 4.4, Figure 4.5, Figure 4.6, and Figure 4.7 (Ridd 2004) provide the overall details of the laboratory specimens as well as of the test setup.

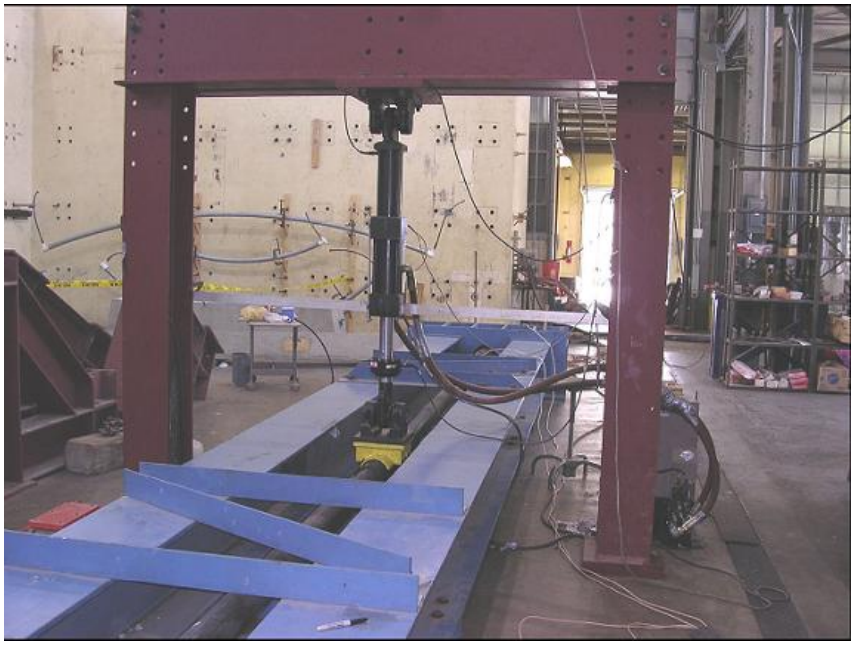

Figure 4.4 Full-scale bending fatigue test setup (Ridd, 2004)

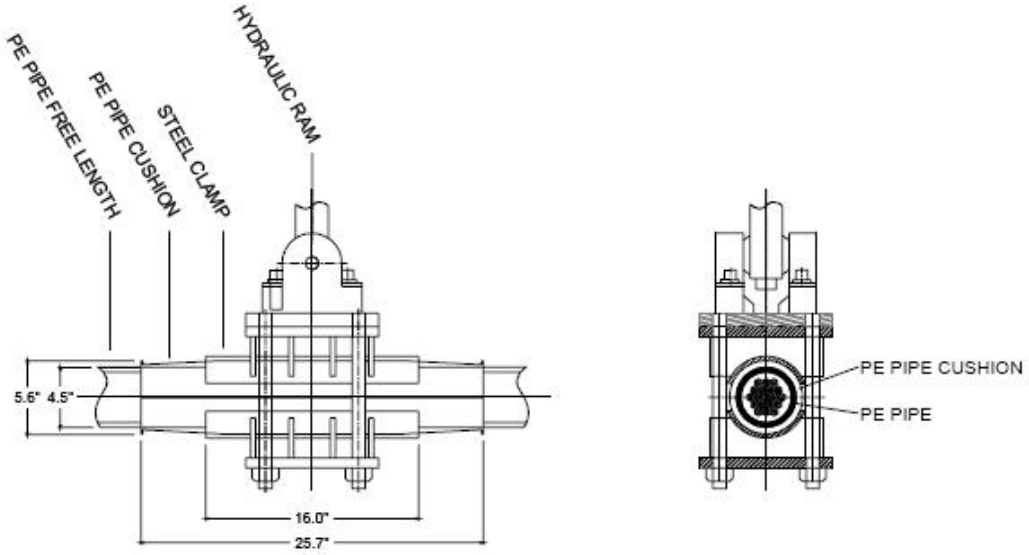

Figure 4.5 Clamp used for loading at mid-span (Ridd, 2004)

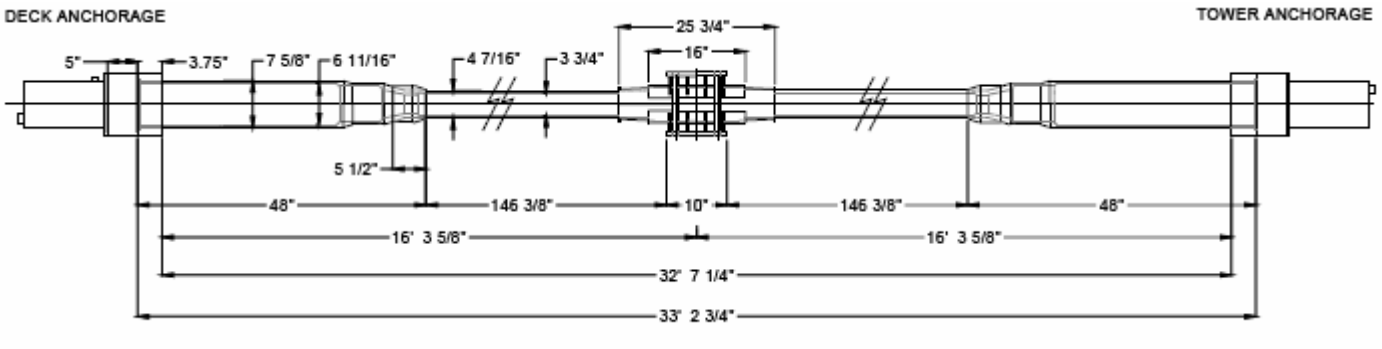

Figure 4.6 Geometry of grouted specimens (Ridd, 2004)

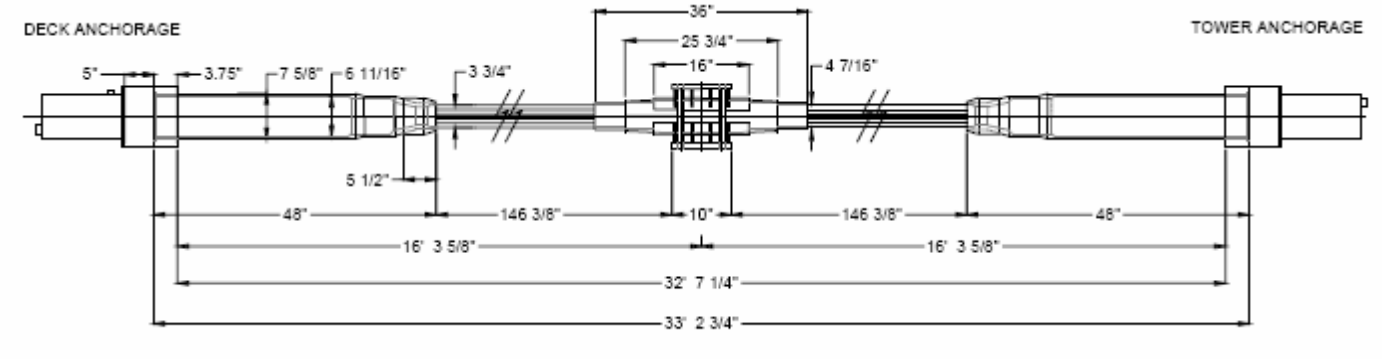

Figure 4.7 Geometry of un-grouted specimens (Ridd, 2004)

Static tests

Before the testing of each stay-cable specimen both Poser and Ridd performed static tests to determine the load-displacement relationship for the various cables. At this point it should be noted that while the majority of the specimens tested by both Poser and Ridd were 19-strand grouted cables, specimens #5 and #8 were ungrouted and specimen #6 was grouted but had only 13 strands. The static test data are listed in Table 4.2

Table 4.2 Load at maximum applied displacement

Stay	Strands	Matrix	Load	Displacement
			(kip)	(in)
1	19	Grouted	7.6	1.6
2	19	Grouted	7.6	1.6
3	19	Grouted	7.5	1.6
4	19	Grouted	4.99	1.1
5	19	Ungrouted	6.53	1.6
6	13	Grouted	5.24	1.6
7	19	Grouted	7.96	1.6
8	19	Ungrouted	6.56	1.6
9	19	Grouted	7.2	1.6
10	19	Grouted	5.28	1.1

The static test data were obtained by recording the actuator load required to displace the mid-point of the specimen 1.6 in, except for specimens #4 and #10, which were only displaced 1.1 in.

4.1.2.4 Overview of fatigue test results

Acoustic monitors were used to determine when wire breaks occurred in the strands and autopsies were performed on the stay-cable specimens after they had been tested to determine the actual locations of wire failures. The following table indicates the total number of breaks per specimen along with an indication

of the cable regions the breaks occurred in (Poser 2001, and Ridd 2004). The tower and deck designations refer to the two anchor heads at the ends of the cable, with the tower and deck ends being the "live" and "dead" ends for prestressing, respectively.

Table 4.3 Wire fracture of fatigue specimens

Stay	Strands	Matrix	Total Cycles	Wire Fractures			
			(millions)	Tower	Center	Deck	Total Breaks
1	19	Grouted	2.81	14	11	0	25
2	19	Grouted	2.87	51	16	1	68
3	19	Grouted	4.96	9	62	14	85
4	19	Grouted	8.78	28	0	3	31
5	19	Ungrouted	5.21	0	0	0	0
6	13	Grouted	6.48	17	11	0	28
7	19	Grouted	2.25	37	65	17	119
8	19	Ungrouted	6.2	2	0	2	4
9	19	Grouted	2.57	12	61	3	76
10	19	Grouted	5.61	23	21	8	52

4.2 COMPUTATIONAL MODELING OF LABORATORY EXPERIMENTS

We compare next the response of the tested specimens, as described above, to closed-form solutions and computational models. The comparison relies primarily on the use of Euler-Bernoulli beam models for the laboratory specimens. The choice of Euler-Bernoulli theory to describe the specimens is due to the fact that all grouted specimens exhibit a relatively low value of γ (Table 4.4), and thus (as per, e.g., Irvine, 1981) beam behavior is dominant (we discuss in detail the behavioral differences based on the γ parameter in the next chapter).

Table 4.4 Specimen γ values

Specimen	γ
1	26.5
2	25.9
3	25.9
4	25.9
6	24.3
7	25.9
9	25.9
10	25.9

Any discrepancies between the actual static test results and the computational models are investigated, and bending stresses are also estimated for the corresponding specimens.

4.2.1 Modeling of grouted specimens

We use the classical Euler-Bernoulli differential equation with a tension load to model all grouted specimens. Accordingly:

$$EI \cdot \frac{d^4 w}{dx^4} - T \cdot \frac{d^2 w}{dx^2} = P \cdot \delta\left(x - \frac{L}{2} \right) + mg \qquad 4.1$$

where E denotes Young's modulus, I is the second moment of inertia, $w \equiv w(x)$ is the transverse displacement , x denotes position, T is the tension force, P represents the applied actuator load assumed concentrated at the midpoint, L is the length of the specimen, mg is the self-weight per unit length, and δ denotes the Dirac function. It is worth noting here that in the actual testing procedure, the sag from self-weight is considered the neutral position and displacements were measured from this position. This analysis assumes the neutral position is prior to the effects of self-weight. Based on the test setup we assume perfect fixity conditions at both anchor heads, or

$$w(0) = w(L) = \frac{dw(0)}{dx} = \frac{dw(L)}{dx} = 0 \qquad 4.2$$

The general solution of the above boundary value problem is:

$$w(x) = -\frac{P}{T}\cdot\left(x-\frac{L}{2}\right)\cdot H\left(x-\frac{L}{2}\right)+\frac{P}{T}\cdot\sqrt{\frac{EI}{T}}\cdot H\left(x-\frac{L}{2}\right)\cdot\sinh\left(\sqrt{\frac{T}{EI}}\cdot\left(x-\frac{L}{2}\right)\right)-\frac{mg}{2T}\cdot x^2$$

$$+c_1+c_2\cdot x+c_3\cdot\sinh\left(\sqrt{\frac{T}{EI}}\cdot x\right)+c_4\cdot\cosh\left(\sqrt{\frac{T}{EI}}\cdot x\right) \qquad 4.3$$

where H is the Heaviside function, and the coefficients c_1 through c_4 are given in Appendix B (they were obtained using the boundary conditions 4.2).

The individual variables in equation 4.1 were all system parameters of the tests. Of these variables the length L was 395.4 in for every test, as the same loading frame was used for all tests. We used smeared section properties to describe the composite cross section in terms of Young's modulus, area, and second moment of inertia. The calculations for the section properties of each specimen can be found in Appendix A. All test and specimen parameters are listed in the table below:

Table 4.5 Static test parameters for grouted specimens

Test	L (in)	E (ksi)	I (in^4)	mg (kips)	P (kips)	Displacement (in)
Stay 1	395.4	27500	3.59	0.862	7.6	1.6
Stay 2	395.4	27500	3.76	0.862	7.6	1.6
Stay 3	395.4	27500	3.76	0.862	7.5	1.6
Stay 4	395.4	27500	3.76	0.862	4.99	1.1
Stay 6	395.4	27500	1.62	0.771	5.24	1.6
Stay 7	395.4	27500	3.76	0.870	7.96	1.6
Stay 9	395.4	27500	3.76	0.870	7.2	1.6
Stay 10	395.4	27500	3.76	0.870	5.28	1.1

We used a symbolic/numerical computation package to obtain the midspan deflection based on equation 4.3 and the test/specimen parameters. The results are summarized in Table 4.6, where a comparison against the actual displacements is also shown.

Table 4.6 Comparison of static midspan deflections for grouted specimens

Displacements				
Stay	**Load (kips)**	**Actual (in)**	**Analytical (in)**	**Difference (%)**
1	7.6	1.60	1.52	5.0
2	7.6	1.60	1.51	5.6
3	7.5	1.60	1.49	6.9
4	5	1.10	1.02	7.3
6	5.2	1.60	1.53	4.4
7	8	1.60	1.58	1.3
9	7.2	1.60	1.43	10.6
10	5.3	1.10	1.07	2.7

4.2.2 Discussion of grouted specimens results

As it can be seen from Table 4.6, there are differences between the computed solutions and the experimentally obtained. In examining the variables involved in the experimental setup it becomes apparent that some of the parameters can be expected to have some inaccuracy in the laboratory, thus affecting the analytical solutions obtained. Parameters of concern are the Young's modulus of the steel strands used, the pre-stressing tension force, and the smeared moments of inertia. In order to better understand how these variables affect the computed solutions we report on the solution sensitivity with respect to parameter variations (± 10%) to see if they could have been responsible for the difference between the solution and the test results. The following figures summarize the observations.

Specimen #1 (Grouted)

Orientation:

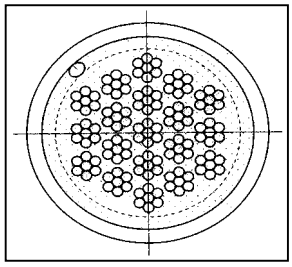

Overall specimen parameters

E (smear)	I (smear)	Length	Tension	Weight
27500 ksi	3.588 in^4	395.375 in	445 kips	.862 kips

Static Test Data

Load (kips)	Disp. (in)	Stiffness (kip/in)
7.6	1.6	4.75

Analytical Model

Disp. (in)
1.515

Difference- Test and Model

%
5.3125

Changing Moment of Inertia incrementally

Inertia	% change	Disp @ (L/2)	% change
3.2292	-10	1.529	0.924
3.3189	-7.5	1.525	0.660
3.4086	-5	1.522	0.462
3.4983	-2.5	1.518	0.198
3.588	0	1.515	0.000
3.6777	2.5	1.512	-0.198
3.7674	5	1.508	-0.462
3.8571	7.5	1.505	-0.660
3.9468	10	1.502	-0.858

Changing Modulus incrementally

"E"	% change	Disp @ (L/2)	% change
24750	-10	1.529	0.924
25437.5	-7.5	1.525	0.660
26125	-5	1.522	0.462
26812.5	-2.5	1.518	0.198
27500	0	1.515	0.000
28187.5	2.5	1.512	-0.198
28875	5	1.508	-0.462
29562.5	7.5	1.505	-0.660
30250	10	1.502	-0.858

Changing Tension Force

Tension	% change	Disp @ (L/2)	% change
400.500	-10	1.667	10.033
411.625	-7.5	1.626	7.327
422.750	-5	1.588	4.818
433.875	-2.5	1.55	2.310
445	0	1.515	0.000
456.1250	2.5	1.481	-2.244
467.2500	5	1.449	-4.356
478.3750	7.5	1.418	-6.403
489.5000	10	1.389	-8.317

Specimen #2 (Grouted)

Orientation:

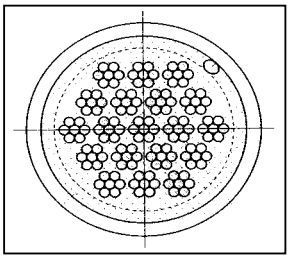

Overall specimen parameters

E (smear)	I (smear)	Length	Tension	Weight
27500 ksi	3.76 in^4	395.375 in	445 kips	.862 kips

Static Test Data

Load (kips)	Disp. (in)	Stiffness (kip/in)
7.6	1.6	4.75

Analytical Model

Disp. (in)
1.509

Difference- Test and Model

%
5.6875

Changing Moment of Inertia incrementally

Inertia	% change	Disp @ (L/2)	% change
3.384	-10	1.523	0.928
3.478	-7.5	1.519	0.663
3.572	-5	1.516	0.464
3.666	-2.5	1.512	0.199
3.76	0	1.509	0.000
3.854	2.5	1.505	-0.265
3.948	5	1.502	-0.464
4.042	7.5	1.499	-0.663
4.136	10	1.496	-0.861

Changing Modulus incrementally

"E"	% change	Disp @ (L/2)	% change
24750	-10	1.523	0.928
25437.5	-7.5	1.519	0.663
26125	-5	1.516	0.464
26812.5	-2.5	1.512	0.199
27500	0	1.509	0.000
28187.5	2.5	1.505	-0.265
28875	5	1.502	-0.464
29562.5	7.5	1.499	-0.663
30250	10	1.496	-0.861

Changing Tension Force

Tension	% change	Disp @ (L/2)	% change
400.500	-10	1.66	10.007
411.625	-7.5	1.619	7.290
422.750	-5	1.581	4.771
433.875	-2.5	1.544	2.319
445	0	1.509	0.000
456.1250	2.5	1.475	-2.253
467.2500	5	1.443	-4.374
478.3750	7.5	1.413	-6.362
489.5000	10	1.383	-8.350

Specimen #3 (Grouted)

Orientation:

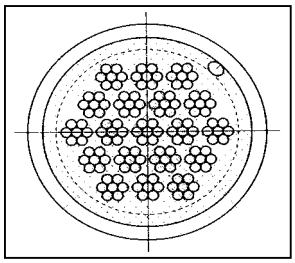

Overall specimen parameters

E (smear)	I (smear)	Length	Tension	Weight
27500 ksi	3.76 in^4	395.375 in	445 kips	.862 kips

Static Test Data

Load (kips)	Disp. (in)	Stiffness (kip/in)
7.496	1.6	4.685

Analytical Model

Disp. (in)
1.489

Difference- Test and Model

%
6.9375

Changing Moment of Inertia incrementally

Inertia	% change	Disp @ (L/2)	% change
3.384	-10	1.503	0.940
3.478	-7.5	1.5	0.739
3.572	-5	1.496	0.470
3.666	-2.5	1.493	0.269
3.76	0	1.489	0.000
3.854	2.5	1.486	-0.201
3.948	5	1.483	-0.403
4.042	7.5	1.479	-0.672
4.136	10	1.476	-0.873

Changing Modulus incrementally

"E"	% change	Disp @ (L/2)	% change
24750	-10	1.503	0.940
25437.5	-7.5	1.5	0.739
26125	-5	1.496	0.470
26812.5	-2.5	1.493	0.269
27500	0	1.489	0.000
28187.5	2.5	1.486	-0.201
28875	5	1.483	-0.403
29562.5	7.5	1.479	-0.672
30250	10	1.476	-0.873

Changing Tension Force

Tension	% change	Disp @ (L/2)	% change
400.500	-10	1.638	9.933
411.625	-7.5	1.598	7.248
422.750	-5	1.56	4.698
433.875	-2.5	1.524	2.282
445	0	1.49	0.000
456.1250	2.5	1.456	-2.282
467.2500	5	1.425	-4.362
478.3750	7.5	1.394	-6.443
489.5000	10	1.365	-8.389

Specimen #4 (Grouted)

Orientation:

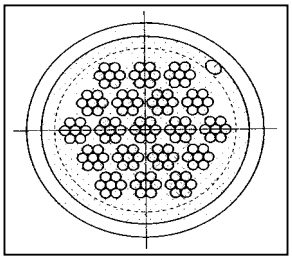

Overall specimen parameters

E (smear)	I (smear)	Length	Tension	Weight
27500 ksi	3.76 in^4	395.375 in	445 kips	.862 kips

Static Test Data

Load (kips)	Disp. (in)	Stiffness (kip/in)
4.9885	1.1	4.535

Analytical Model

Disp. (in)
1.018

Difference- Test and Model

%
7.4545455

Changing Moment of Inertia incrementally

Inertia	% change	Disp @ (L/2)	% change
3.384	-10	1.028	0.982
3.478	-7.5	1.025	0.688
3.572	-5	1.023	0.491
3.666	-2.5	1.02	0.196
3.76	0	1.018	0.000
3.854	2.5	1.016	-0.196
3.948	5	1.014	-0.393
4.042	7.5	1.011	-0.688
4.136	10	1.009	-0.884

Changing Modulus incrementally

"E"	% change	Disp @ (L/2)	% change
24750	-10	1.028	0.982
25437.5	-7.5	1.025	0.688
26125	-5	1.023	0.491
26812.5	-2.5	1.02	0.196
27500	0	1.018	0.000
28187.5	2.5	1.016	-0.196
28875	5	1.014	-0.393
29562.5	7.5	1.011	-0.688
30250	10	1.009	-0.884

Changing Tension Force

Tension	% change	Disp @ (L/2)	% change
400.500	-10	1.12	10.020
411.625	-7.5	1.093	7.367
422.750	-5	1.067	4.813
433.875	-2.5	1.042	2.358
445	0	1.018	0.000
456.1250	2.5	0.996	-2.161
467.2500	5	0.974	-4.322
478.3750	7.5	0.953	-6.385
489.5000	10	0.933	-8.350

Specimen #6 (Grouted)

Orientation:

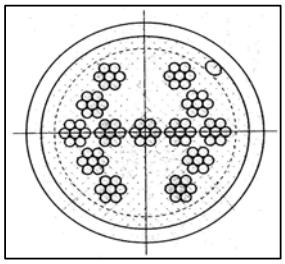

Overall specimen parameters

E (smear)	I (smear)	Length	Tension	Weight
27500 ksi	1.62 in^4	395.375 in	304.47 kips	.772 kips

Static Test Data

Load (kips)	Disp. (in)	Stiffness (kip/in)
5.24	1.6	3.275

Analytical Model

Disp. (in)
1.603

Difference- Test and Model

%
0.1875

Changing Moment of Inertia incrementally

Inertia	% change	Disp @ (L/2)	% change
1.458	-10	1.614	0.686
1.4985	-7.5	1.611	0.505
1.539	-5	1.608	0.324
1.5795	-2.5	1.605	0.143
1.62	0	1.603	0.000
1.6605	2.5	1.600	-0.183
1.701	5	1.597	-0.366
1.7415	7.5	1.594	-0.548
1.782	10	1.591	-0.730

Changing Modulus incrementally

"E"	% change	Disp @ (L/2)	% change
24750	-10	1.614	0.686
25437.5	-7.5	1.611	0.505
26125	-5	1.608	0.324
26812.5	-2.5	1.605	0.143
27500	0	1.603	0.000
28187.5	2.5	1.600	-0.183
28875	5	1.597	-0.366
29562.5	7.5	1.594	-0.548
30250	10	1.591	-0.730

Changing Tension Force

Tension	% change	Disp @ (L/2)	% change
274.023	-10	1.761	9.857
281.635	-7.5	1.723	7.486
289.247	-5	1.681	4.866
296.858	-2.5	1.641	2.371
304.47	0	1.603	0.000
312.0818	2.5	1.567	-2.246
319.6935	5	1.532	-4.429
327.3053	7.5	1.498	-6.550
334.9170	10	1.467	-8.484

Specimen #7 (Grouted)

Orientation:

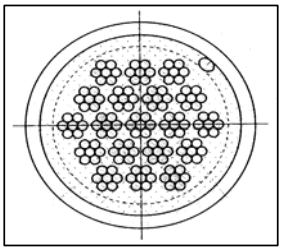

Overall specimen parameters

E (smear)	I (smear)	Length	Tension	Weight
27500 ksi	3.76 in^4	395.375 in	445 kips	.870 kips

Static Test Data

Load (kips)	Disp. (in)	Stiffness (kip/in)
7.96	1.6	4.972

Analytical Model

Disp. (in)
1.577

Difference- Test and Model

%
1.4375

Changing Moment of Inertia incrementally

Inertia	% change	Disp @ (L/2)	% change
3.384	-10	1.592	0.951
3.478	-7.5	1.588	0.698
3.572	-5	1.584	0.444
3.666	-2.5	1.581	0.254
3.76	0	1.577	0.000
3.854	2.5	1.574	-0.190
3.948	5	1.57	-0.444
4.042	7.5	1.567	-0.634
4.136	10	1.563	-0.888

Changing Modulus incrementally

"E"	% change	Disp @ (L/2)	% change
24750	-10	1.592	0.951
25437.5	-7.5	1.588	0.698
26125	-5	1.584	0.444
26812.5	-2.5	1.581	0.254
27500	0	1.577	0.000
28187.5	2.5	1.574	-0.190
28875	5	1.57	-0.444
29562.5	7.5	1.567	-0.634
30250	10	1.563	-0.888

Changing Tension Force

Tension	% change	Disp @ (L/2)	% change
400.500	-10	1.735	10.019
411.625	-7.5	1.693	7.356
422.750	-5	1.652	4.756
433.875	-2.5	1.614	2.346
445	0	1.577	0.000
456.1250	2.5	1.542	-2.219
467.2500	5	1.509	-4.312
478.3750	7.5	1.477	-6.341
489.5000	10	1.446	-8.307

Specimen #9 (Grouted)

Orientation:

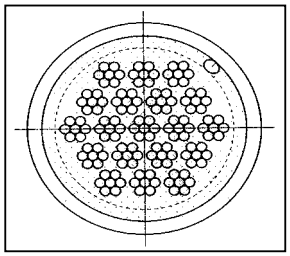

Overall specimen parameters

E (smear)	I (smear)	Length	Tension	Weight
27500 ksi	3.76 in^4	395.375 in	445 kips	.870 kips

Static Test Data

Load (kips)	Disp. (in)	Stiffness (kip/in)
7.2	1.6	4.5

Analytical Model

Disp. (in)
1.434

Difference- Test and Model

%
10.375

Changing Moment of Inertia incrementally

Inertia	% change	Disp @ (L/2)	% change
3.384	-10	1.448	0.976
3.478	-7.5	1.444	0.697
3.572	-5	1.441	0.488
3.666	-2.5	1.438	0.279
3.76	0	1.434	0.000
3.854	2.5	1.431	-0.209
3.948	5	1.428	-0.418
4.042	7.5	1.425	-0.628
4.136	10	1.422	-0.837

Changing Modulus incrementally

"E"	% change	Disp @ (L/2)	% change
24750	-10	1.448	0.976
25437.5	-7.5	1.444	0.697
26125	-5	1.441	0.488
26812.5	-2.5	1.438	0.279
27500	0	1.434	0.000
28187.5	2.5	1.431	-0.209
28875	5	1.428	-0.418
29562.5	7.5	1.425	-0.628
30250	10	1.422	-0.837

Changing Tension Force

Tension	% change	Disp @ (L/2)	% change
400.500	-10	1.578	10.042
411.625	-7.5	1.539	7.322
422.750	-5	1.503	4.812
433.875	-2.5	1.468	2.371
445	0	1.434	0.000
456.1250	2.5	1.403	-2.162
467.2500	5	1.372	-4.324
478.3750	7.5	1.343	-6.346
489.5000	10	1.315	-8.298

Specimen #10 (Grouted)

Orientation:

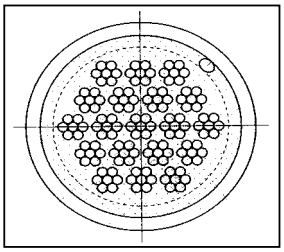

Overall specimen parameters

E (smear)	I (smear)	Length	Tension	Weight
27500 ksi	3.76 in^4	395.375 in	445 kips	.870 kips

Static Test Data

Load (kips)	Disp. (in)	Stiffness (kip/in)
5.28	1.1	4.8

Analytical Model

Disp. (in)
1.074

Difference- Test and Model

%
2.36

Changing Moment of Inertia incrementally

Inertia	% change	Disp @ (L/2)	% change
3.384	-10	1.084	0.931
3.478	-7.5	1.081	0.652
3.572	-5	1.079	0.466
3.666	-2.5	1.076	0.186
3.76	0	1.074	0.000
3.854	2.5	1.071	-0.279
3.948	5	1.069	-0.466
4.042	7.5	1.066	-0.745
4.136	10	1.064	-0.931

Changing Modulus incrementally

"E"	% change	Disp @ (L/2)	% change
24750	-10	1.084	0.931
25437.5	-7.5	1.081	0.652
26125	-5	1.079	0.466
26812.5	-2.5	1.076	0.186
27500	0	1.074	0.000
28187.5	2.5	1.071	-0.279
28875	5	1.069	-0.466
29562.5	7.5	1.066	-0.745
30250	10	1.064	-0.931

Changing Tension Force

Tension	% change	Disp @ (L/2)	% change
400.500	-10	1.181	9.963
411.625	-7.5	1.152	7.263
422.750	-5	1.125	4.749
433.875	-2.5	1.099	2.328
445	0	1.074	0.000
456.1250	2.5	1.05	-2.235
467.2500	5	1.027	-4.376
478.3750	7.5	1.005	-6.425
489.5000	10	0.9843	-8.352

As can be clearly seen in the previous pages, variations in the Young's modulus and/or in the (equivalent) section moment of inertia do not result in substantial variation. For example, for specimen #7 a ±10% change in either the modulus or the moment of inertia resulted in less than 1% of change in the midspan deflection. By contrast, the sensitivity to variations of the tension load is significant: for the same specimen #7 a 5% change in the tension force results in a 4.76% change in the midspan deflection. In fact, the variation is nearly linear. We then attribute the observed differences to uncertainties in the actual magnitude of the applied tension force.

One other possible source of discrepancy lies in the Young's modulus for the grout. A value of 3500 ksi was used which is consistent with previous work (Poser, 2001). This value used is approximate, and as such we might be concerned that its uncertainty would lead to discrepancies in the solution obtained. An altering of the grout's modulus would change the modular ratio used to determine the transformed moment of inertia used in the solution. However, it can be shown that discrepancy in the modulus for the grout lead to only small changes in the overall solution. For example, looking at the results for specimen #1; if we were to change the grout Young's modulus by 20%, the transformed moment of inertia would be changed by roughly 6.7%. If we look at the data for specimen #1 in the previous pages we can see that a change in the moment of inertia of even 10% does not result in even a 1% change in the overall solution.

4.2.2.1 Bending stresses in grouted specimens

The bending stresses of the grouted specimens were computed based on the same Euler-Bernoulli model; details are provided in Appendix B.

It should be noted that in developing the equations for a load-displacement relationship of the grouted specimens, we used the second moment of inertia

corresponding to sections along the free-length of the specimens. By "free-length", we refer to the majority of the specimen's length where the cross-section of the specimen was uniform and at its smallest. As the drawings shown earlier in this chapter would indicate (Figure 4.6), the transition region as well as the cross-section directly at the anchorage have larger cross-sectional areas and the steel strands splay out in order to have enough area around the ends of the strands for prestressing purposes. For example, the following pictures show a comparison of the dimensions of the cross-sections at the anchorage as well as along the free-length for the first specimen.

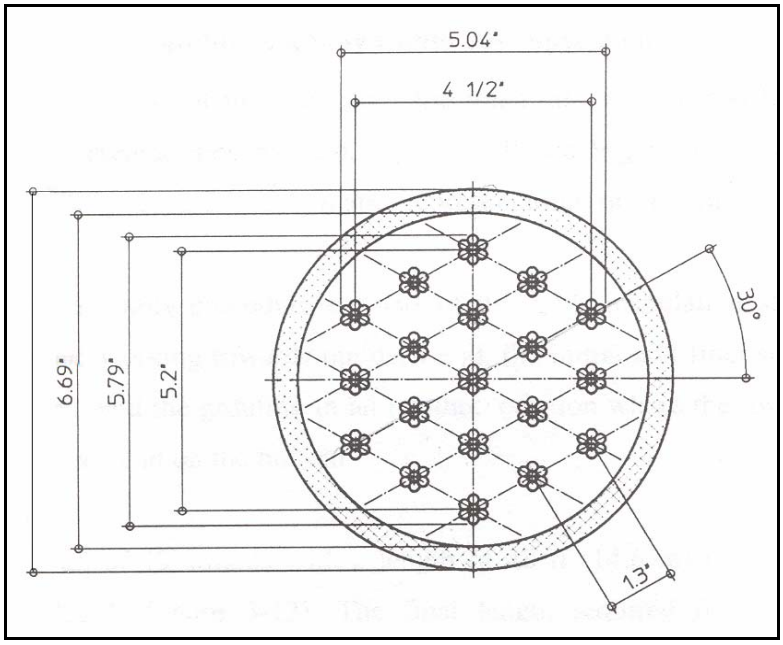

Figure 4.8 Cross-section at the anchor head

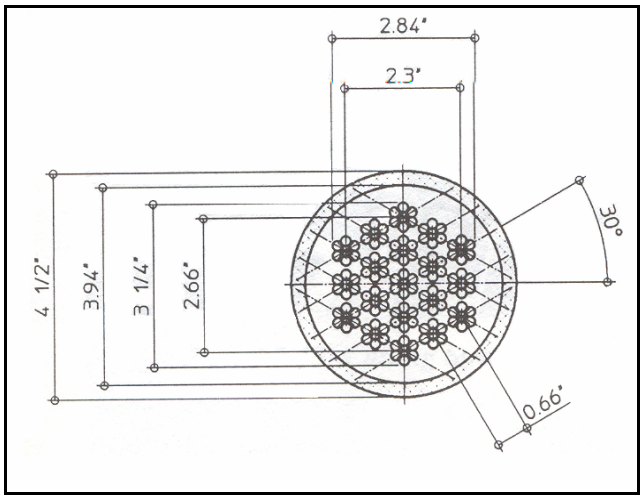

Figure 4.9 Cross-section along the free-length

The moment of inertia at the anchor head, as calculated in Appendix A is approximately 4 ½ times that of the free length moment of inertia. We might conclude that a better approximation for moment of inertia might be to average the moment of inertia along the length, but as was shown in section 4.2.2 altering the moment of inertia did not have a significant effect on the solution obtained for the displacements. While this may be the case for determining the overall load-displacement relationship, it is important to recognize that any attempt made to calculate the bending stresses at the anchor heads should be made with the appropriate moment of inertia of that section.

The smeared moments of inertia at the anchor head are calculated in Appendix A for use in estimating bending stresses in the grouted test specimens. In order to calculate the bending stresses in the steel we must make some assumptions about the condition of the grout at the anchor heads: as reported by (Poser 2001) and (Ridd 2004) there were typically a few cracks and even evidence of some crushing in the grout at the anchorages in nearly all the specimens observed in the autopsies performed after the testing was completed.

This would seem to indicate that some reduction in the cross-sections smeared moment of inertia should be used in calculating bending stresses. An exact value for the moment of inertia corresponding to the cracked grout section will never be known for these tests, as such bending stresses are calculate with moments of inertia for the two extreme cases of; no cracking in the grout, and conversely, complete deterioration of the grout. In the latter case, the moment of inertia is just from the steel. With this in mind, the bending stresses were calculated (see Appendix B).

Table 4.7 Closed-form bending stresses at the terminations

Bending Stress Ranges at the Anchorages				
Specimen	**Displacement**	**Load**	**Uncracked Bending Stress Range**	**No Grout; Bending Stress Range**
	(in)	(kips)	± (ksi)	± (ksi)
1	1.60	7.60	8.64	19.7
2	1.60	7.60	7.74	17.6
3	1.60	7.50	7.64	17.4
4	1.10	4.99	5.33	12.2
6	1.60	5.24	6.82	21.3
7	1.60	7.96	8.07	18.4
9	1.60	7.20	7.37	16.8
10	1.10	5.28	5.61	12.8

While the aim of the experimental tests was to match bending stresses from Cable #24 in the anchorage regions it might be worthwhile to calculate the bending stresses at midspan using the same procedure used for the anchorages. These values should only be used to explain possible breaks occurring in this region during testing and not used to correlate bending stresses with those at the anchorages of the actual bridge cables.

Table 4.8 Closed-form bending stresses at mid-span

Bending Stress Ranges at Mid-Span				
Specimen	Displacement	Load	Uncracked Bending Stress Range	No Grout; Bending Stress Range
	(in)	(kips)	± (ksi)	± (ksi)
1	1.60	7.60	20.9	31.3
2	1.60	7.60	18.7	27.3
3	1.60	7.50	18.5	26.9
4	1.10	4.99	12.4	18.0
6	1.60	5.24	18.0	32.4
7	1.60	7.96	19.6	28.6
9	1.60	7.20	17.7	25.9
10	1.10	5.28	13.1	19.0

4.2.2.2 Comparison of field and laboratory bending stresses

The intent of the laboratory experiments was to subject the terminations of the specimens' steel strands to the same stress range as the estimated stress range the actual stay-cables were estimated to have undergone, as a necessary precursor to estimating the fatigue life of the stay-cables. Table 4.9 below summarizes the stress range as computed for the laboratory specimens (assuming no grout contribution for the moment of inertia) at the anchorages and compares these values against the finite element stress range reported in the previous chapter. In general, we can see that the laboratory specimens total cyclic bending stress range is significantly lower than the value of ± 27.17 ksi determined from the dynamic modeling of Chapter 3.

Table 4.9 Comparison of bending stress ranges at the terminations

Bending Stress Calculations			
Specimen	Calculated Laboratory Stress Range (No Grout)	Calculated Stress Range for Cable #24	Difference
	± (ksi)	± (ksi)	%
1	19.7	27.2	-27.4
2	17.8	-	-34.5
3	20.1	-	-26.0
4	14.0	-	-48.5
6	24.2	-	-10.9
7	21.2	-	-22.0
9	19.4	-	-28.6
10	14.7	-	-45.9

As it can be seen from Table 4.9 there are differences between the computed bending stress range for the laboratory specimens obtained through the Euler-Bernoulli model, and the bending stress range computed from the model of the field stay-cable using the finite element transient analysis. There are several reasons for the discrepancy: a) the loading or excitation is considerably different (a midspan point load for the laboratory specimens versus a moving support load for the field cable). The discrepancy can be further attributed to earlier finite element analyses (Dowd 2001) that were used to calibrate the laboratory setup, which, in turn, were based on estimates of the observed field motion that have been revised here. b) Though it can be argued that once similar stress ranges to the field cable are achieved in the laboratory, conclusions regarding the fatigue life could extend to the field cable, it is important to observe that there is a considerable behavioral difference between the laboratory specimen and the actual stay-cable: this can be best seen from the fact that the γ parameter that describes beam versus cable behavior is typically 26 for the laboratory specimen versus 292 for the field cable. The importance and the role the γ parameter plays

is discussed in the next chapter, where modifications to the test setup are suggested for future testing in an effort to better capture the field cable's behavior.

4.2.3 Modeling of ungrouted specimens

Because of the small moments of inertia for specimens #5 and #8 (both ungrouted) it is more appropriate to obtain a solution for displacements by treating these specimens solely as a group of cables instead of using the Euler-Bernoulli theory. To this end, the following equation describes the load-midspan-deflection response (see Appendix B for the derivation details) of a single cable under a concentrated load applied at midspan.

$$P = \left(\frac{4 \cdot T \cdot w}{L} \right) + \left(8 \cdot \frac{E \cdot A - T}{3 \cdot L^3} \right) \cdot w^3 \tag{4.4}$$

where w denotes here the midspan deflection. The second, higher-order, term in the equation contributes a negligible amount (see Appendix B), and if ignored allows us to solve explicitly for the midspan deflection in terms of the applied load as:

$$w = \frac{P \cdot L}{4 \cdot T} \tag{4.5}$$

Furthermore, the midspan deflection due to self-weight can be calculated as:

$$w_{sag} = \frac{mg \cdot L^2}{8 \cdot T} \tag{4.6}$$

where w_{sag} is the displacement at midspan. The total deflection can be obtained via superposition of equations 4.5 and 4.6. Using the resulting expression and the given properties of the ungrouted specimens the corresponding values of displacement are obtained and compared with the experimental values in the table

below. It should be noted here again that in the actual laboratory tests the neutral testing position was taken with sagging included.

Table 4.10 Comparison of static midspan deflections for ungrouted specimens

Displacements				
Stay	**Load**	**Actual**	**Analytical**	**Comparison**
	(kips)	(in)	(in)	%
5	6.53	1.6	1.5	6.25
8	6.56	1.6	1.51	5.63

In Table 4.10 we can see that the solutions provided by the cable analysis are within a similar error range as the grouted specimens modeled with the Euler-Bernoulli beam equation; these results are equally sensitive to variations of the tension force as the ones presented earlier for the grouted specimens. However, the above simplified formulae have been derived for a single cable and have been applied to a group of cables, thereby not taking into account any geometric variations that were indeed present in the laboratory specimens. Thus, to better account for the actual cable arrangement in the laboratory, we used a finite element model to obtain the midspan deflection. This is described in the next section.

4.2.3.1 Finite element analysis of ungrouted specimens

The solid modeling of the ungrouted specimens consisted solely of the steel strands. The gradual change in the overall cross-section in the transition region between the anchor head and tension ring is now taken into account and can be seen in the oblique, close-up image of Figure 4.10.

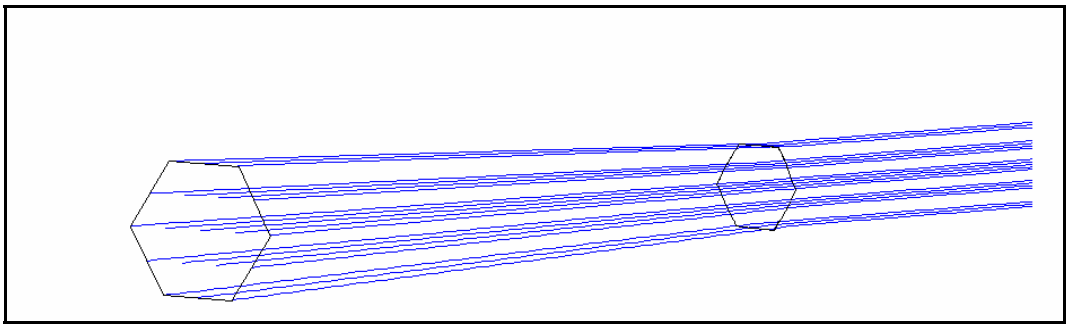

Figure 4.10 Transition region of strand arrangement

The material properties used by ANSYS were the same as those used in the closed-form solution. The Young's modulus was 27500 ksi and a Poisson's ratio of 0.33 was used. In order to best model the cable behavior of the ungrouted steel strands LINK8 elements were used. LINK8 elements possess 3 degrees of freedom (X,Y,Z), provide no flexural resistance, and can only resist axial loads in tension. In addition to these basic operations LINK8 elements are capable of having an initial strain input by the user. This initial strain is input, along with a standard cross-sectional area for each element, via the real constants for the element type. The tension force, given by (Ridd 2004), is taken to be 445 kips for the whole cross-section and the cross-sectional area is taken as the nominal area of 0.217 in^2. With these numbers a value of initial strain could be found for use with the elements to simulate the applied tension force, as per:

$$\varepsilon = \sigma \cdot E = \frac{T}{A} \cdot E \qquad 4.7$$

The strain value and cross-sectional area corresponding to this equation are input into ANSYS as seen in Figure 4.11.

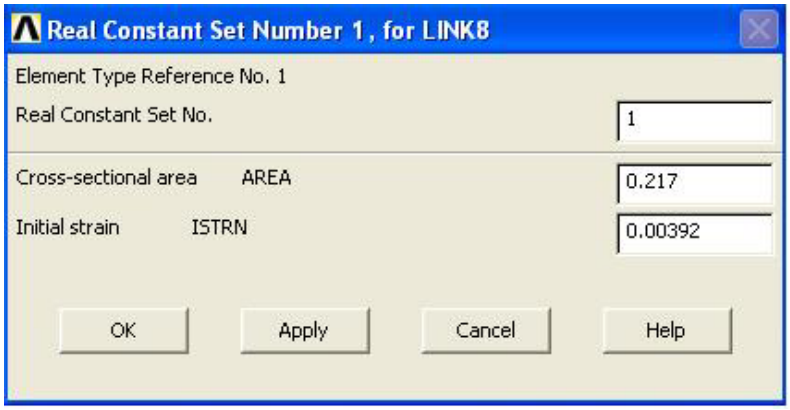

Figure 4.11 Real constants for Link 8 elements

Each strand was modeled with elements averaging just under 0.5" in length along its entire span.

In order to make sure the FEA model was representative of the experimental setup the nature of the applied loads and boundary conditions is of great importance. The terminations of the strands at the anchor heads are modeled in ANSYS as having displacement constraints in the X, Y, and Z directions. An image of these applied boundary conditions at the anchor heads is seen below.

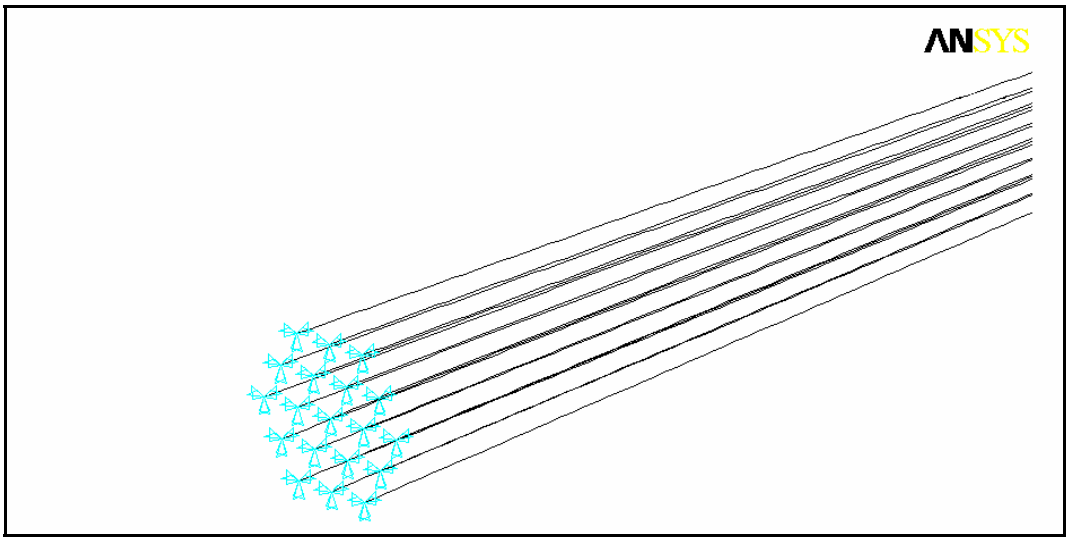

Figure 4.12 Boundary conditions at anchor head

In addition to the constraints at the anchor heads it was necessary that constraints in the form of boundary conditions and coupling equations were applied to the nodes corresponding to the tension ring location as well as the mid-point where the actuator load is applied. The strands of the ungrouted specimens were held tightly together at the tension rings restricting any relative motion between the strands in the Y or, vertical, directions. In addition to this vertical restraint, motion was restrained in the X-direction (which in this model is perpendicular to the length of the strands. In order to replicate the vertical behavior at the tension ring cross-section it is important to recognize that vertical displacements do in fact occur there, there is just no relative vertical displacement between the strands. This vertical behavior was modeled with coupling equations that prevent any relative vertical displacement between the nodes. These described constraints for the tension ring can be seen in Figure 4.13.

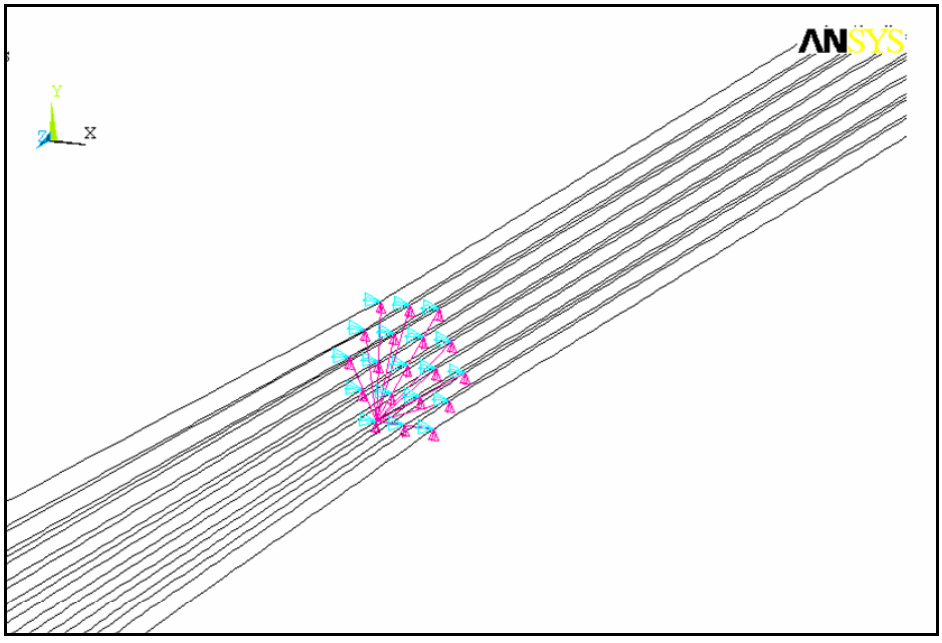

Figure 4.13 Tension ring constraints

In addition to the coupling equations at the tension ring, there must also be a similar vertical coupling applied to the nodes at the mid-span cross-section where the vertical load is applied in order to prevent any relative vertical motion between the strands. Geometry, solid modeling, element types, and boundary conditions were the same for both of the ANSYS models for specimens #5 and #8. The only difference between the 2 models was the magnitude of the load applied. Specimen #5 had a load of 6.53 kips and specimen #8 had a load of 6.56 kips (Ridd 2004). For both cases however, the load was distributed in ANSYS among the 19 strands equally at their center nodes. The following isometric image shows the application of the static load and the coupling equations as described for the center of the span.

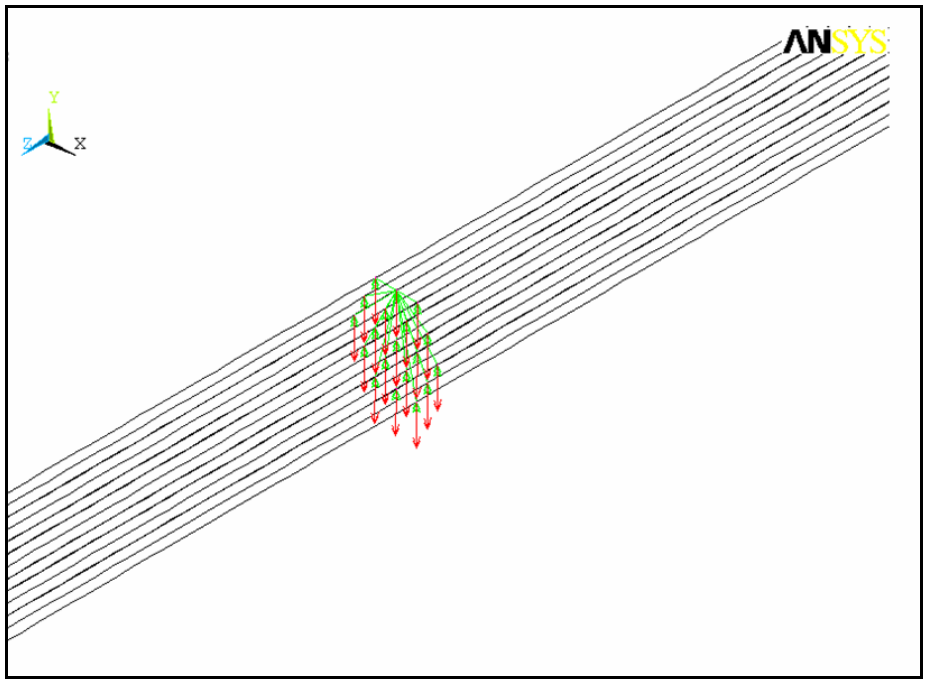

Figure 4.14 Mid-span loading and constraints

Figure 4.15 provides a better idea of what the entire ANSYS model looks like. It is an isometric view of the entire specimen with boundary conditions, load, and constraint equations all visible.

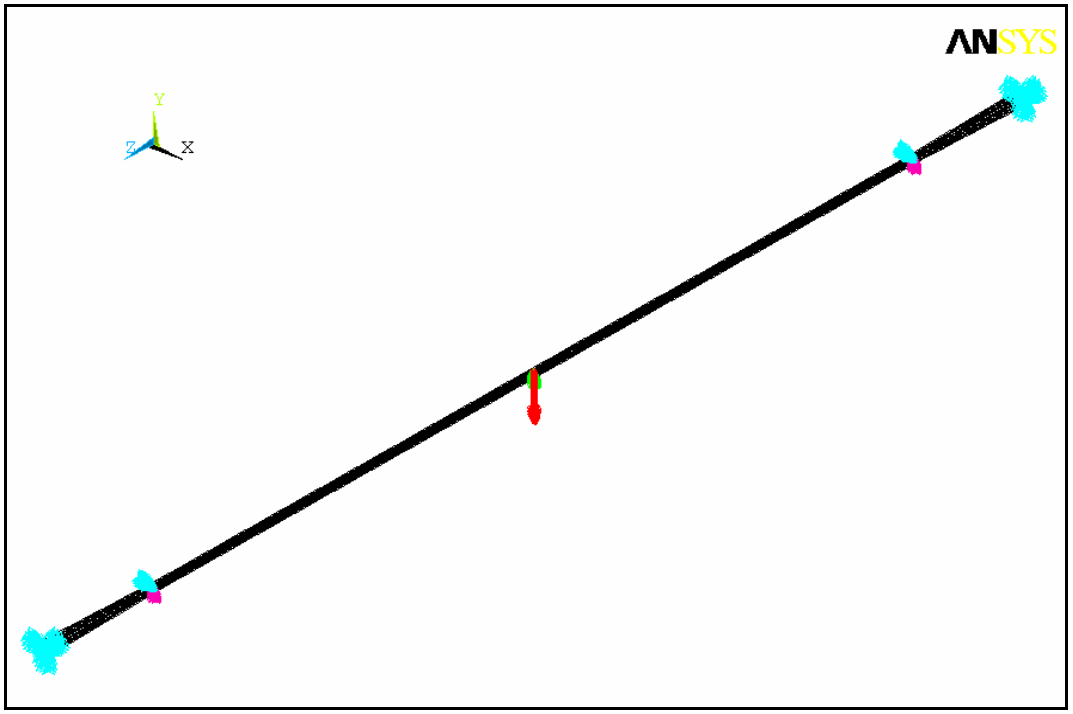

Figure 4.15 Entire specimen with boundary conditions and loads

Displaced shapes are scaled 15 times and shown in the following images, Figure 4.16 and Figure 4.17 for the whole ANSYS model as well as a close-up of the transition regions.

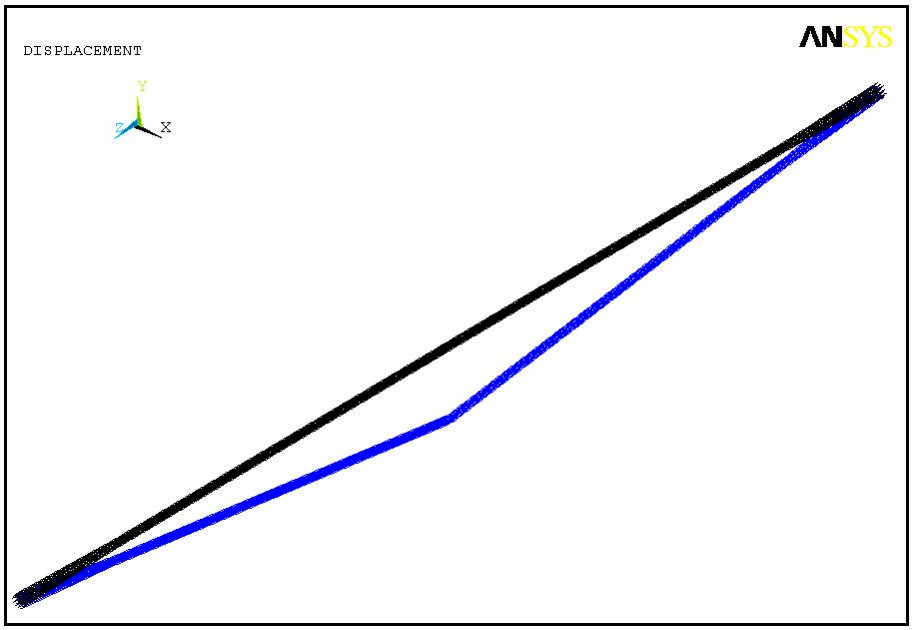

Figure 4.16 Displaced shape of cable: full isometric view

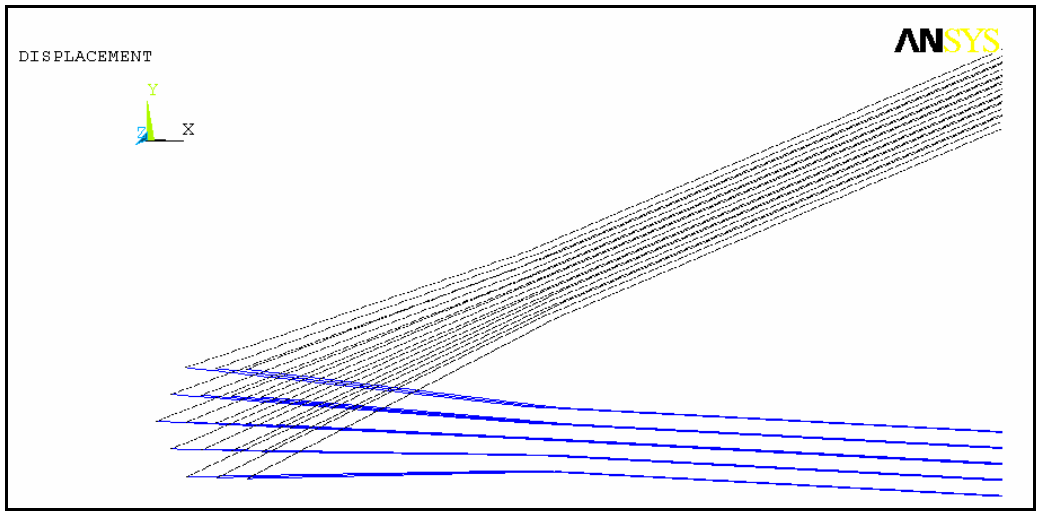

Figure 4.17 Displaced shape of cable: oblique anchorage close-up

The results obtained for displacement from ANSYS are shown in Table 4.11 below along with the closed-form solutions and the experimental results.

Table 4.11 ANSYS cable-model results

Displacements			
Stay	**Analytical (in)**	**ANSYS (in)**	**Actual (in)**
5	1.5	1.48	1.6
8	1.51	1.49	1.6

As it can be seen the finite element results, now accounting for the correct laboratory specimen geometry, very closely match the ones obtained from expressions 4.5 and 4.6, and exhibit the same difference from the actual values obtained from the experiment. Again, the difference is attributed to the uncertainty about the actual value of the applied tension force.

CHAPTER 5
New Testing Guidelines

5.1 OBJECTIVE

The primary objective of this chapter is to develop the test parameters for a new series of bending fatigue tests aimed at overcoming the limitations of past experiments while being more representative of the field behavior. The primary parameters investigated are the cable/beam parameter, $\gamma = \sqrt{\frac{TL^2}{EI}}$, as well as the bending stress range computed in Chapter 3 for Cable #24 of the Fred Hartman Bridge. To this end, we discuss first the fundamental differences between cable and beam model behavior.

5.2 BEAM-CABLE: CHARACTERISTIC BEHAVIOR

An ideal cable has no flexural rigidity present; it is capable of carrying only tensile axial forces and no bending stresses along its length. In design practice the terminations of cables on bridges are typically modeled as pin-connections with no flexural rigidity for simplicity's sake and because, on the whole, it is a reasonable assumption (Gimsing 1998).

In reality, however, cables do exhibit some minimal flexural rigidity. Along the overall length of the member the presence of this relatively small amount of stiffness causes bending stresses of negligible magnitude as there are no significant changes in the curvatures of the cables. While in these cases it is the tensile stresses across the cross-section that are of primary design importance, there are cases where the effects of flexural rigidity should not be ignored. Under

large-amplitude dynamic motion, termination or clamping regions could become areas of significant bending stress-induced fatigue for a stay-cable. This suggests that to better characterize a cable's stress distribution due to dynamic behavior it is necessary to include the effects of flexural rigidity at least at those locations where large curvatures are expected.

5.2.1 The importance of the γ-parameter

Before we can begin to understand the possible dynamic effects of bending fatigue on stay-cables we should first look at the equations governing their static behavior. The differential equation for an elastic beam (Euler-Bernoulli assumptions) supporting both a tension force and a lateral, distributed load is given as:

$$EI\frac{d^4w(x)}{dx^4} - T\frac{d^2w(x)}{dx^2} = q(x) \qquad 5.1$$

Notice that as the flexural rigidity term EI approaches zero we recover the familiar governing differential equation for a taut string or "cable" under uniform lateral load and a tension force (also valid for a cable with a sag to span ratio of 1:8 or less).

$$-T\frac{d^2w(x)}{dx^2} = q(x) \qquad 5.2$$

An interesting question is thus, "What happens in the transition region of diminishing flexural rigidity, where the structural member is neither beam under tension nor a string." Kervorkian (et al 1981) suggest that as we move away from the traditional beam model with diminishing flexural rigidity the loss of the necessary boundary condition (5.1 needs four boundary conditions compared to only two for 5.2) implies the existence of a boundary layer near the support, a region where the effects of flexural rigidity cannot be ignored. This is an idea

synonymous to boundary layer behavior in fluid dynamics (Irvine, 1981). In parallel, it is also of interest to be able to define the cutoff value (if any) for the above transition zone. To illustrate, let us consider a fixed-fixed beam of length L, flexural rigidity EI, under a uniform load q, and subjected to a tension force T. It is easy to show that the exact solution is given as:

$$\hat{w}(\hat{x}) = \frac{1}{2}\left[-\hat{x}^2 + \hat{x} + \frac{1}{\gamma}\frac{\sinh(\gamma)}{\cosh(\gamma)-1}\left(\cosh\left(\gamma\hat{x}\right)-1\right) - \frac{1}{\gamma}\sinh\left(\gamma\hat{x}\right)\right] \qquad 5.3$$

where the following normalized quantities have been used:

$$\hat{x} = \frac{x}{L}, \hat{w} = \frac{w}{\left(\frac{qL^2}{T}\right)} \qquad 5.4$$

Furthermore, the normalized bending moment can be easily shown to be:

$$\hat{M}(\hat{x};\gamma) = \frac{1}{2\gamma^2}\left[2 - \gamma\left(\frac{\cosh\left(\gamma\hat{x}\right)}{\tanh\left(\frac{\gamma}{2}\right)} - \sinh\left(\gamma\hat{x}\right)\right)\right] \qquad 5.5$$

where $\hat{M}(\hat{x};\gamma) = \frac{M}{qL^2}$, with M denoting bending moment.

We first consider the two extreme cases for the governing behavior of the structural member. In the first case, we may assume that γ is extremely low, almost zero, and thus we have beam behavior governing. As such, a bending moment would have to exist at the mid-span of the member; in fact, it can be readily verified from equation 5.5 that $\hat{M}(0.5;0) = \frac{1}{24}$. On the other hand, when γ is much higher, and flexural rigidity is negligible, cable behavior must govern and therefore there should be negligible moment in the member at the mid-span, or anywhere else along the length for that matter (for example, $\hat{M}(0.5;\infty) = 0$).

The following graph provides a better understanding of when the mid-span moment approaches zero, implying cable-like behavior.

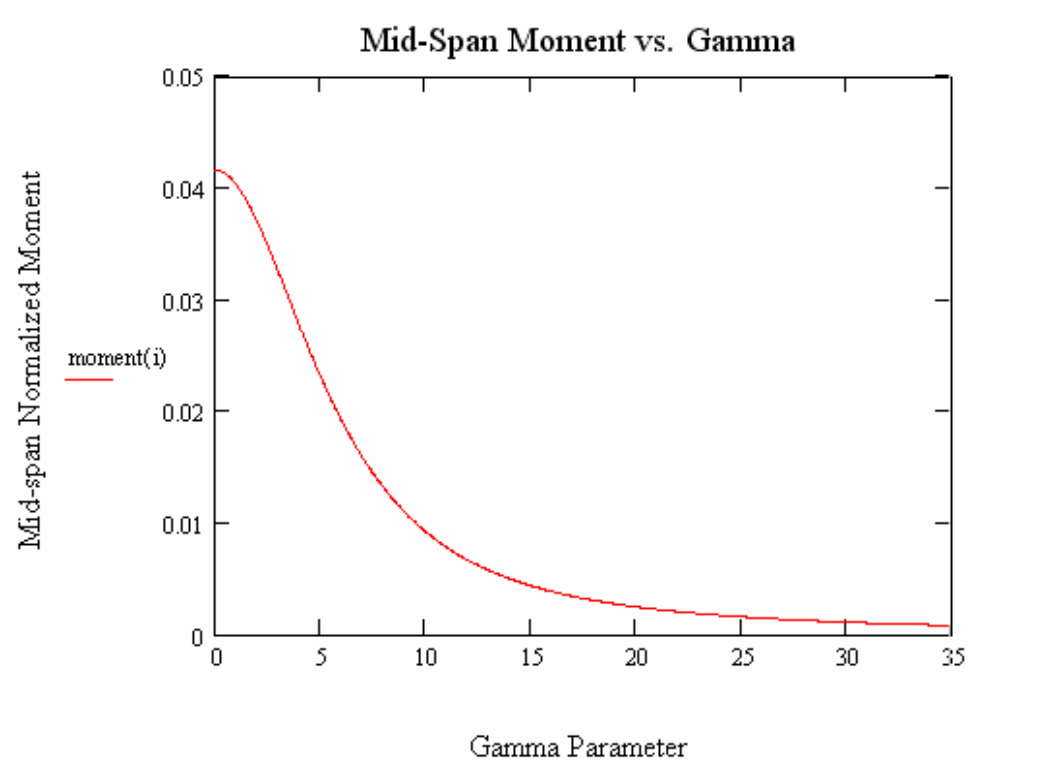

Figure 5.1 Mid-span moment versus γ

As can be seen in the figure above, as γ increases the corresponding mid-span moment decreases exponentially, confirming the conclusion that with increasing γ we see a drastic reduction in any mid-span moment, indicative of cable characteristics. Obviously mid-span moment doesn't ever truly reach zero until γ reaches ∞, which would imply a member with no flexural rigidity whatsoever. For practical purposes however, it would be helpful to find a cutoff value indicative of dominant cable behavior. One plausible value for a cutoff is to set the mid-span moment to less than or equal to 1% of that of a pure beam model.

With that value in mind we can find a value of γ that corresponds to this cutoff value for mid-span moment from the equations previously used.

$$\frac{\hat{M}(0.5;\gamma_{\text{cutoff}})}{\hat{M}(0.5;0)} = 0.01 \text{ where } \hat{M}(0.5;0) = 0.04167$$

We thus seek solutions for γ_{cutoff} such that:

$$\hat{M}(\hat{x} = 0.5;\gamma_{\text{cutoff}}) = 0.0004167 = \frac{1}{2\gamma_{\text{cutoff}}^2}\left[2 - \gamma_{\text{cutoff}}\left(\frac{\cosh(\gamma_{\text{cutoff}} \cdot 0.5)}{\tanh\left(\frac{\gamma_{\text{cutoff}}}{2}\right)} - \sinh(\gamma_{\text{cutoff}} \cdot 0.5)\right)\right]$$

Solving for γ_{cutoff} we obtain the value which corresponds to the minimum value necessary for cable behavior, per the above criterion.

$$\gamma_{\text{cutoff}} = 49$$

5.2.2 Effects of γ on stress distribution

It is worthwhile to investigate the effects that γ has on the distribution of stresses along our hypothetical structural "member" with an eye on fatigue life. As demonstrated earlier altering γ has a significant effect on the level of bending stresses at terminations of structural members. While it has already been discussed that changing γ can determine whether bending stresses are seen along the length of the member, the rate of change of these bending stresses away from the supports also depends on γ.

In order to assess the effect that varying γ has on the rate of change of bending stress or moment gradient in the member we can again return to the same example of the previous section. Figure 5.2 below depicts the distribution of

bending moments along the length of the example beam/cable for values of γ equal to 5, 25, and 250.

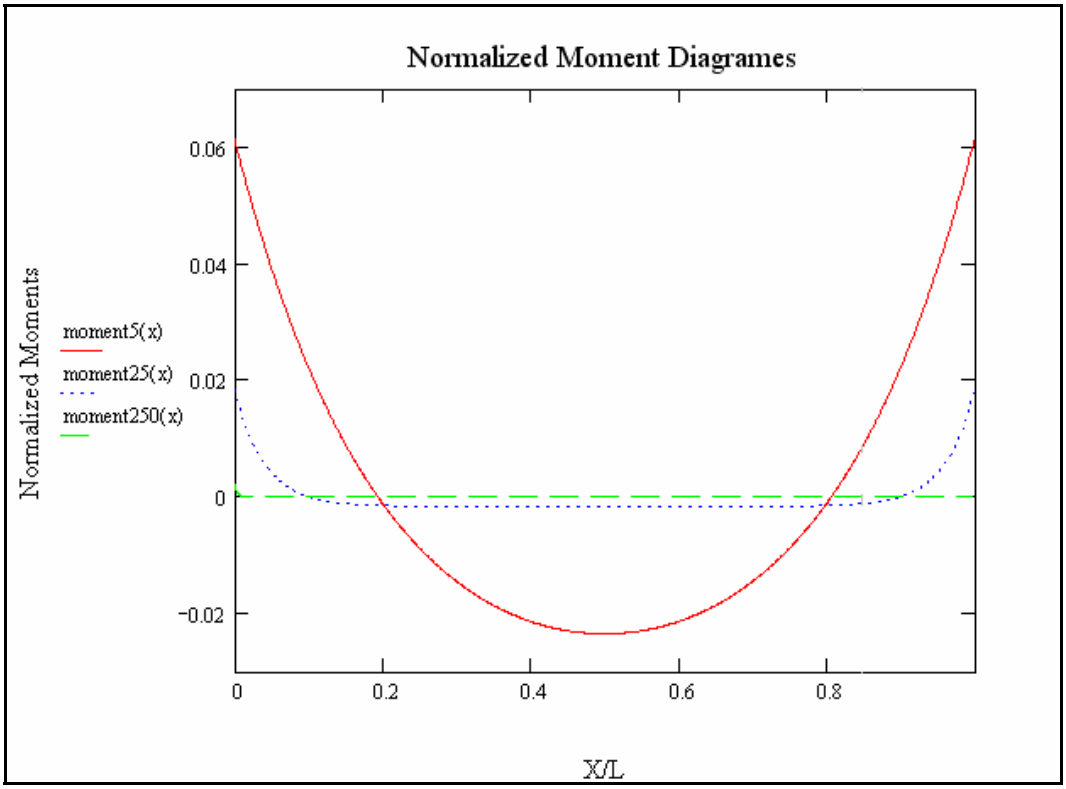

Figure 5.2 Effects of γ on moment distribution

It is apparent that as γ increases the overall element bending moments at the end decrease. It would also appear that the gradient gets steeper as γ increases. To investigate this effect on moment gradient further, the equation for the highest γ equal to 250, is scaled so that its peak bending moment at the left end is equal to the bending moment for γ equal to 25. This will allow us to see how two different structural members with the same peak values of moments at their terminations will differ in their moment gradients. See the following figure, which is a close-up plot of $\hat{x}$ from 0 to 0.1.

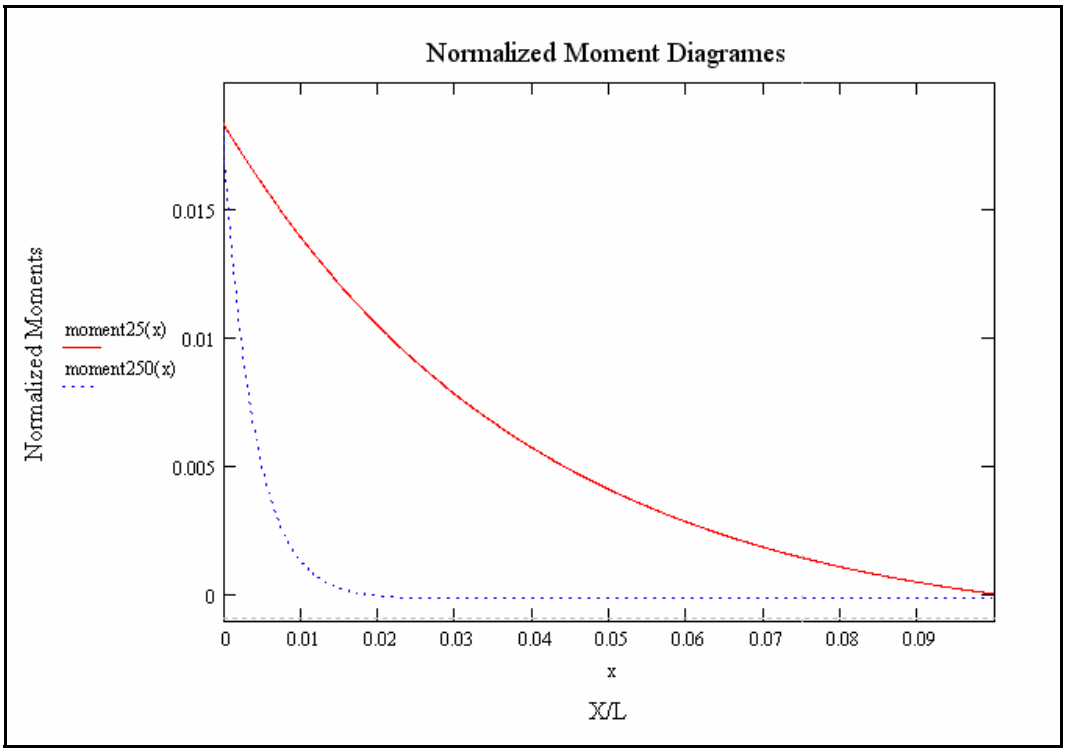

Figure 5.3 Effect of γ on moment gradient for members with equivalent peak bending moments

As can be seen in the figure, even if the peak moments for a given members are the same at the terminations, the moment gradients can be drastically different for different γ. This is an important factor to consider when one is considering the effects that bending stresses might have on the overall fatigue life of a structural element. If an element has a greater amount of material under higher stresses then its overall fatigue life can be shorter than a material with a smaller amount of material subjected to that same level of stress.

5.3 NEW EXPERIMENTAL SETUP

With the preceding discussion in mind, we remark that the stay-cable on the Fred Hartman Bridge we are trying to simulate in our research work has a γ parameter of 292 which is considerably higher than the cutoff value of 49 necessary, per our simple criterion, for cable behavior to govern. While this 650 ft cable's length could never be fully duplicated in a laboratory setting for bending fatigue testing, it is important that any test being performed have a γ parameter that is as close to the cutoff value as possible to ensure a cable-dominant behavior. This is one of the primary design criteria for the proposed experimental setup.

5.3.1 Two-strand specimen – physical characteristics

Whereas it would seem easiest to have simply designed a test specimen with as low a moment of inertia as possible in order to increase γ as much as possible, perhaps by using a single-strand test setup, it was desirable to have strands at some distance away from the neutral axis of the cable. Having multiple strands would thus ensure a more realistic interpretation and calculation of bending stresses in these strands, as the determination of the bending stresses in the strands is based on:

$$\sigma = \frac{M \cdot y}{I} \tag{5.6}$$

where y is the distance of the fiber in question from the neutral axis of the specimen.

It was apparent that two strands would be the minimum number of strands used in designing the test setup. The size of pipe used was based on minimizing the smeared moment of inertia I while still leaving a practical amount of space between the inside of the pipe and the steel strands; 3" was used as the inside

diameter of the pipe. Based on this inner diameter for the pipe the smeared moment of inertia was calculated in Appendix A as 0.674 in^4.

In order to further increase the value of γ for the test setup the values for the tension T and length L were needed to be as large as possible. The length of the specimen is somewhat dictated by the space available in the laboratory and therefore the longest specimen feasible was about 49 feet. The amount of tension in the specimen was, for reasons of safety, kept to a maximum of 50% GUTS. For the 270 ksi strands this corresponds to a tension force per strand of 29 kips. Using the above values γ can be calculated as:

$$\gamma = \sqrt{\frac{T \cdot L^2}{E \cdot I}} = \sqrt{\frac{(2 \cdot 29kips) \cdot (588in)^2}{(27500ksi) \cdot (.674in^4)}} = 32.9 \qquad 5.7$$

Even though the above value is near optimal given the laboratory constraints, it is still away from the cutoff value of 49. However, it improves upon the prior laboratory specimen γ value of 25.9. We remark that the ratio of the actual to the ideal midspan moment becomes $\frac{\hat{M}(0.5;33)}{\hat{M}(0.5;0)} =$ 2.1% versus $\frac{\hat{M}(0.5;25.9)}{\hat{M}(0.5;0)} =$ 3.5%, an improvement of 40 %.

5.3.2 Two-strand specimen – computational model

The primary goal here is to demonstrate computationally that the proposed two-strand specimen is capable of matching the stress range of the field cable as the latter was calculated earlier in Chapter 3. To this end, we modeled the two-strand specimen using finite elements. To model this test setup as accurately as possible we used solid elements (elastic). It was desirable to develop an FEA model without smeared properties, but instead with geometric and material

properties of the grout and steel strands represented as accurately as possible. In order to assess the accuracy of solutions obtained with this ANSYS model, specific results were obtained and compared to solutions obtained with the closed-form Euler-Bernoulli model for determining static bending stresses. The following sections present this information, including a detailed summary of the work done in ANSYS.

5.3.2.1 Model geometry

The steel strands and grout are modeled separately while assuming perfect bond between the two materials (no slip conditions). In the preprocessing phase of the ANSYS model both the grout matrix and the steel strands are created with circles that are later extruded into long cylindrical shapes after having been meshed. See the following figure for a cross section view with dimensions.

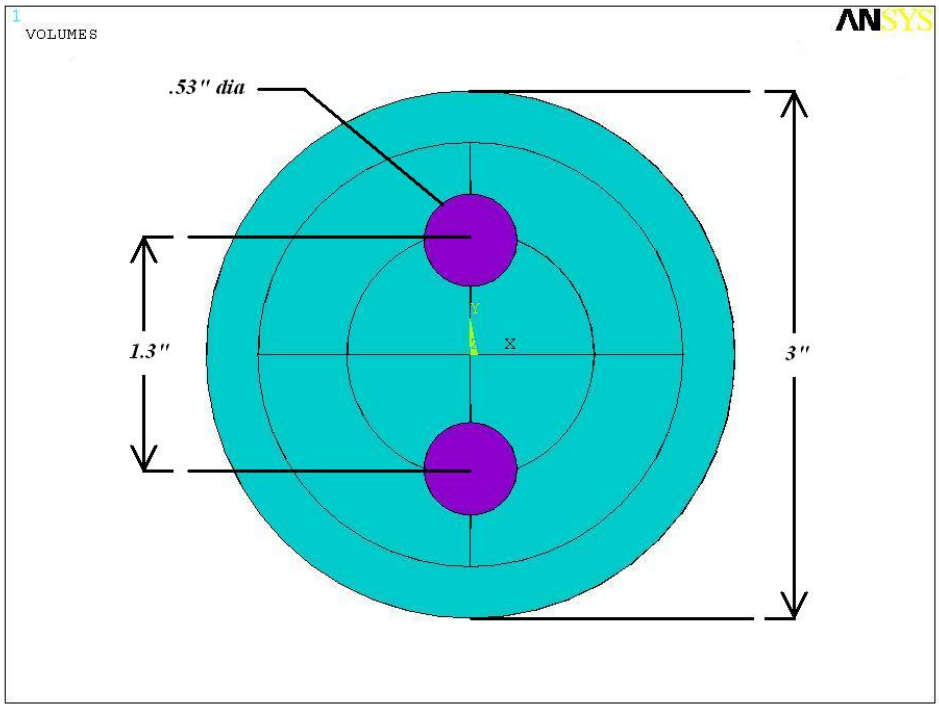

Figure 5.4 Cross-section of ANSYS model

As the use of the actual 7-wire configuration for each strand would complicate the geometry, such that it would greatly increase the refinement of meshing necessary in the model, a circle was used to represent the cross-section of the strands. In order to still accurately represent the actual amount of steel in the seven wire strand the diameter of the representative circle used was chosen such that the area of steel represented in the ANSYS model was equivalent to the actual specimen. It should also be noted that the additional lines and circles in the figure are there only as a means of controlling the meshing on the cross-section and don't represent any break in material properties.

The total length of the specimen in the lab will be 588 in. Taking advantage of symmetric boundary conditions, which will be discussed in greater detail later, the ANSYS model examines only half of the specimen length or, 294 in.

5.3.2.2 Material properties and element types

In order to model the cement-grout matrix surrounding the steel strands SOLID65 solid elements were used. SOLID65 elements are essentially the same as the more common SOLID45 3-D 8-noded solid element except that SOLID65 has crushing and cracking properties not available in SOLID45. In order to use SOLID65 one must enter material properties for the grout which are based on the values given in Chapter 4; compressive strength (f_c'), tensile strength ($7.5\sqrt{f_c'}$), and Young's Modulus ($57\sqrt{f_c'}$). A value of 0.15 was input as the Poisson's ratio for the cement elements, which is a standard value for concrete.

SOLID45 elements were used for the steel strands. This isotropic, 3-D solid-element was given the same value of Young's modulus used for the steel throughout the closed form equations, which was 27,500 ksi. The typical value of 0.33 was input as the Poisson's ratio.

5.3.2.3 Meshing

The meshing was done by first meshing the cross-section with PLANE42 elements, which are the quadrilateral, 2-D complementary elements to the SOLID45 element. After meshing the cross-section properly these elements were then extruded along the length of the cable into the corresponding SOLID45 and SOLID65 elements. After extrusion the original 2-D elements were deleted and only the 3-D solid elements were left.

Much care was taken in this first step of 2-D meshing by dividing the cross-section appropriately to ensure coincident nodes so as to prevent any regions from being overly refined with very small elements. Small elements on the initial cross-section would limit the longitudinal length that they could be extruded because of aspect ratio limits built into ANSYS. This would force a decrease in the allowable length of an element and thus a drastic increase in the total number of elements in the system. With a limit of 128,000 degrees of freedom for the entire system it was necessary to prevent this problem from occurring. That being said the final mesh of the 2-D cross-section can be seen in the following figure.

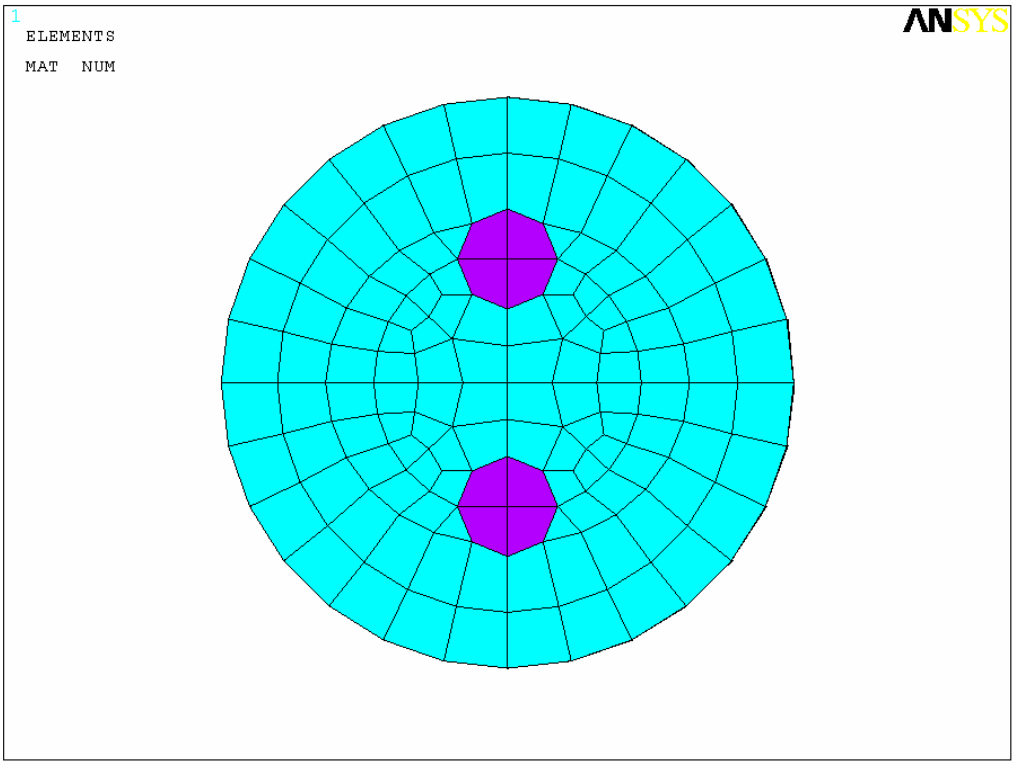

Figure 5.5 2-D mesh of cross-section

After this 2-D mesh was extruded. As the regions near the ends are the areas where the highest curvatures are expected the first 6 in of the model was extruded into much smaller length elements than the majority of the length. An isometric close-up of one of the ends of the full volume mesh is seen in Figure 5.6. The aspect-ratios of all the elements seen were checked for warnings by ANSYS and none was found.

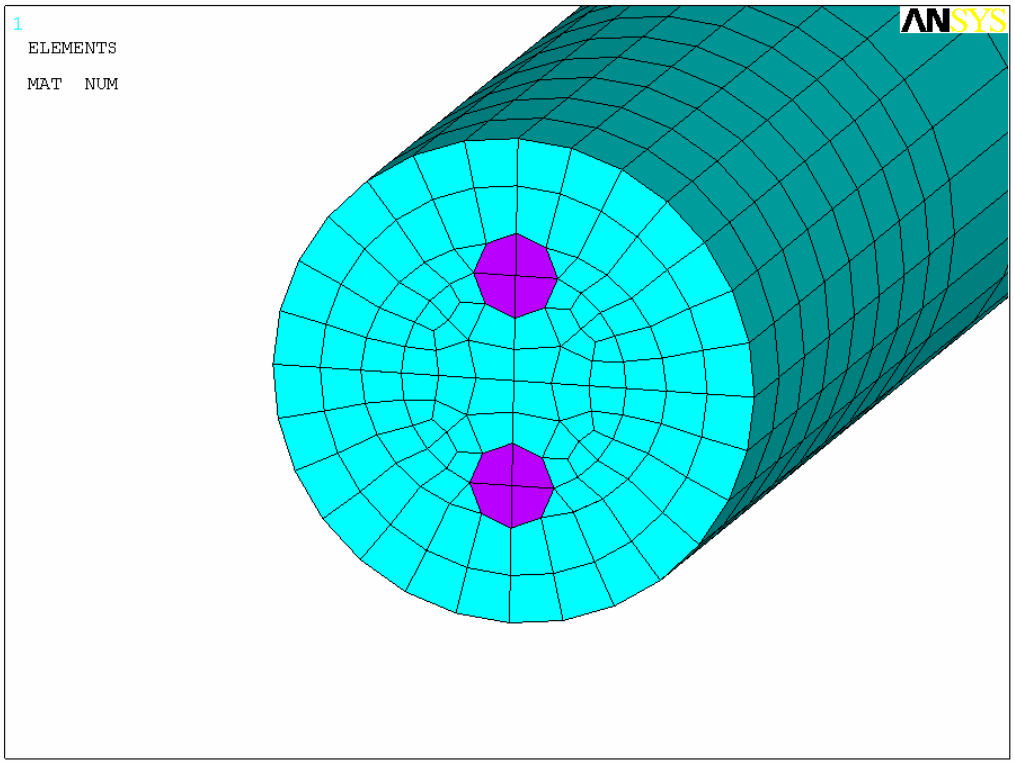

Figure 5.6 3-D extruded mesh

In the discretization of any solid model with even a moderate level of complexity the finite elements created act as an accurate, but approximate representation of the actual shapes. Meshing of the steel strand cross-sections, for instance, involved using only 4 quadrilateral elements whose combined cross-sectional area was 0.196 in^2 while the solid geometry circle representing the steel strand was actually 0.217 in^2 (which is the nominal area of a strand). Our steel elements therefore represent 90.2% of the actual area of the steel strands. Similarly the grout elements represented 99.1% of the actual grout geometry. It is important to note these observations as it implies that if not dealt with the total self-weight of the analyzed system, among other things, would not be representative of the actual system. To compensate for this problem we may

examine the density value that is entered into the material properties for the grout and steel elements. Both densities entered into the ANSYS analysis were therefore obtained by multiplying the actual density by the ratio of the actual area to the discretized area resulting in densities of 0.314 lb/in^3 and 0.0868 lb/in^3 for the steel and cement respectively.

5.3.2.4 Loading and boundary/initial conditions

Continuing on the topic of compensating for lost cross-sectional area we can examine the issue of the assumed tension force to be used in the model. An initial stress condition is used in the FEA to induce the level of tension force that will be applied in the lab. As discussed earlier the tension force that will be applied in the laboratory will be 58 kips between the 2 strands in the cable. Based on the cross-sectional area of the actual strands and their Young's modulus of 27,500 ksi, this would imply an initial stress in the strands of 133.66 ksi. However knowing that we have a slight reduction in our cross-sectional area due to discretization of the strands, this initial stress actually results in a tension force of only 52.29 kips (This value of tension force was verified in ANSYS by checking the reaction forces at the ends of the steel strands under a negligible but, present, lateral load). In order to reach the necessary value of tension force in the system the initial stress of 133.66 ksi was multiplied by the same ratio of actual area to discretized area used for the densities and the required tension force of 58 kips was reached. As non-linear behavior will not be expected in the ANSYS model for the steel strands we do not need to be concerned with this increase in steel stress in the finite element analysis, we need only realize that when final results are obtained for bending stresses in the strands they are higher than the actual values expected in the laboratory testing by the same increase in the initial stress state input into ANSYS.

Full fixity is assumed at both ends of our specimen and as such it is important that measures are taken in the laboratory to ensure this is the case during the test as well. As mentioned before, in order to reduce computation time while increasing the number of possible elements used, the ANSYS model represents one half of the total length of 588 in. In order to make such a model it is important to discuss what kind of boundary conditions and symmetric assumptions were used.

At the location corresponding to one of the fixed ends all the nodes were restricted in the X, Y, and Z directions (rotations need not be explicitly restricted as the elements used have degrees of freedom in these three directions only and therefore any rotational constraint is implicit; Figure 5.7).

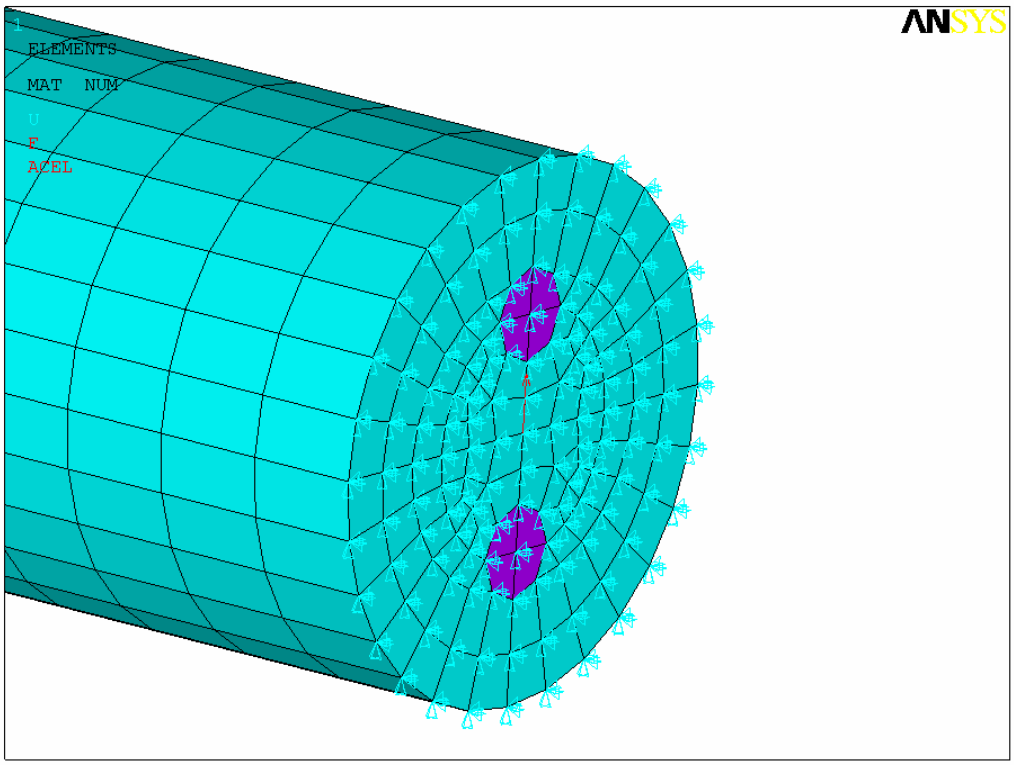

Figure 5.7 Fixed-end boundary conditions

At the mid-span location where the ANSYS model is cut in half certain boundary conditions are assumed based on the symmetry of the test setup. Based on the longitudinal symmetry at this point all nodes here should be restricted for motion in the longitudinal direction (Z). Any movement in the X-direction is also constrained here even though there is negligible external reaction in the X-direction. This assumption is made to prevent out of plane motion that was observed during a second-order analysis done without constraints in the X-direction there. Motion in the Y-direction is left unrestrained (Figure 5.8)

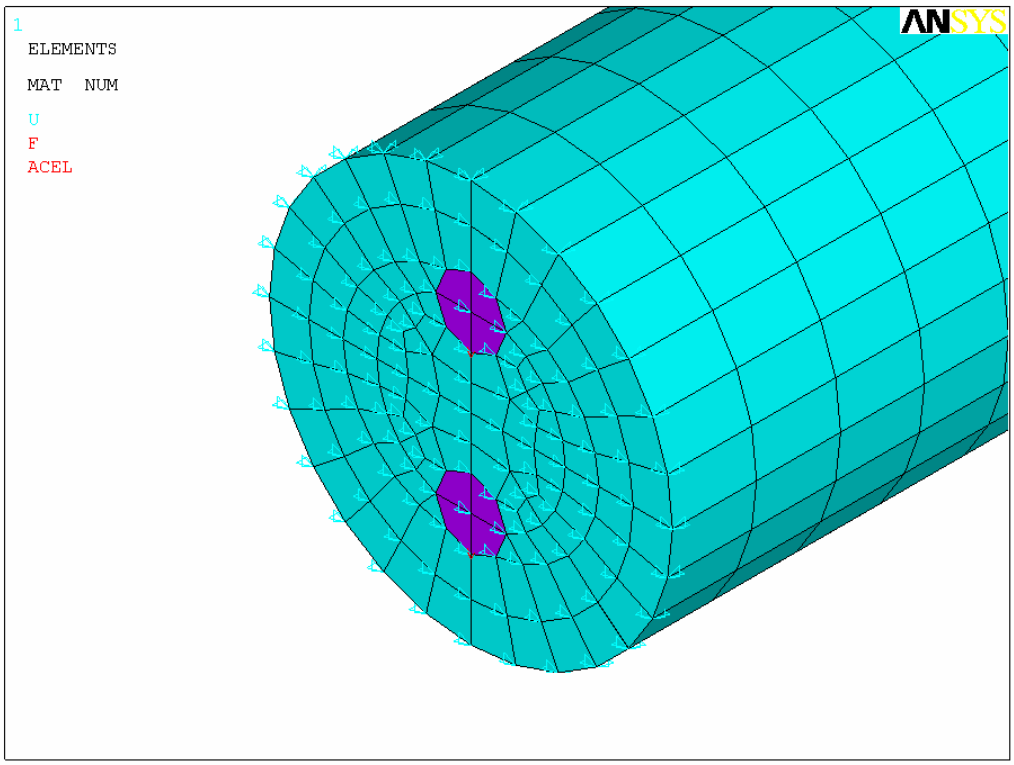

Figure 5.8 Mid-span symmetric boundary conditions

The initial analysis performed was done to try and determine how accurate the ANSYS modeling was in comparison to the static solution obtained using closed-form solutions. In the model of the two-strand closed-form solution

performed similar to that shown in Appendix B, there is a single point load in addition to the self-weight of the system. While the next analysis that will be discussed will use a slightly more distributed load to simulate the actual geometry of the loading clamp to be used, this first analysis discussed refers specifically to a point load used in the system in order to validate the ANSYS model. That being said the point load was applied at the mid-span point, which because of the symmetry assumptions made appears as the left end of the specimen. Application of the load was distributed along all the nodes of the steel elements lying along the face of the mid-span point. Problems occurred when the load was applied at any of the nodes of grout elements due to the material's non-linearity. The problem arises if an exterior concrete element crushes or cracks and there is a load applied on a node corresponding to the failed element. Significant element distortion is induced and convergence may not be reached. A simple and accurate solution is to make sure that the load is applied to only the steel elements in a fashion similar to the figure below (Figure 5.9), created with the grout elements taken out of the image for clarity.

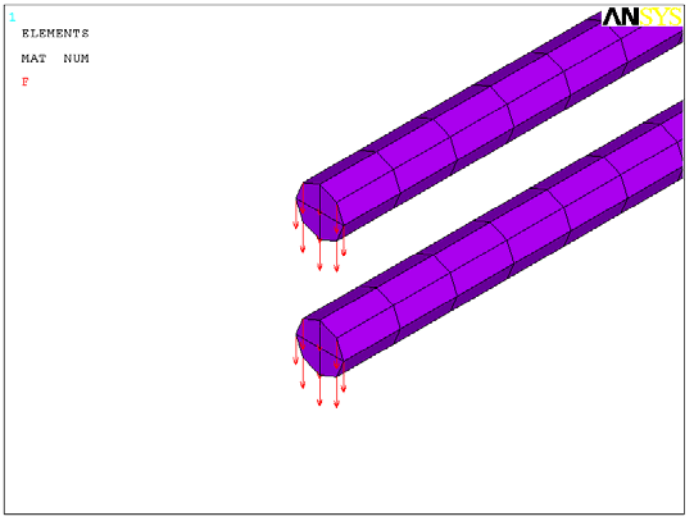

Figure 5.9 Point-load application in ANSYS verification model

5.3.2.5 Solution approach

Because of the great amount of flexibility of the cable and the relatively large displacements expected the "large displacement static" analysis option was run with a full Newton-Raphson, non-linear, iterative procedure. Because of the large displacements and the non-linear behavior of the grout in the system it was found that the best substep size for convergence was a minimum of 0.05 and a maximum of 0.2. To help prevent against solution instabilities and facilitate the convergence the Newton-Raphson line search parameter option was turned on as well.

5.3.2.6 Results and comparison

A comparison of both the original closed-form solution and the solution obtained from the ANSYS model would provide a good means to gauge the accuracy of the computer model. The original governing Euler-Bernoulli equation was used with the given parameters of the two-strand test setup (an example of this approach is in Appendix B) to calculate approximate bending stresses. In order to determine what load to use the load was increased (in one-direction of bending) in the closed-form equation until the bending stress obtained was equal to the 54.34 ksi in only one-direction of loading, which was the value determined by the dynamic analysis of Chapter 3. It should be noted here that this closed-form solution assumes the grout has fully deteriorated at the anchor head and the moment of inertia at the point is composed only of the contribution from the steel strands. This value of moment of inertia is seen in Appendix A as .191 in^4. This is perhaps a conservative assumption that the grout contribution to moment of inertia is negligible, and the assumption will be later discussed after results are obtained.

Based on these assumptions the closed-form solution was used in Appendix B to calculate displacements and bending stresses and it was determined that in order to reach the required stress level of 54.34 ksi the point-load required was .983 kips. The displacement corresponding to this level of stress was found to be 2.65 in at the mid-span of the cable. This load of .983 kips was then used in the ANSYS model, applied as previously described, to determine if the ANSYS model was producing bending stresses and displacements consistent with the analytical model.

An image of the deflected shape under this load as solved by ANSYS is seen below, scaled 30 times to help show the displaced shape. It is interesting to observe that only near the point loading (left-side) and the anchorage (right-side) is there significant curvature or a "kinking" of the cable. This is in agreement with the idea discussed earlier that for cables with very low flexural rigidities and high tension forces, indicative of a high γ parameter, bending stresses are only developed near terminations and loading points. The rest of the cable's length is dominated by axial forces. It is also indicative of the assumption that the areas nearest the ends needed to be discretized with a finer mesh.

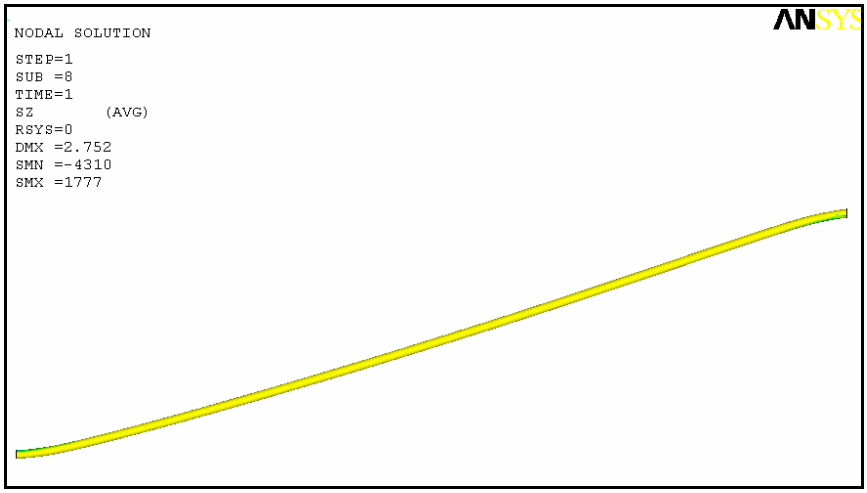

Figure 5.10 Scaled displaced shape under a point load

Upon running the ANSYS model, the data were monitored for peak bending stresses and displacement under the described point load. A comparison of the ANSYS data obtained with the same point load as used in the closed-form solution is shown in the table below. It should be reminded here that the ANSYS model takes symmetry into account and therefore the actual point load applied is only half of the point load used in the closed-form solution.

Table 5.1 Comparison of bending stress for ANSYS and closed-form models

Comparison of ANSYS and Analytical Solution							
Analysis Type	**Load** (kips)	**Disp.** (in)	**ANSYS Stress Results**		**Normalized Stresses**		**Stress Range (ksi)**
			Max. (ksi)	Initial (ksi)	Max. (ksi)	Initial (ksi)	
ANSYS	0.983	2.75	192.2	148.2	173.3	133.7	39.65
Closed-Form	0.983	2.65	--	--	188.0	133.7	54.34

In the table above the maximum stress refers to the peak tensile stress, which is a combination of the axial tension and the bending stresses, for the steel strands. It should be reiterated here that the maximum bending stress in the ANSYS model is not exactly representative of the expected maximum bending stress in the laboratory setup. This disparity is due to the altered initial stress input into the steel strands in the ANSYS necessary, due to the difference between the actual steel strand area and the discretized area in the solid modeling. The initial stress input into ANSYS for the steel strands is 148.2 ksi, while the expected initial stress in the steel strands in the laboratory setup will be 133.6 ksi. Described earlier in this section, the initial stress was higher in the ANSYS model to ensure that the tension force was 58 kips, as it is in the closed-form modeling and will be in the laboratory testing. This ratio of stresses (based on the ratio of discretized area to actual) is used to "normalize" the stress range value given by ANSYS for the actual setup. We can look at the contour plots for the steel strands' longitudinal stresses near the anchorage face and the mid-span.

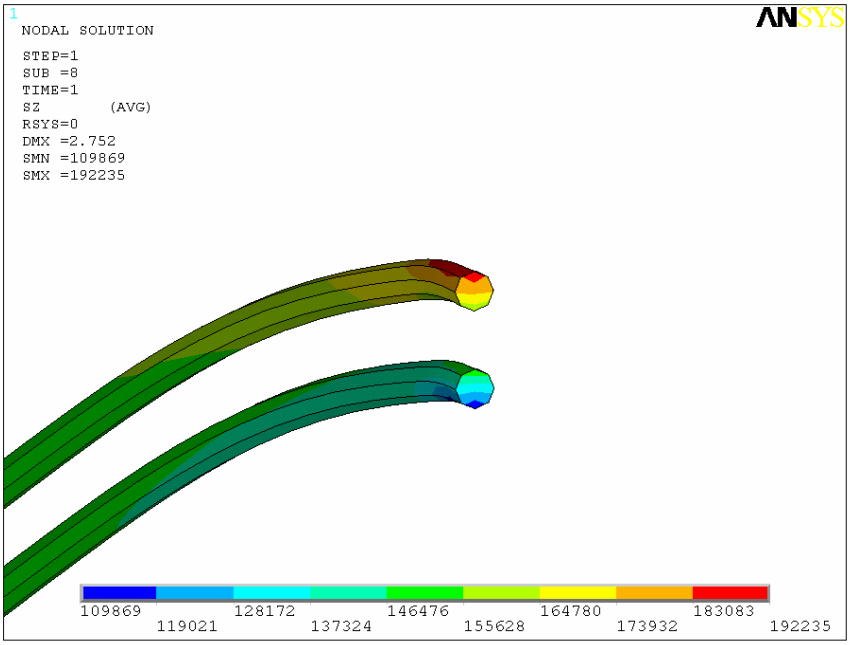

Figure 5.11 Oblique view of bending stresses at the anchorage (units in lbs/in^2)

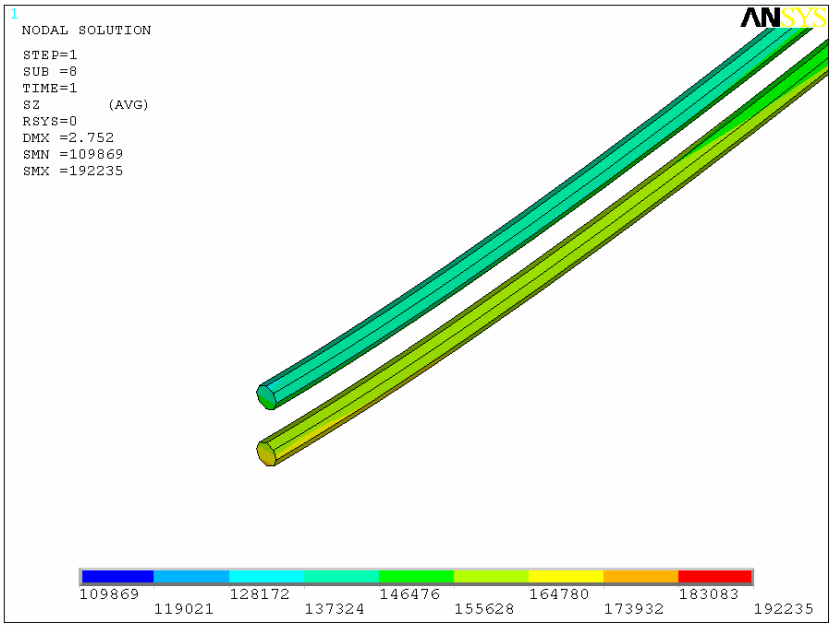

Figure 5.12 Isometric view of bending stresses at mid-span (units in lbs/in^2)

While the results from the ANSYS model for displacement in Table 5.1 are within 3.8% of the values obtained from the closed-form solution, there is a larger discrepancy seen between the stress range predicted by the closed-form solution and the ANSYS results. As described before, in order to calculate the bending stresses with the closed-form solution an assumption was made about the moment of inertia at the terminations. In the calculation of bending stresses with the closed-form solution the extreme case of complete grout deterioration was assumed for the moment of inertia used. This would intuitively provide conservative values of bending stresses for the steel strands. Upon investigation of the ANSYS solution we see that in fact, there is still some capacity in the grout at the anchor head, suggesting why the ANSYS model has lower longitudinal stresses in the steel strands than the more conservative closed-form solution. Figure 5.13 is a contour stress plot (longitudinal direction) of the grout elements close to the anchorage face demonstrating the additional capacity left in some of the grout.

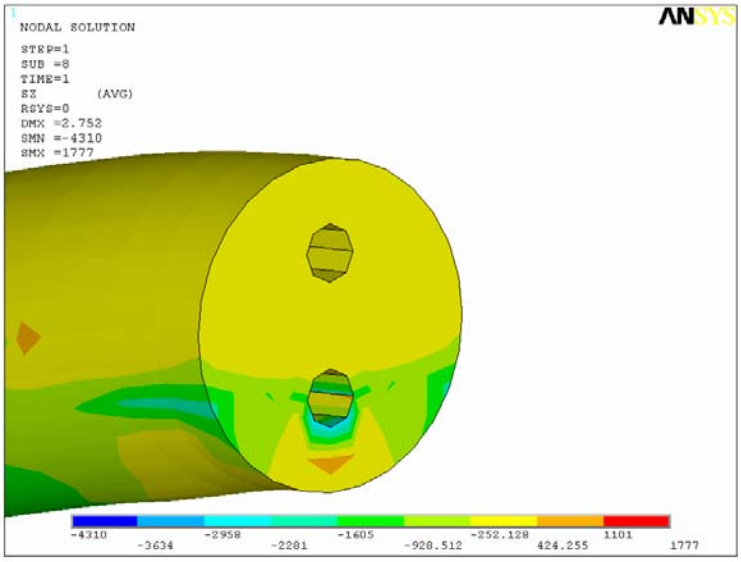

Figure 5.13 Longitudinal grout stresses at the anchorage face (units in lbs/in^2)

In Figure 5.13 we can see from the stress relaxation in the top of the cross-section (tension region) that the elements here have lost their tensile capacity or, cracked. It is also apparent however that there is still some compressive capacity in the grout in the lower region of the cross-section here.

These images from ANSYS are justification for having used a reduced moment of inertia in the closed-form solution, however the disparity between bending stresses calculated using the closed form solution and the ANSYS model suggests that the assumption that the grout had no contribution to the transformed moment of inertia in the closed-form solution may have been conservative and produced bending stresses that were too high. In general though, we have established that the ANSYS model is a reasonable one, and it would seem wise to use this model as a more accurate means of calculating bending stresses than the closed-form solution, as the ANSYS model takes into account non-linear material behavior and the subsequent effect on the distribution of bending stresses along the cross-section of the cable.

As such, another model was run in ANSYS to more closely model the actual loading method in the laboratory and better approximate the load necessary to match the required cyclic stress range of 54.34 ksi predicted for Cable #24 with the dynamic finite element modeling discussed in Chapter 3.

5.3.2.7 Loading clamp expected stresses

In the actual application of the load in the laboratory test setup a clamp will be used that is approximately 7 inches long. In order to be as closely representative as possible of the actual test setup the final FEA model of the laboratory specimen will take this loading clamp into consideration. The load is therefore applied by distributing the total load among the steel elements in the

first 3.5 inches of the left edge of the model. The application of the distributed load along the first few steel elements is seen in Figure 5.14

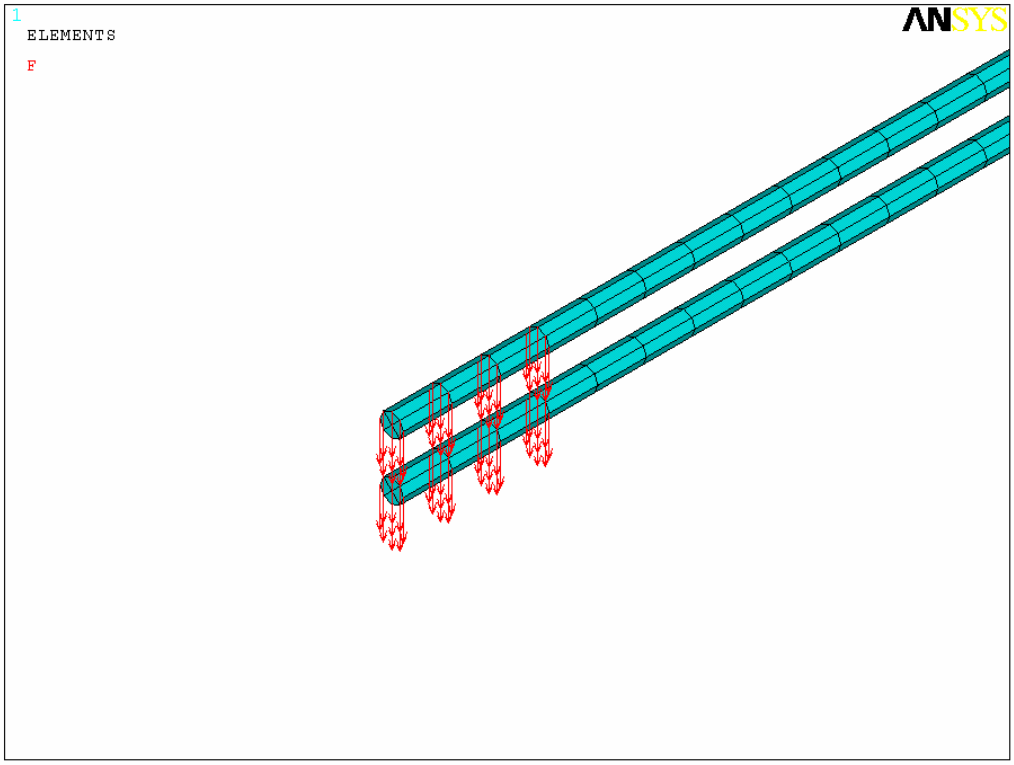

Figure 5.14 Loading clamp application

The same type of analysis was run as in the previous section where the ANSYS model was run at different loads to determine what load would be necessary to induce the equivalent bending stresses in the laboratory model that were calculated for Cable #24 earlier. The aim is to reach a total bending stress range of 54.34 ksi in a strand. A series of analyses were conducted, as the exact value of load necessary to induce the required stresses had to be narrowed down. The closest value obtained was 54.31 ksi, which was within 1% of the required bending stress range of 54.34 ksi. The specifications and results for this test are seen in the table below.

Table 5.2 Results for matched bending stresses

ANSYS Results under Loading Clamp						
Total Load @ midspan (kips)	Displacement (in)	Stress Results		Normalized Stresses		Stress Range
		Max. (ksi)	Initial (ksi)	Max. (ksi)	Initial (ksi)	(ksi)
1.35	3.56	208.4	148.2	187.9	133.6	54.3

It is worthwhile to elaborate on these results seen in Table 5.2. The maximum stress value obtained was induced on the top strand (under tensile longitudinal stresses from bending). The initial stress value given is the stress that was input into ANSYS based on the tension in the strands before testing. Both these stresses must be "normalized" into equivalent values of stress that will be actually experienced in the laboratory model. This is due to the previously described issue of loss of area of the steel strands in the meshing process. The difference between the two normalized areas corresponds to the bending stress range for the top steel strand at the anchorage face (Figure 5.15 and Figure 5.16).

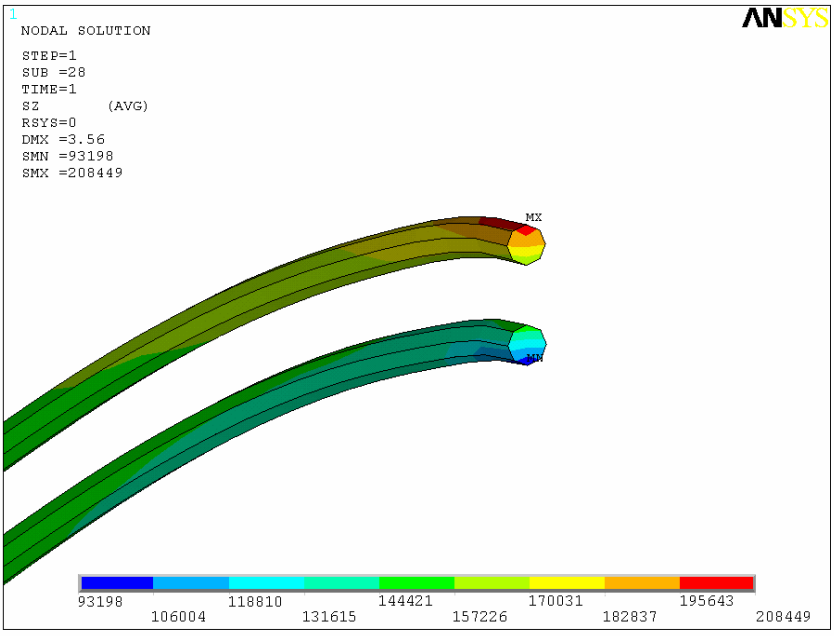

Figure 5.15 Longitudinal steel stress at anchorage (units in lbs/in^2)

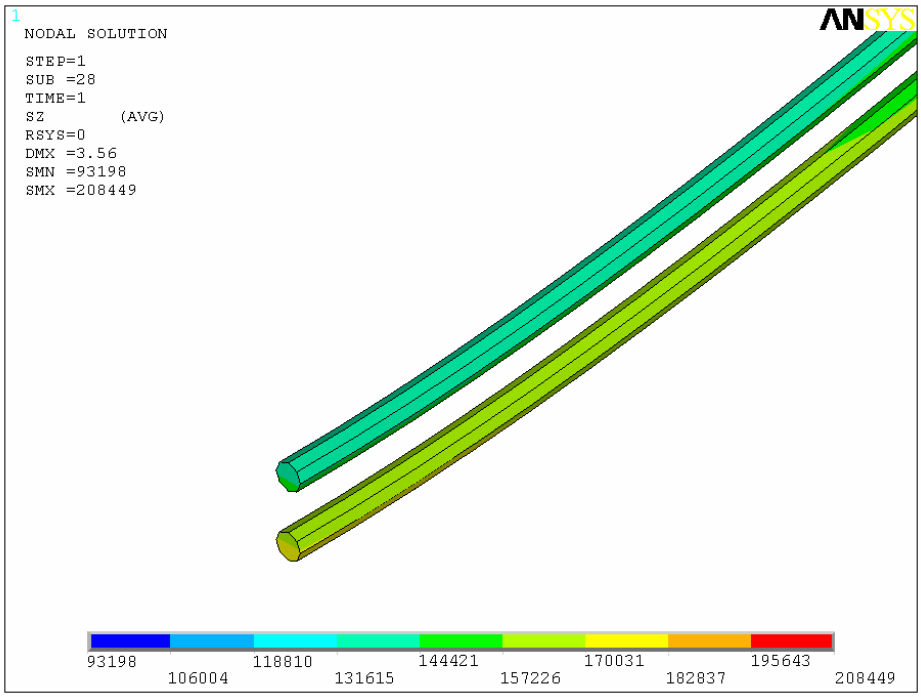

Figure 5.16 Longitudinal steel stress at mid-span (units in lbs/in^2)

Looking also at images of the grout longitudinal stresses will give us a good indication of what behavior to expect from the grout during testing. The following images demonstrate that at the anchorage face, there is significant loss of grout capacity, especially in the tension region, but there is however a small amount of capacity left. This would seem to indicate that the assumption of complete loss of grout capacity would have been slightly conservative in estimating bending stresses with the closed-form solution.

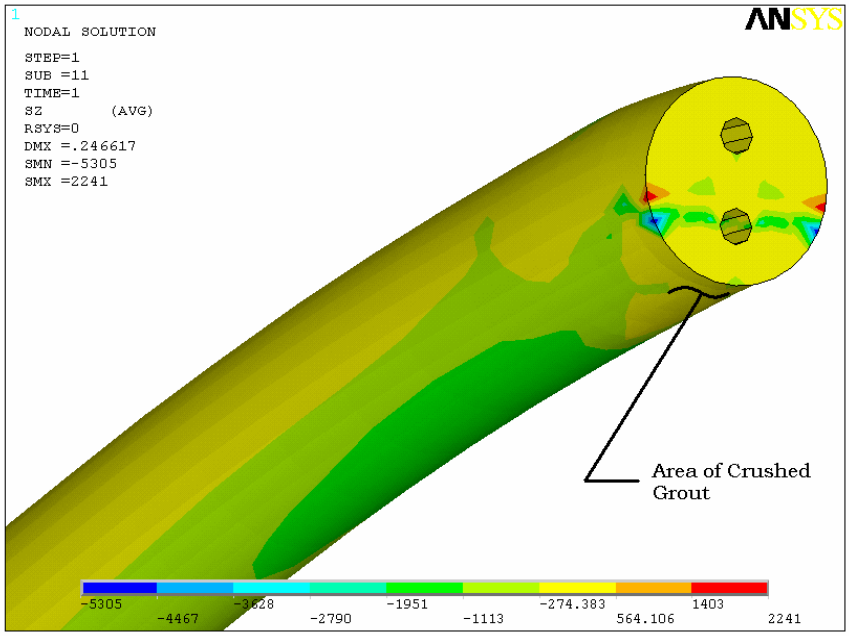

Figure 5.17 Longitudinal stress in the grout at the fixed-end (units in lbs/in^2)

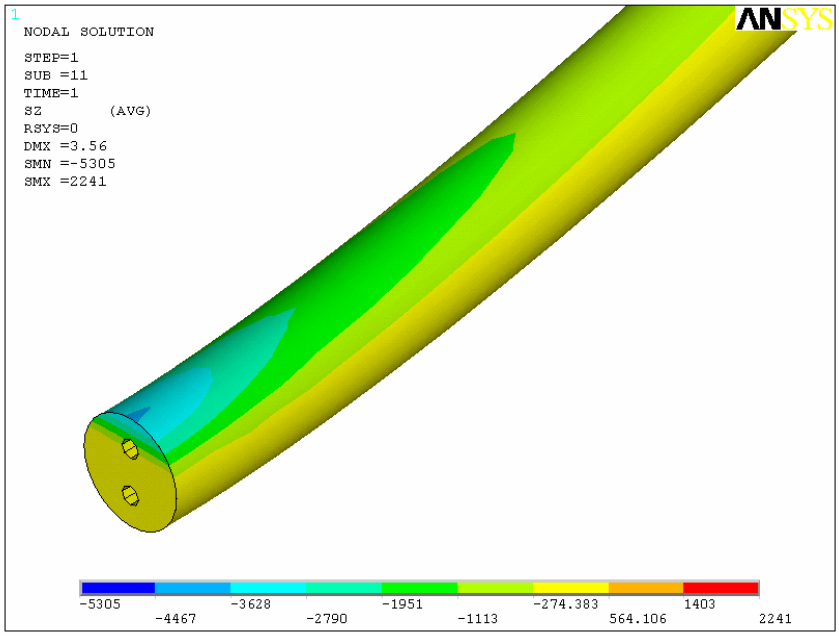

Figure 5.18 Longitudinal stress in the grout at the mid-span (units in lbs/in^2)

It might be beneficial to examine the rates of change of the bending stress near the terminations for later discussions of fatigue effects. Figure 5.19 is a plot of the axial stresses at the nodes along the extreme vertical points of the top steel strand, which undergoes the greatest bending stresses, versus the length of the specimen. This graph can give us a general idea of how quickly the stresses change as we move away from the anchorage.

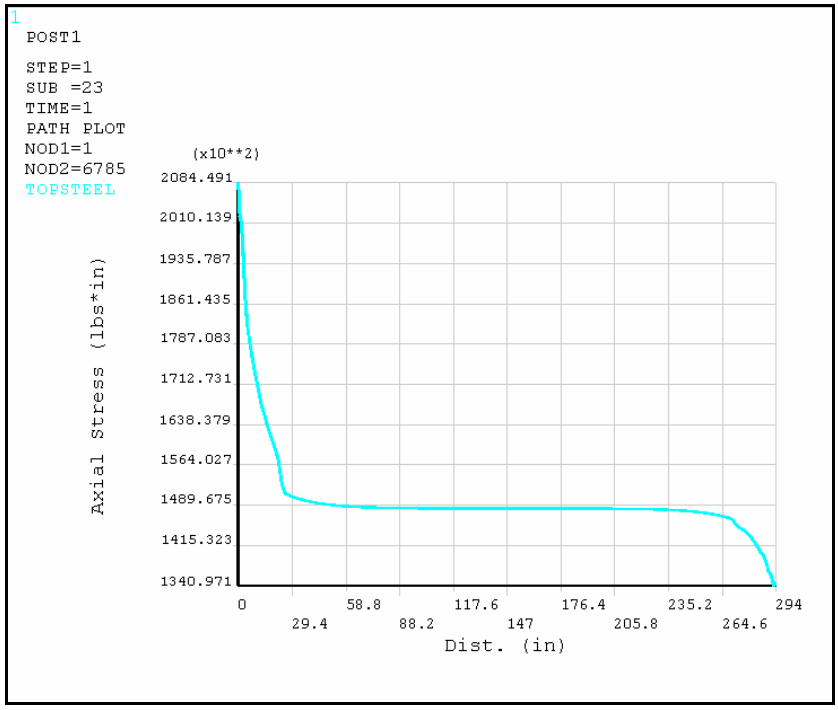

Figure 5.19 Overall rate of change of extreme fiber tension stress

As we can see in the image the stress gradient near the anchorage at the left is much steeper than it is along the majority of the length. It is also apparent that for the majority of the length of the cable the tensile stress in the steel is relatively uniform as it is not governed by bending stresses, but by the axial forces induced in the cable by the increase in overall length due to deflection. We can look even closer at the stress gradient of the extreme fiber of the top steel strand

near the anchorage. We can see in Figure 5.20 that within the first two feet of the length the axial stress has decreased from its peak value to almost the uniform axial stress induced in the strands by the pre-tensioning force and the displacements.

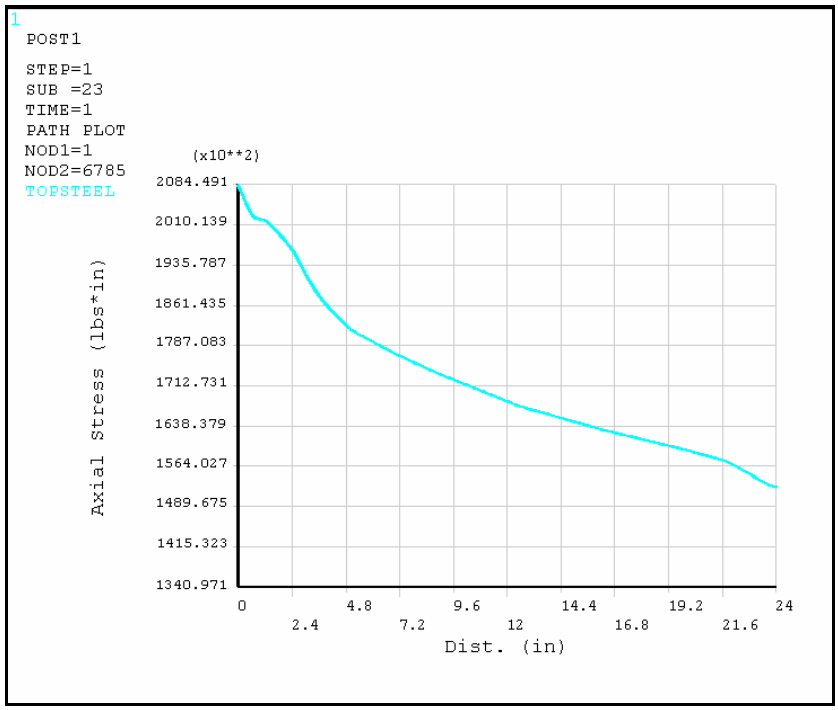

Figure 5.20 Close-up of stress gradient for peak tensile steel strand

As we can see in the image the tensile stress in the top steel strand drops of more than 50 ksi from its peak value near the anchorage in the first two feet away from the anchorage.

The impact of these stress values, as well as the apparent stress gradients, expected in the specimen as calculated in this section will be discussed in the following section in terms of a possible correlation to fatigue life.

5.3.2.8 Loading and displacement for testing

In summary, in order to best match the bending stresses for Cable #24, calculated in Chapter 3, it is has been shown that a load of 1.35 kips will be required at mid-span of the specimen. The displacement expected under this load should be 3.56 in and the maximum bending stress induced on the top strand directly at the anchorage face should be 54.3 ksi. It is recommended that static tests be initially performed and that strain gauges be applied to monitor the stress levels at this location. Matching the required bending stress of 54.3 ksi should be the critical goal, and as such, the testing should be "displacement-controlled" such that the testing displacement should induce this required stress level during the static tests.

CHAPTER 6
Observations and Conclusions

6.1 SUMMARY

The first objective accomplished in this work was to present a plausible scenario for the observed large-amplitude cable vibrations recorded in April, 1997 on the Fred Hartman Bridge. As this video was the only means for characterizing the behavior observed for Cable #24, it was imperative that the field behavior be matched with a computational model. The dynamic finite element analysis conducted was reasonably successful in characterizing the field behavior as is evidenced by the satisfactory agreement between the finite element-based animation and the actual video recording. We believe that the observed motion was due to the cyclic movement of the deck, and therefore of the cable's anchorage to the deck as well, which, in turn, was due to wind- (and/or rain-) induced deck vibrations. We believe that the observed motion is a standing wave corresponding to the first anti-symmetric cable mode. We have also shown that the cables neighboring Cable #24 do not experience as dramatic a motion as Cable #24, which again is consistent with the recorded vibrations.

Furthermore, based on the same computational model, we have extracted the range of bending stresses experienced by Cable #24 during the large-amplitude motion.

After the bending stress range for the field case was quantified, prior laboratory experiments were also computationally modeled in an attempt to estimate bending stress ranges for these tests. A comparison between the field and laboratory stress ranges was performed at the end of chapter 4 and it was shown

that the stress level in the laboratory models is below what was computed based on the field observations.

With this in mind, in Chapter 5, we proposed a new series of tests that will better match the expected stresses based on the field observations. In addition to this better matching of the expected field stress levels, we also investigated possible improvements that could be made to better match the experimental model's parameters to those of a field cable. Further computational modeling was done to characterize the necessary displacement and loading for the laboratory setup, and to better understand the stress gradients near the anchorages of the laboratory model.

6.2 OBSERVATIONS

As mentioned earlier in the thesis the amount of research that has been done on the topic of fatigue life of grouted, steel strands under cyclic bending loads is perhaps not extensive enough. While there has been quite a lot of work done in studying the fatigue life of steel strands under only axial cyclic loading, there is still great opportunity for improving our basic understanding of how cyclic bending can affect fatigue. There is reason to believe (Raoof 1993) that the traditional means for estimating fatigue damage of steel strands may not be completely applicable for situations involving cyclic bending stresses. The traditional approach for calculating the fatigue life of stay-cables (PTI, 2000) is based on the strands' service-life under solely axial cyclic loading. If one were to use these models to estimate the reduction in service life of steel strands under pronounced cyclic bending, one would simply use the range of longitudinal stresses induced by the bending in the equations based on axial cyclic loading. For example, if a strand had some mean axial stress due to pre-tensioning, and cyclic

longitudinal stresses induced on the strand were +30 ksi and -30 ksi, we might be inclined to base the strand's fatigue life on the axial cyclic loading data for that strand with a stress range of 60ksi (it has generally been determined (Hobbs and Ghavami, 1982) from axial fatigue tests that a strand's fatigue life is insensitive to the mean axial stress).

The most pronounced qualitative difference between axial fatigue tests and bending fatigue tests lies in the amount of material undergoing the longitudinal cyclic stress range. In an axial fatigue test of a strand the entire strand length is subject to the cyclic stress range. In a bending fatigue test there may be only a very small, critical region where these cyclic stresses are induced. This would seem to suggest, as (Poser, 2001) has also noted, that an axial fatigue test has a higher likelihood than materials with imperfections would be exposed to the given stress range, whereas a bending test has a much lower likelihood that imperfections exist in the limited region of high stresses.

This issue is of relevance to our investigations into the effects of dynamics on bending stresses when we review the effect that the γ parameter, as discussed in Chapter 5, has on the stress gradient of a structural element. Returning to Figure 5-3, repeated here for clarity (Figure 6.6.1), we can see the effect that γ has on the stress gradient for two elements with the same peak value for bending moment.

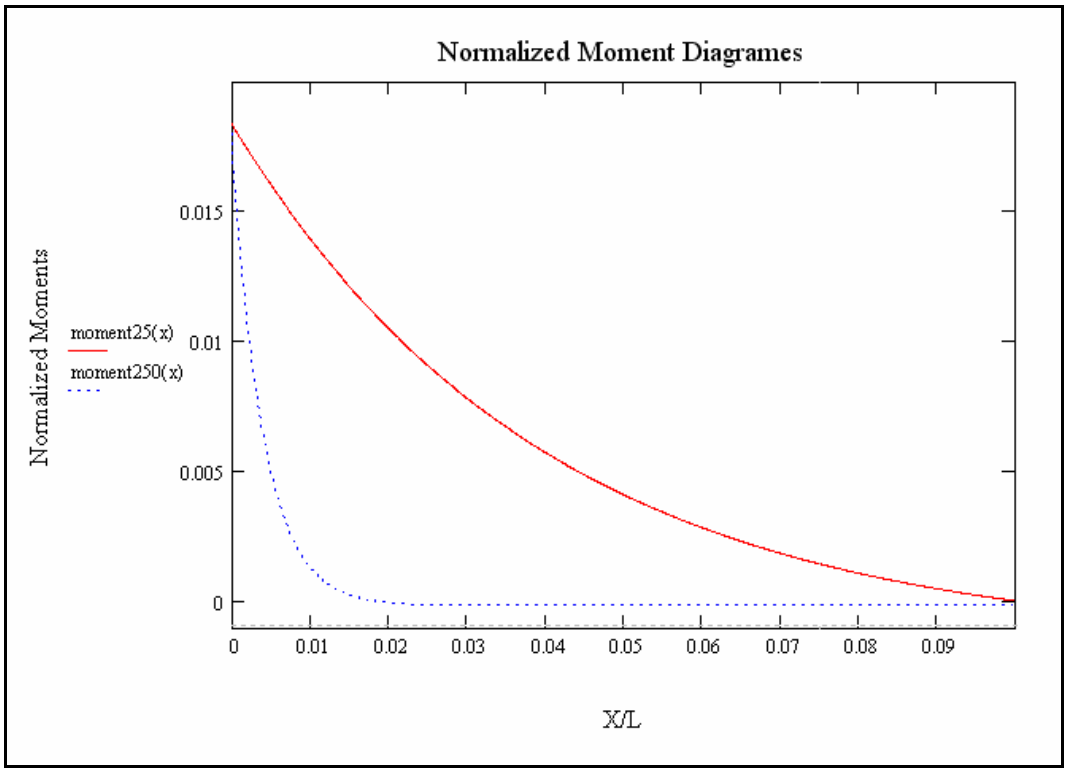

Figure 6.6.1 Effect of γ on moment gradient for members with equivalent peak bending moments (Fig. 5-3 repeated)

As the figure clearly shows elements with higher γ have much steeper stress gradients even when they have the same peak stress as a more "beam"-like element. This would seem to suggest that as we examine elements of increasing γ

the likelihood that their bending fatigue life can be easily characterized by the strands axial fatigue life diminishes, because a far smaller amount of material is being subjected to the stress levels in question.

6.3 AXIAL FATIGUE LIFE ESTIMATES

In axial fatigue testing done on the 270K 7-wire strands in question (Ridd 2004) their performance was compared to the axial fatigue design criteria set forth by the Post-Tensioning Institute in 1986 and 2001. The Fred Hartman Bridge was constructed after 1986 but well before any new fatigue provisions made in 2001 and we might assume that fatigue life was designed based on the 1986 provisions.

We can make an attempt here to apply these axial fatigue provisions for the bending cases as well. Using the equations for fatigue life given by the Post-Tensioning Institute (1986) for axial fatigue life we can make a reasonable assessment as to the fatigue life of the strands based on the bending stress ranges determined by the ANSYS model. Work done previously (Willox, 1998) used the same failure criteria that are used here but for much higher predicted bending stresses. The estimation for total number of cycles is given as such:

$$N = \frac{A}{\left(.75 \cdot \Delta F\right)^3} \tag{6.1}$$

Where;

ΔF = Stress range (MPa)

A = Fatigue Constant for Parallel Strands (MPa)

N = Total Number of Cycles

From the ANSYS model we have determined that the total expected stress range for the steel strands will be 54.3 ksi or, 379 MPa. The fatigue constant A for parallel strands is given as 39.3e11 (PTI, 2001). With these values we can obtain an estimate for the life-span of a strand under these stresses as;

$$N = 171{,}116 \tag{6.2}$$

This may seem like a low number of cycles until strand failure but we have to remember that this isn't the life-span for the strand under normal traffic loading conditions. These large bending stresses were only induced during the

wind-rain conditions. Furthermore it is important to reiterate that these equations developed by the Post-Tensioning Institute are based on axial fatigue tests, which for the reasons described earlier, may be conservative for elements with high γ values where the amount of material undergoing this stress range is extremely small. The results from the ANSYS model of the new test setup support this concept of a very small region of these high stress ranges. Seen below is a reproduction of Figure 5.20 which shows the quick drop-off in stresses of the extreme fiber of steel stress in the first 2 feet of length.

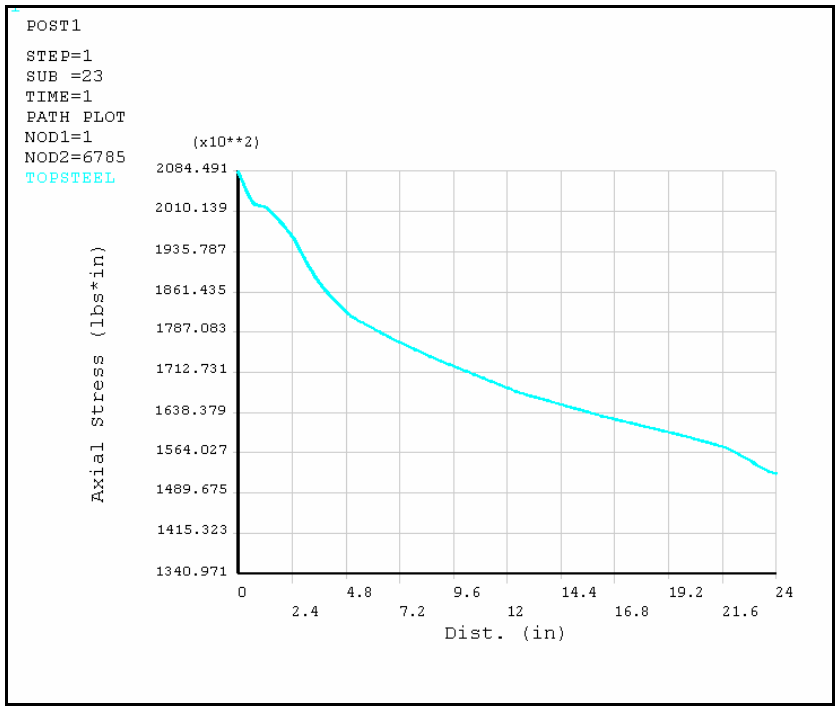

Figure 6.6.2 Close-up of stress gradient for peak tensile steel strand

It is certain that in Cable #24, which has a much higher γ the stress gradient at the anchorages is even steeper, representing an even further departure from the axial fatigue model.

6.4 CONCLUSIONS

6.4.1 On the modeling of stay-cables

We distinguish two cases: experimental and computational modeling. The discussion and results presented herein are based on relatively simple models (both experimental and computational) for simulating highly complex fluid-structure nonlinear transient physical phenomena, as those arising under wind (possibly turbulent) and/or rain conditions on a cable-stayed bridge with a slender profile. As such, there is much more that needs to be done: on the experimental front, it is imperative that the specimens adhere as closely as it is physically possible to the actual cable field behavior, as, at a minimum, dictated by the γ parameter. But, more importantly, both from an experimental and computational viewpoint it is necessary to tightly test the various hypotheses for the causes of large-amplitude vibrations discussed in Chapter 2 (galloping, vortex shedding, etc). Despite the fact that we feel confident that our own hypothesis is quite plausible, it is important to recall that the hypothesis holds for one day –the day the video recording was made. It is probable that any of the other candidate causes mentioned in Chapter 2 may be responsible for similar events during another day. Of those causes mentioned the most intriguing one, both from a theoretical and an experimental point of view, is the scenario of rivulets altering the aerodynamic profile of the cables during wind-rain conditions. It is suggested that it be the subject of future investigations.

6.4.2 On fatigue issues of stay-cables

The estimated number of cycles until strand failure for the laboratory setup, predicted at the beginning of this chapter, are based on the most current design approaches used for estimating the fatigue life of steel strands in stay-

cables. These limits for fatigue life were based on axially-loaded fatigue testing of 7-wire strands. As discussed, these axial tests may not be synonymous to bending fatigue tests of 7-wire strands because of the significantly reduced amount of material being subjected to the high stress ranges in a bending test. It is the author's belief that the fatigue tests to be performed on the two-strand test setup should prove the estimates for total number of cycles calculated in this chapter to be conservative. If this is the case it would lend credit to the theory that the PTI-recommendations for fatigue life of stay-cable strands is more aptly applied to situations where the fatigue loading is primarily axial.

It would seem that with such a small area of high stress ranges in flexural fatigue situations some consideration for the effects of fretting between the outer layers of wires in the strands, or between other strands in the cross-section should be considered. (Raoof, 1993) has done some extensive work in this area of fretting between wires in bending fatigue problems for multi-layer strands as discussed earlier. Those investigations focused on multi-layer strands with at least 3-layers of wires in the strands and as such, the equations developed in the investigation are not applicable to the 7-wire strands which have only 2 layers of wires (including the core wire).

As such the tests to be performed should provide an interesting avenue of research in understanding the effect (or lack thereof) that relatively high bending stresses have on the fatigue life of 7-wire strands and therefore the validity of applying axial fatigue design criteria to situations involving flexure of steel-stranded stay-cables.

APPENDIX A
Smeared Properties

A.1 BEAM MODELING

For the purposes of modeling the tested specimens and Cable #24 from the Fred Hartman Bridge in the static and dynamic closed-form and FE analysis, transformed, or "section", properties were needed. The following sections contain the calculations for the smeared section properties of the analyzed stay-cable from the bridge, Cable #24.

A.1.1 Fred Hartman Bridge Cable #24

As is the case for the calculations of I for all the cables in question, the stiffness contribution of the PE pipe surrounding the grout and steel strands was considered negligible and not used in the calculations.

The plan-drawings for the cross-section of Cable #24 were based on the maximum number of strands, 55, that were in cables of the same group. Cable #24 had only 50 strands and the figure below, taken from the structural drawings, provides the most reasonable assumption of the arrangement of those strands in the free-length as since the exact arrangement is not known. Strands that are blacked out in the figure represent the locations of plausible vacant strand locations.

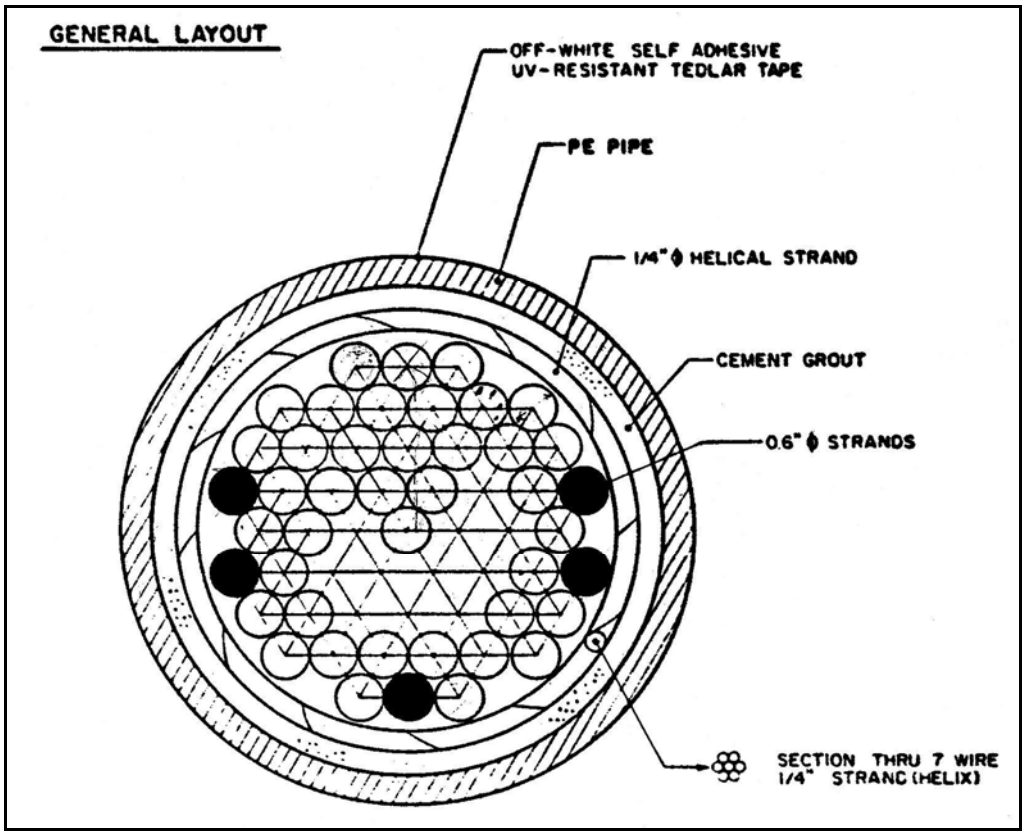

Figure A.1 Cross-Section of Cable #24

The following are the smeared property calculations made for Cable #24 of the Fred Hartman Bridge. All dimensions used for these calculations are available in the TXDOT plan drawings (C 389-12-52), part 4, S112.

Moment of Inertia for Cable #24:

Modulus - Strand: $E_{strand} := 27500 \quad ksi$

Modulus - Grout: $E_{Grout} := 3500 \quad ksi$

Inner Diameter Free length - PE: $ID_{fl} := 5.58in$

Diameter - Wire: $d_{wire} := .2in$

Diameter - Strand: $d_{str} := .6in$

Area - Wire: $A_{wire} := \frac{d_{wire}^2}{4} \cdot \pi$ $\quad A_{wire} = 0.031\,in^2$

Area - Strand: $A_{str} := 7 \cdot A_{wire}$ $\quad A_{str} = 0.21991149\,in^2$

Moment of Inertia - Individual Strand: $I_{str} := 7 \cdot \left(\frac{\pi \cdot d_{wire}^4}{64} \right) + \frac{A_{str}}{7} \cdot \left[2 \cdot d_{wire}^2 + 4 \cdot \left(\frac{d_{wire}}{2} \right)^2 \right]$

$I_{str} = 0.00431969\,in^4$

Moment of Inertia of the steel for the free length:

$$I_{SFL} := 50 \cdot (I_{str}) + 2 \cdot A_{str} \cdot \left[2.5 \cdot (4 \cdot d_{str})^2 + 6 \cdot (3 \cdot d_{str})^2 + 7 \cdot (2 \cdot d_{str})^2 + 6 \cdot (d_{str})^2 \right]$$

$I_{SFL} = 20.483027\,in^4$

We want to develop a smear moment of inertia (ref. Poser);

$$n := \frac{E_{strand}}{E_{Grout}}$$

$n = 7.857$

Moment of Inertia of the grout at free length:

$$I_{gfl} := \left(\frac{\pi \cdot ID_{fl}^{4}}{64}\right) - I_{SFL}$$

$$I_{gfl} = 27.106\,in^4$$

Smeared moment of inertia in free length:

$$I_{FL} := I_{SFL} + \frac{I_{gfl}}{n}$$

$$I_{FL} = 23.933\,in^4$$

Free-length transformed area based on transformed moment of inertia

$$A := \frac{\pi}{4} \cdot \left[\left(\frac{I_{FL} \cdot 64}{\pi}\right)^{\frac{1}{4}}\right]^2 \qquad A = 17.342\,in^2$$

Anchor HEad

$$I_{sah} := 50 \cdot I_{str} + 2 \cdot A_{str} \cdot \left[2.5 \cdot (3.68 \cdot in)^2 + 6 \cdot (2.76 \cdot in)^2 + 7 \cdot (1.84 \cdot in)^2 + 6 \cdot (.92 \cdot in)^2\right]$$

$$I_{sah} = 47.866\,in^4$$

$$I_{gah} := \left[\frac{\pi \cdot (8.46 \cdot in)^4}{64}\right] - I_{sah}$$

$$I_{gah} = 203.584\,in^4$$

$$I_{AH} := I_{sah} + \frac{I_{gah}}{n}$$

$$I_{AH} = 73.777\,in^4$$

A.1.2 Tested Laboratory Specimens

The same procedure was used to calculate the smeared moments of inertia for the cross-sections of tested specimens #1-10. These cross-sections are as seen in Figure 4.8 and Figure 4.9 with the appropriate dimensions.

Specimen 1 moment of inertia:

Modulus - Strand: $E_{strand} := 27500 \ ksi$

Modulus - Grout: $E_{Grout} := 3500 \ ksi$

Inner Diameter Free length - PE: $ID_{fl} := 3.94 \cdot in$

Inner Diameter Anchor Head-PE $ID_{ah} := 6.69 in$

Diameter - Wire: $d_{wire} := 5.05 \cdot mm$ $d_{wire} = 0.199 \, in$

$d_{str} := .6 in$

Area - Wire: $A_{wire} := \frac{d_{wire}^2}{4} \cdot \pi$ $A_{wire} = 0.031 \, in^2$

Area - Strand: $A_{str} := 7 \cdot A_{wire}$ $A_{str} = 0.21732178 \, in^2$

Moment of Inertia - Strand:

$$I_{str} := 7 \cdot \left(\frac{\pi \cdot d_{wire}^4}{64} \right) + \frac{A_{str}}{7} \cdot \left[2 \cdot d_{wire}^2 + 4 \cdot \left(\frac{d_{wire}}{2} \right)^2 \right]$$

$I_{str} = 0.00421855 \, in^4$

Moment of Inertia of the steel for the free length:

$$I_{SFL} := 19 \cdot (I_{str}) + A_{str} \cdot \left[4 \cdot (.3325 in)^2 + 6 \cdot (.665 in)^2 + 4 \cdot (.9975 in)^2 + 2 \cdot (1.33 in)^2 \right]$$

$$I_{SFL} = 2.386675\,in^4$$

We want to develop a smear moment of inertia (ref. Poser);

$$n := \frac{E_{strand}}{E_{Grout}}$$

$$n = 7.857$$

Moment of Inertia of the grout at free length:

$$I_{gfl} := \left(\frac{\pi \cdot ID_{fl}^{\,4}}{64}\right) - I_{SFL}$$

$$I_{gfl} = 9.443\,in^4$$

Smeared moment of inertia in free length:

$$I_{FL} := I_{SFL} + \frac{I_{gfl}}{n}$$

$$I_{FL} = 3.588\,in^4$$

Moment of Inertia of the steel at the anchor head:

$$I_{SAH} := 19 \cdot (I_{str}) + 2 \cdot A_{str} \cdot \left[(2.6 \cdot in)^2 + 2(1.95 \cdot in)^2 + 3 \cdot (1.3 \cdot in)^2 + 2 \cdot (.65 \cdot in)^2\right]$$

$$I_{SAH} = 8.894724\,in^4$$

Moment of Inertia of the grout at the anchor head:

$$I_{GAH} := \left(\frac{\pi \cdot ID_{ah}^{\,4}}{64}\right) - I_{SAH}$$

$$I_{GAH} = 89.433\,in^4$$

Smeared moment of inertia at the anchor head:

$$I_{AH} := I_{SAH} + \frac{I_{GAH}}{n}$$

$$I_{AH} = 20.277\,in^4$$

Specimens 2-4,7,9,10-12 Moment of Inertia:

Moduls - Strand: $E_{strand} := 27500 \quad ksi$

Moduls - Grout: $E_{Grout} := 3500 \quad ksi$

Inner Diameter Free length - PE: $ID_{fl} := 3.94 \cdot in$

$I_{nom} := 1.3 \cdot in$

Inner Diameter Anchor Head-PE $ID_{ah} := 6.69 in$

Diameter - Wire: $d_{wire} := 5.05 \cdot mm$ $d_{wire} = 0.199\,in$

$d_{str} := .6 in$

Area - Wire: $A_{wire} := \frac{d_{wire}^{2}}{4} \cdot \pi$ $A_{wire} = 0.031\,in^2$

Area - Strand: $A_{str} := 7 \cdot A_{wire}$ $A_{str} = 0.21732178\,in^2$

Moment of Inertia - Strand: $I_{str} := 7 \cdot \left(\frac{\pi \cdot d_{wire}^{4}}{64} \right) + \frac{A_{str}}{7} \cdot \left[2 \cdot d_{wire}^{2} + 4 \cdot \left(\frac{d_{wire}}{2} \right)^{2} \right]$

$I_{str} = 0.00421855\,in^4$

Area - Steel: $A_S := 19 \cdot A_{str}$ $A_S = 4.129\,in^2$

Moment of Inertia - Strand: $I_{str} := 7 \cdot \left(\frac{\pi \cdot d_{wire}^{4}}{64} \right) + \frac{A_{str}}{7} \cdot \left[2 \cdot d_{wire}^{2} + 4 \cdot \left(\frac{d_{wire}}{2} \right)^{2} \right]$

$I_{str} = 0.00421855\,in^4$

Area - Steel: $A_S := 19 \cdot A_{str}$ $A_S = 4.129\,in^2$

Moment of Inertia of the steel for the free length:

$I_{SFL} := 19 \cdot (I_{str}) + A_{str} \cdot \left[6 \cdot (2 \cdot d_{str})^2 + 8 \cdot (d_{str})^2 \right]$

$I_{SFL} = 2.583699\,in^4$

Moment of Inertia of the steel at anchor head:

$I_{SAH} := 19 \cdot (I_{str}) + A_{str} \cdot \left[6 \cdot (2.25in)^2 + 8 \cdot (1.125in)^2 \right]$

$I_{SAH} = 8.882\,in^4$

We want to develop a smear moment of inertia (ref. Poser);

$n := \frac{E_{strand}}{E_{Grout}}$

$n = 7.857$

Moment of Inertia of the grout at free length:

$I_{gfl} := \left(\frac{\pi \cdot ID_{fl}^{4}}{64} \right) - I_{SFL}$

$I_{gfl} = 9.245\,in^4$

Smeared moment of inertia in free length:

$I_{FL} := I_{SFL} + \frac{I_{gfl}}{n}$

$I_{FL} = 3.76\,in^4$

Moment of Inertia of the grout at the anchor head

$$I_{gah} := \left[\frac{\left(\pi \cdot ID_{ah}^{4}\right)}{64}\right] - I_{SAH}$$

$$I_{gah} = 89.446\,in^4$$

Smeared moment of Inertia at the anchor head:

$$I_{AH} := I_{SAH} + \frac{I_{gah}}{n}$$

$$I_{AH} = 20.266\,in^4$$

Specimen 5 & 8 moment of inertia

Moduls - Strand: $E_{strand} := 27500$ ksi

Moduls - Grout: $E_{Grout} := 3500$ ksi

Inner Diameter Free length - PE: $ID_{fl} := 3.94 \cdot in$

$I_{nom} := 1.3 \cdot in$

Inner Diameter Anchor Head-PE $ID_{ah} := 6.69in$

Diameter - Wire: $d_{wire} := 5.05 \cdot mm$ $d_{wire} = 0.199\,in$

$d_{str} := .6in$

Area - Wire: $A_{wire} := \frac{d_{wire}^{2}}{4} \cdot \pi$ $A_{wire} = 0.031\,in^2$

Area - Strand: $A_{str} := 7 \cdot A_{wire}$ $A_{str} = 0.21732178\,in^2$

Moment of Inertia - Strand: $I_{str} := 7 \cdot \left(\frac{\pi \cdot d_{wire}^{4}}{64} \right) + \frac{A_{str}}{7} \cdot \left[2 \cdot d_{wire}^{2} + 4 \cdot \left(\frac{d_{wire}}{2} \right)^{2} \right]$

$I_{str} = 0.00421855\,in^4$

Area - Steel: $A_S := 19 \cdot A_{str}$ $A_S = 4.129\,in^2$

Moment of Inertia of the steel for the free length:

$I_{SFL} := 19 \cdot I_{str}$

$I_{SFL} = 0.080152\,in^4$

Moment of Inertia of the steel at anchor head:

$I_{SAH} := 19 \cdot (I_{str}) + A_{str} \cdot \left[4 \cdot (2.25in)^2 + 4 \cdot (1.125in)^2 \right]$

$I_{SAH} = 5.581\,in^4$

Specimen 6 moment of inertia

Moduls - Strand: $E_{strand} := 27500$ ksi

Moduls - Grout: $E_{Grout} := 3500$ ksi

Inner Diameter Free length - PE: $ID_{fl} := 3.94 \cdot in$

$I_{nom} := 1.3 \cdot in$

Inner Diameter Anchor Head-PE $ID_{ah} := 6.69in$

Diameter - Wire: $d_{wire} := 5.05 \cdot mm$ $d_{wire} = 0.199\,in$

$d_{str} := .6in$

Area - Wire: $A_{wire} := \frac{d_{wire}^2}{4} \cdot \pi$ $A_{wire} = 0.031\,in^2$

Area - Strand: $A_{str} := 7 \cdot A_{wire}$ $A_{str} = 0.21732178\,in^2$

Moment of Inertia - Strand: $I_{str} := 7 \cdot \left(\frac{\pi \cdot d_{wire}^4}{64} \right) + \frac{A_{str}}{7} \cdot \left[2 \cdot d_{wire}^2 + 4 \cdot \left(\frac{d_{wire}}{2} \right)^2 \right]$

$I_{str} = 0.00421855\,in^4$

Area - Steel:

$A_S := 19 \cdot A_{str}$ $A_S = 4.129\,in^2$

Moment of Inertia of the steel for the free length:

$I_{SFL} := 13 \cdot (I_{str}) + A_{str} \cdot \left[4 \cdot (2 \cdot d_{str})^2 + 4 \cdot (d_{str})^2 \right]$

$I_{SFL} = 1.619558\,in^4$

Moment of Inertia of the steel at anchor head:

$I_{SAH} := 13 \cdot (I_{str}) + A_{str} \cdot \left[4 \cdot (2.25in)^2 + 4 \cdot (1.125in)^2 \right]$

$I_{SAH} = 5.556\,in^4$

We want to develop a smear moment of inertia (ref. Poser);

$$n := \frac{E_{strand}}{E_{Grout}}$$

$$n = 7.857$$

Moment of Inertia of the grout in the free length:

$$I_{gfl} := \left(\frac{\pi \cdot ID_{fl}^{4}}{64}\right) - I_{SFL}$$

$$I_{gfl} = 10.21\,in^4$$

Smeared moment of inertia in the free length:

$$I_{FL} := I_{SFL} + \frac{I_{gfl}}{n}$$

$$I_{FL} = 2.919\,in^4$$

Moment of Inertia of the grout at the anchor head

$$I_{gah} := \left[\frac{\left(\pi \cdot ID_{ah}^{4}\right)}{64}\right] - I_{SAH}$$

$$I_{gah} = 92.772\,in^4$$

Smeared moment of Inertia at the anchor head:

$$I_{AH} := I_{SAH} + \frac{I_{gah}}{n}$$

$$I_{AH} = 17.363\,in^4$$

The dimensions for the cross-section of the proposed 2-stranded test, along with the associated transformed section properties are seen below.

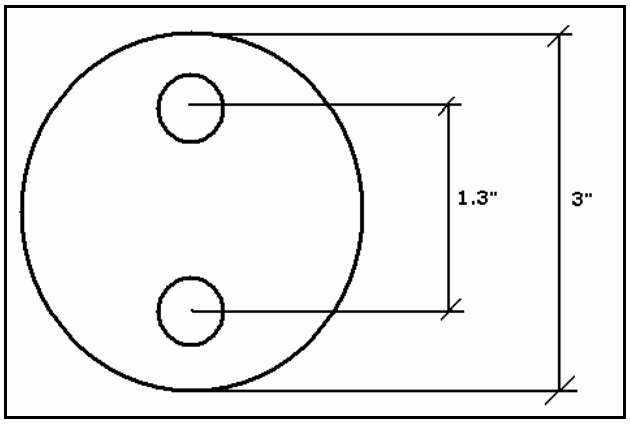

Test 2-strand moment of inertia:

Modulus - Strand: $E_{strand} := 27500 \quad ksi$

Modulus - Grout: $E_{Grout} := 3500 \quad ksi$

Inner Diameter Free length - PE: $ID_{fl} := 3in$

Diameter - Wire: $d_{wire} := 5.05 \cdot mm$ $\quad d_{wire} = 0.199\,in$

$d_{str} := .6in$

Area - Wire: $A_{wire} := \frac{d_{wire}^{2}}{4} \cdot \pi$ $\quad A_{wire} = 0.031\,in^2$

Area - Strand: $A_{str} := 7 \cdot A_{wire}$ $\quad A_{str} = 0.21732178\,in^2$

Moment of Inertia - Strand: $I_{str} := 7 \cdot \left(\frac{\pi \cdot d_{wire}^{4}}{64} \right) + \frac{A_{str}}{7} \cdot \left[2 \cdot d_{wire}^{2} + 4 \cdot \left(\frac{d_{wire}}{2} \right)^{2} \right]$

$I_{str} = 0.00421855\,in^4$

Area - Steel:

$A_S := 2 \cdot A_{str} \qquad A_S = 0.435\,in^2$

Moment of Inertia of the steel for the free length:

$I_{SFL} := 2 \cdot (I_{str}) + 2A_{str} \cdot (.65 \cdot in)^2$

$I_{SFL} = 0.192074\,in^4$

We want to develop a smear moment of inertia (ref. Poser);

$$n := \frac{E_{strand}}{E_{Grout}}$$

$n = 7.857$

Moment of Inertia of the grout at free length:

$$I_{gfl} := \left(\frac{\pi \cdot ID_{fl}^{\,4}}{64} \right) - I_{SFL}$$

$I_{gfl} = 3.784\,in^4$

Smeared moment of inertia in free length:

$$I_{FL} := I_{SFL} + \frac{I_{gfl}}{n}$$

$I_{FL} = 0.674\,in^4$

APPENDIX B
Closed-Form Solutions

B.1 STATIC CASE

B.1.1 Euler-Bernoulli Beam Equation

The familiar Euler-Bernoulli Beam equation for a structural element under tension, a point load at its mid-span, and uniform self-weight is given as;

$$EI \cdot \frac{d^4 w}{dx^4} - T \cdot \frac{d^2 w}{dx^2} = P \cdot \delta\left(x - \frac{L}{2}\right) + mg \qquad \text{B.1}$$

where; E is Young's Modulus, I denotes the second moment of inertia, w is vertical displacement, T is the tension force, P the applied load multiplying the dirac delta function, m is the mass per unit length, and g is gravitational acceleration.

The general solution:

$$w(x) = -\frac{P}{T} \cdot \left(x - \frac{L}{2}\right) \cdot H\left(x - \frac{L}{2}\right) + \frac{P}{T} \cdot \sqrt{\frac{EI}{T}} \cdot H\left(x - \frac{L}{2}\right) \cdot \sinh\left(\sqrt{\frac{T}{EI}} \cdot \left(x - \frac{L}{2}\right)\right) - \frac{mg}{2T} \cdot x^2$$

$$+ c_1 + c_2 \cdot x + c_3 \cdot \sinh\left(\sqrt{\frac{T}{EI}} \cdot x\right) + c_4 \cdot \cosh\left(\sqrt{\frac{T}{EI}} \cdot x\right) \qquad \text{B.2}$$

Applying the boundary conditions for the fixed-fixed structural element we obtain the four necessary equations needed to solve for the constants c_1, c_2, c_3, and c_4.

For brevity's sake the solution is shown for only the first specimen tested. The values obtained for all other tests were computed similarly with the appropriate material and geometry properties computed in Appendix A, and

Chapter 4. From these Maple files the displacements and bending stresses shown in Chapter 4 were derived for all the grouted specimens.

Specimen 1:

```
> E:=27500; #Steel young's modulus (ksi)
```

$$E := 27500$$

```
> Ifu:=3.58; #The uncracked free-length moment of inertia (in^4)
```

$$Ifu := 3.58$$

```
> Ifc:=2.39; #Free-length moment of inertia, no grout contribution (in^4)
```

$$Ifc := 2.39$$

```
> Iau:=20.277; #The uncracked anchor head moment of inertia (in^4)
```

$$Iau := 20.277$$

```
> Iac:=8.89; #The anchor head moment of inertia, no grout contribution
  (in^4)
```

$$Iac := 8.89$$

```
> P:=7.6; #Load at midspan (kips)
```

$$P := 7.6$$

```
> L:=395.375; #Length of specimen (in)
```

$$L := 395.375$$

```
> T:=445; #Tension in cable (kips)
```

$$T := 445$$

```
> po:=evalf(.861/(E*Ifu*L),32);
```

$$po := .22119648738179692280618316116048\ 10^{-7}$$

```
> K:=evalf(sqrt((T/(E*Ifu))),32);
```

$$K := .067231398502797413016290162354523$$

```
> M:=evalf(sqrt(P/(E*Ifu)),32);
```

$$M := .00878615652434495882565866914352 24$$

```
> with(linalg):
> cf:=array([[1,0,0,1],[0,1,K,0],[1,L,evalf(sinh(K*L),32),evalf(cosh(K*L),3
  2)],[0,1,evalf(K*cosh(K*L),32),evalf(K*sinh(K*L),32)]]);
```

$$cf :=$$

$$\begin{bmatrix} 1 & 0 & 0 & 1 \\ 0 & 1 & .067231398502797413016290162354523 & 0 \\ 1 & 395.375 & .17507267361808431414109706632626\ 10^{12} & .17507267361808431414109992228310\ 10^{12} \\ 0 & 1 & .11770380686967613906595422475888\ 10^{11} & .11770380686967613906595230465915\ 10^{11} \end{bmatrix}$$

```
> s:=array([[0],[0],[evalf(((M/K)^2)*(L/2)-((M^2)/(K^3))*sinh(K*L/2)+(po*(L
```

```
^2)/(2*K^2)),32)],[evalf(((M^2)/(K^2))*(1-cosh(K*L/2))+(po*L/(K^2)),32)]]
);
```

$$s := \begin{bmatrix} 0 \\ 0 \\ -75154.311451696593814056745149468 \\ -5052.963153494713261796579745973 3 \end{bmatrix}$$

```
> sols:=evalf(evalm(inverse(cf) &* s),32);
```

$$sols := \begin{bmatrix} -.14140287012614301947378922 58 \\ .00950674157303370786516534552 \\ -.14140329942174480328289737 14 \\ .14140287012614301947378922 58 \end{bmatrix}$$

```
> d:=evalf(-((M^2)/(K^2))*(z-(L/2))*Heaviside(z-L/2)+((M^2)/(K^3))*Heavisid
e(z-(L/2))*sinh(K*(z-(L/2)))-(po*z^2/(2*K^2))+sols[1,1]+sols[2,1]*z+sols[
3,1]*sinh(K*z)+sols[4,1]*cosh(K*z),32);
```

$$d := -.017078651685393258426966292134831 (z - 197.68750000000000000000000000000) \text{ Heaviside}(z - 197.68750000000000000000000000000) + .254027910555551472627439087372 31 \text{ Heaviside}(z - 197.68750000000000000000000000000) \sinh(.067231398502797413016290162354523 z - 13.290807091521763585657861470460) - .244683080704920303935603732766 85\, 10^{-5} z^2 - .141402870126143019473789225 8 + .009506741573033707865165345 52 z - .141403299421744803282897371 4 \sinh(.067231398502797413016290162354523 z) + .141402870126143019473789225 8 \cosh(.067231398502797413016290162354523 z)$$

```
> moment:=evalf(E*Ifu*diff(d,z,z),32); #Moment as a function of x in terms
of uniform cross-section as derived
```

$$moment := -3362.786516853932584269662921348 2 \text{ Dirac}(\%2) - 1681.393258426966292134831460674 1 \%2 \text{ Dirac}(1, \%2) + 25009.047794194042480171378151804 \text{ Dirac}(1, \%2) \sinh(\%1) + 3362.786516853932584269662921348 2 \text{ Dirac}(\%2) \cosh(\%1) + 113.042420197220405319210393880 67 \text{ Heaviside}(\%2) \sinh(\%1) - .481780985907988078449203749817 93 - 62.924468242676437460889330273000 \sinh(.067231398502797413016290162354523 z) + 62.924277206133643665836205480999 \cosh(.067231398502797413016290162354523 z)$$

$$\%1 := .067231398502797413016290162354523 z - 13.290807091521763585657861470460$$

$$\%2 := z - 197.68750000000000000000000000000$$

```
> moment_end:=evalf(subs(z=0,moment),32); #Moment evaluated at anchorage
```

$$moment\_end := 62.582032524628394482554346986446$$

```
> moment_midspan:=evalf(subs(z=195.375001,moment),32); #Moment evaluated at
midspan
```

moment_midspan := -48.864319632852071507616553

```
stress_end_uncracked:=evalf(moment_end*(2.6+.2)/(Iau),32); #Bending
stress at anchorage for uncracked case
```

stress_end_uncracked := 8.6417956832351681486981393481308

```
stress_end_no_grout:=evalf(moment_end*(2.6+.2)/(Iac),32); #Bending stress
at the acnhorage for no grout case
```

stress_end_no_grout := 19.710876385709730545686408499668

```
stress_mid_uncracked:=evalf(moment_midspan*(1.33+.2)/(Ifu),32); #Bending
stress at the midspan for uncracked case
```

stress_mid_uncracked := -20.883354479961918828674113432961

```
stress_mid_no_grout:=evalf(moment_midspan*(1.33+.2)/(Ifc),32); #Bending
stress at the midspan for no grout case
```

stress_mid_no_grout := -31.281342693834171299854948154812

```
plot(d,z=0..395.375);
```

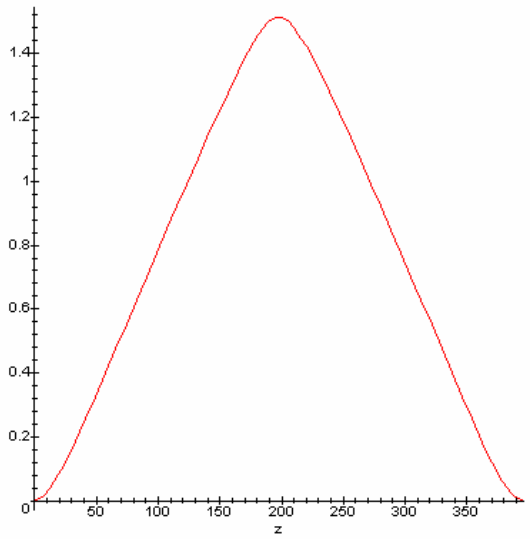


```
g:=L/2;
```

g := 197.6875000

```
d:=evalf(-((M^2)/(K^2))*(g-(L/2))*Heaviside(g-L/2)+((M^2)/(K^3))*Heavisid
e(g-(L/2))*sinh(K*(g-(L/2)))-(po*g^2/(2*K^2))+sols[1,1]+sols[2,1]*g+sols[
3,1]*sinh(K*g)+sols[4,1]*cosh(K*g),32);
```

d := 1.5153246286501250073967214O4

B.1.2 Cable modeling for un-grouted specimens

As mentioned in Chapter 4 the un-grouted specimens, #5 and #8 can be modeled analytically as cables. The approach for calculating the displacements and subsequent increases in tensile force are outlined in this section.

The geometry of the setup and loading conditions for the un-grouted specimens are seen in the following figure.

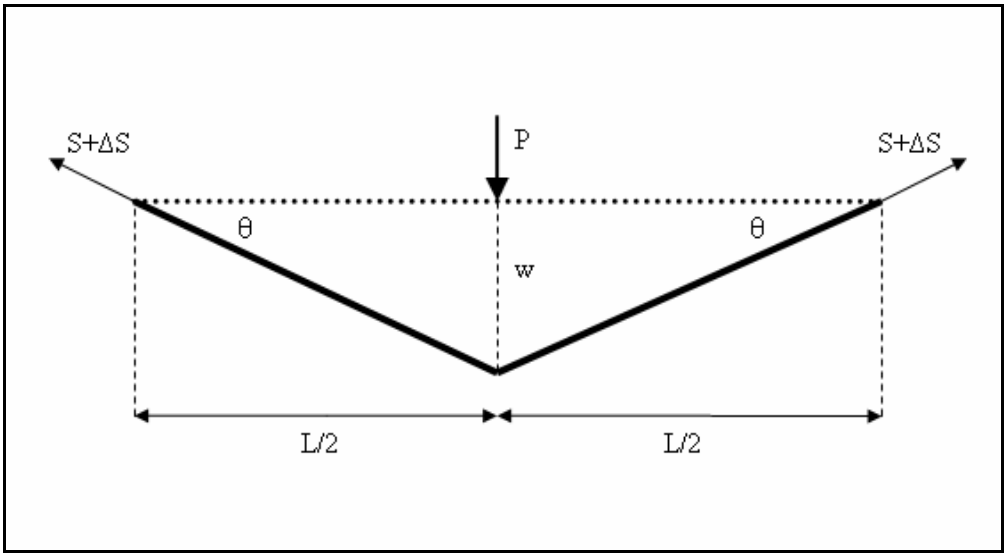

Figure B.1 Schematic of un-grouted test specimens

Where; S is the applied tension force, P denotes the applied load at midspan, w is vertical displacement, and ΔS is the increase in tension due to cable deformation.

Sum of vertical forces;

$$\sum Fy = 0$$
$$P = 2(S + \Delta S)\sin(\theta) \qquad \text{B.3}$$

The additional tension due to the elongation of the cable under the applied load, ΔS, can be written in terms of its strain.

$$\Delta S = \varepsilon \cdot E \cdot A \qquad \text{B.4}$$

Where the strain, ε, is determined by the change in length of the specimen;

$$\varepsilon = \frac{\Delta L}{L/2} \qquad \text{B.5}$$

The change in length, ΔL, of each half of the specimen can be found as;

$$\Delta L = \left(\frac{L}{2}\right) \cdot \left(\frac{1}{\cos(\theta)}\right) - \left(\frac{L}{2}\right) \qquad \text{B.6}$$

Therefore;

$$\varepsilon = \left(\frac{1}{\cos(\theta)} - 1\right) \qquad \text{B.7}$$

We can now substitute this expression for strain into our expression for additional tension.

$$\Delta S = \left(\frac{1}{\cos(\theta)} - 1\right) \cdot E \cdot A \qquad \text{B.8}$$

Going back to our equilibrium equation (B-10) we can now substitute this expression for additional tension to obtain:

$$P = 2\left[S + \left(\frac{1}{\cos(\theta)} - 1\right) \cdot E \cdot A\right] \cdot \sin(\theta) \qquad \text{B.9}$$

Which results in:

$$P = 2 \cdot S \cdot \sin(\theta) + 2 \cdot \left[\tan(\theta) - \sin(\theta)\right] \cdot E \cdot A \qquad \text{B.10}$$

Using Taylor expansions up to the second terms for sin(θ) and tan(θ) there results:

$$P = 2 \cdot S \cdot \left(\theta - \frac{\theta^3}{3!}\right) + 2 \cdot \left[\left(\theta + \frac{\theta^3}{3}\right) - \left(\theta - \frac{\theta^3}{3!}\right)\right] \cdot E \cdot A \qquad \text{B.11}$$

Simplifying the expression:

$$P = 2 \cdot S \cdot \theta + \left(E \cdot A - \frac{S}{3} \right) \cdot \theta^3 \qquad \text{B.12}$$

We can assume that small angle theory holds based on the lab experiments which showed that:

$$\tan(\theta) = \frac{w}{L/2} = \frac{1.6\ in}{197.6875\ in} = .81\% \qquad \text{B.13}$$

Therefore we can assume the following;

$$\tan(\theta) \cong \sin(\theta) \cong \theta \cong \frac{w}{L/2} \qquad \text{B.14}$$

The equilibrium equation then becomes;

$$P = 2 \cdot S \cdot \left(\frac{2w}{L} \right) + \left(EA - \frac{S}{3} \right) \cdot \left(\frac{2w}{L} \right)^3 \qquad \text{B.15}$$

The specifications from the lab; tension, Young's modulus, cross-sectional area, and length for un-grouted specimen numbers 5 & 8 were:

$$E = 27500\ \frac{kips}{in^2} \quad A = 4.123\ in^2 \quad L = 395.375\ in \quad S = 445\ kips$$

Notice the first term in the load displacement equation is:

$$1^{st}\ \text{term} = \left(\frac{4S}{L} \right) w \qquad \text{B.16}$$

Using the static testing loads of 6.5 kips and 6.6 kips for specimens #5 & #8 respectively, the displacements due to the first term in the equation are;

$$P_5 = 6.5\ kips \quad w_5 = \frac{P_5 L}{4S} \quad w_5 = 1.444\ in \qquad \text{B.17}$$

$$P_8 = 6.6\ kips \quad w_8 = \frac{P_5 L}{4S} \quad w_8 = 1.466\ in \qquad \text{B.18}$$

The higher order term in the load –displacement equation is:

$$P_{higher-term} = \left(8 \cdot \frac{EA - S}{3L^3}\right) \cdot w^3 \qquad \text{B.19}$$

Substituting the values of displacement obtained we find the additional loads due to these higher order terms as:

$$P_{5-higher-term} = .015\ kips$$
$$P_{8-higher-term} = .015\ kips$$

In comparison to the 6.5 and 6.6 kip loads applied this suggests that the higher order terms do not have much effect here.

The effects of self-weight should be taken into account as well. The 1st order displacements due to self-weight, 0.462 kips total for each specimen, are calculated as:

$$\delta_{self-weight} = \frac{wL}{8S} \qquad \delta_{self-weight} = .051\ in \qquad \text{B.20}$$

The total displacement is found with superposition of the point load and self-weight displacements and compared with the lab displacements here;

$$\Delta_5(total) = w_5 + \delta_{self-weight} \qquad \Delta_5(total) = 1.495\ in \qquad \text{B.28}$$

$$\Delta_6(total) = w_6 + \delta_{self-weight} \qquad \Delta_6(total) = 1.517\ in \qquad \text{B.29}$$

Bibliography

Abdel-Ghaffar, A.M., and M.A. Khalifa. “Importance of Cable Vibration in Dynamics of Cable-Stayed Bridges.” Journal of Engineering Mechanics 117 (1991): 2571-2589.

Burgess, J.J., and M.S. Triantafyllou. "The Elastic Response Frequencies of Cables." Journal of Sound and Vibration 120.1 (1998): 153-165.

Caracoglia, L., and N.P. Jones. "In-plane dynamic behavior of cable networks. Part 1: formulation and basic solutions." Journal of Sound and Vibration 279 (2005): 969-991.

Chang, W.K., V. Pilipchuk, and R.A. Ibrahim. "Fluid Flow-Induced Nonlinear Vibration of Suspended Cables." Nonlinear Dynamics 14 (1997): 377-406.

Dowd, J. Response of Stay Cables to High Amplitude Vibrations. Master’s Thesis, The University of Texas at Austin, 2001.

Eggers, J. Cable Stay Fatigue Analysis for the Fred Hartman Bridge. Master’s Thesis, The University of Texas at Austin, 2003.

Gimsing, Niels J. Cable Supported Bridges. 2nd ed. New York: John Wiley & Sons, 1998.

Gu, M., and X. Du. “Experimental Investigation of Rain-Wind-Induced Vibration of Cables in Cable-Stayed Bridges and its Mitigation.” Journal of Wind Engineering and Industrial Aerodynamics 93 (2005): 79-95.

Hartono, and A.H.P. Van Der Burgh. "A linear differential equation with a time-periodic damping coefficient: stability diagram and an application." Journal of Engineering Mechanics 49 (2004): 99-112.

Hikami, Y., “Rain Vibration of Cables in Cable-Stayed Bridges.” Journal of Wind Engineering 27 (1986): 23-34.

Hikami, Y., and N. Shiraishi. “Rain-Wind Induced Vibrations of Cable-Stayed Bridges.” Journal of Wind Engineering and Industrial Aerodynamics 29 (1988): 409-418.

Hobbs, R.E., and K. Ghavami, “The Fatigue of Structural Wire Strands.” International Journal of Fatigue 4 (1982): 69-72.

Irvine, H.M. Cable Structures. 1st ed. New York: Dover Publications, 1981.

Irvine, H.M. "Local Bending Stresses in Cables." International Journal of Offshore and Polar Engineering 3 (1993): 172-175.

Irvine, H.M., and T.K. Caughey, "The Linear Theory of Free Vibrations of a Suspended Cable." Proceedings of the Royal Society 341 (1974): 299-315.

Ito, M., Y. Fujino, T. Miyata, and N. Narita Cable-Stayed Bridges: Recent Developments and their Future. 1st ed. New York: Elsevier Science Publishers B.V., 1991.

Jones, N. P., T. Kumarasena, P. Irwin, and A. Felber "Wind-Induced Vibration of Stay-Cables" FHWA Study 2003.

Kervorkian, J., and Cole, J.D. Perturbation Methods in Applied Mathematics. 1st ed. New York: Springer-Verlag, 1981.

Leonhardt, F., and W. Zellner. "Past, Present and Future of Cable-Stayed Bridges." Proceedings of the Cable-Stayed Bridges Seminar. Yokohama, Japan. December 10-11 1991.

Lilien, J.L., and A. Pinto da Costa. "Vibration Amplitudes Caused by Parametric Excitation of Cable-Stayed Structures." Journal of Sound and Vibration 174 (1994): p.69-90.

Matsumoto, Masaru, Yoshiyuki Daito, Takashi Kanamura, and Yoshinori Shigemura. "Wind-induced vibration of cables of cable-stayed bridges." Journal of Wind Engineering and Industrial Aerodynamics 1998: 1015-1027.

Matsumoto, Masaru, Tomomi Yagi, Mitsutaka Goto, and Seiichiro Sakai. "Rain-wind-induced vibration of inclined cables at limited high reduced wind velocity region." Journal of Wind Engineering and Industrial Aerodynamics 2003: 1-12.

Papanikolas, P. Axial Fatigue of Multi-Layered Wire Strands. Doctoral Dissertation, The University of Alberta, 1995.

Pinto da Costa, A., J.A.C Martins, F. Branco, and J.L. Lilien. "Oscillations of Bridge Stay Cables Induced by Periodic Motions of Deck and/or Towers." Journal of Engineering Mechanics July 1996: 613-622.

Poser, M. Full-Scale Bending Fatigue Tests on Stay Cables. Master's Thesis, The University of Texas at Austin, 2001.

Post-Tensioning Institute. "Recommendations for Stay-Cable Design, Testing and Installation." PTI Guide Specification, 2000.

Raoof, M. "Design of Steel Cables Against Free-Bending Fatigue at Terminations." The Stuctural Engineer 71.10 (1993): 171-178.

Ridd, J. Fatigue Performance of Stay Cables. Master's Thesis, The University of Texas at Austin, 2004.

Triantafyllou, M.S., and L. Grinfogel. "Natural Frequencies of Inclined Cables ." Journal of Structural Engineering 112.1 (1986): 139-148.

Troitsky, M.S. Cable-Stayed Bridges. 1st ed. London: William Clowes & Sons, Limited, 1977.

Verwiebe, C., and H. Ruscheweyh. "Recent research results concerning the exciting mechanisms of rain-wind-induced vibrations." Journal of Wind Engineering and Industrial Aerodynamics 1998: 1005-1013

Virlogeux, M. “Cable Vibrations in Cable-Stayed Bridges.” Bridge Aerodynamics. Ed Larsen and Esdahl. 1998: 213-233.

Walther, R., B. Houriet, W. Isler, P. Moia, and J.F. Klein. Cable Stayed Bridges. 2nd ed. London: Thomas Telford, 1999.

Willox, A. Determining the Vibration-Induced Stresses in the Stay-Cables of the Fred Hartman Bridge. Master’s Departmental Report, The University of Texas at Austin, 2000.

Whitlock Dalrymple Poston & Assoc., Evaluation and Repair of Stay-Cable Vibrations, Fred Hartman Bridge and Veterans Memorial Bridge. Progress Report, WDP Project No. 06-95114B, 1998.

Wyatt, T.A. "Secondary Stresses in Parallel Wire Cables." Journal of the Structural Division, Proceedings of the American Society of Civil Engineers 86.ST7 (1960): 37-59.

VITA

Aaron James Pebley was born to James Walter and Cynthia Marie Pebley March 4, 1979 in Brunswick, Maine. Raised in San Diego, California Aaron attended Ramona High School and graduated in 1997. After high school he attended the University of California, San Diego where he received a bachelor's degree in Structural Engineering conferred upon him June 2002. Upon graduation Aaron worked as a civil design engineer with Martin & Ziemniak Civil Engineers where he worked until his enrollment into the graduate Civil Engineering Program at the University of Texas, Austin in September of 2003. Working as a graduate research assistant while completing the required curriculum he finished his Master's work in the summer of 2005. After graduation Aaron will be starting work as a structural designer with the structural consulting firm KPFF in Los Angeles, California, living the good life.

Permanent Address:

1183 Saxony Rd.

Encinitas, CA 92024

This thesis was typed by the author.